LUND UNIVERSITY

Laminar burning velocity of hydrogen and flame structure of related fuels for detailed kinetic model validation

Alekseev, Vladimir

2015

Laminar burning velocity of hydrogen and flame structure of related fuels for detailed kinetic model validation

Doctoral Thesis

Vladimir Alekseev

Division of Combustion Physics
Department of Physics

Lund 2015

LUND
UNIVERSITY

Printed by: Tryckeriet E-huset, Lund, Sweden
November 2015

Lund Reports on Combustion Physics, LRCP-190
ISBN 978-91-7623-518-8 (printed)
ISBN 978-91-7623-519-5 (pdf)
ISSN 1102-8718
ISRN LUTFD2/TFCP-190-SE

Vladimir Alekseev
Division of Combustion Physics
Department of Physics
Lund University
P.O. Box 118, SE-221 00
Lund, Sweden

Abstract

The laminar burning velocity and the flame structure are common targets for combustion studies aimed at detailed kinetic model development. In the present work, fuels relevant to hydrogen combustion were considered.

The laminar burning velocity of rich and lean hydrogen flames was studied experimentally and numerically, including its pressure dependence in rich mixtures and temperature dependence in lean mixtures. An updated version of the Konnov detailed reaction mechanism for H_2 combustion was validated, and after that it was applied to simulate the results obtained in experiments. The laminar burning velocities of rich H_2 + air mixtures were determined from spherical flame propagation data using three models for stretch correction available in the literature. The heat flux method was employed for the first time to measure the laminar burning velocity of lean H_2 + air mixtures and its temperature dependence. A modified procedure for processing data from unstable cellular flames was suggested, and its accuracy was evaluated. The observed difference between the literature results obtained in stretched flames and the values measured in the present work in flat flames was discussed. The trends in the temperature dependence of the burning velocity of lean H_2 + air mixtures, indicated by the modeling but not supported by the majority of data determined from literature values, were confirmed experimentally in the present work.

An analysis of the experimental uncertainties of the heat flux method was performed. It was shown that some of the factors which affect the accuracy of the measurements are related to the temperature dependence of the laminar burning velocity. A method to evaluate asymmetric heat fluxes in the plate of the heat flux burner was proposed. The work reported in the present study resulted in the necessity to re-evaluate some of the previously published data. Based on the available information from literature, as well as on the results obtained in the present study, recommendations were made on how to control or reduce several experimental uncertainties associated with the heat flux method.

The structure of NH_3 and CH_4 flames was investigated with the aim of further kinetic model development. Intracavity laser absorption spectroscopy was applied to record HCO concentration profiles in rich low-pressure CH_4 mixtures and predictions of two widely used kinetic models were analyzed. Minor

and major species concentrations in NH_3 + air flames were used to validate four contemporary H/N/O reaction schemes and investigate the performance of the best one.

Popular summary

The word "combustion" describes a number of physical and chemical processes, whose common characteristic is an interaction between fuel and oxygen and their subsequent transformation into products, such as CO_2 and water. Even though the process is often described as a single chemical reaction between fuel and oxygen, in reality, their chemical transformation requires many intermediate stages and involves many reactions. The simplest combustion system is hydrogen + oxygen (H_2 + O_2), which can be described with 8 species and about 20 elementary reactions. The smallest hydrocarbon fuel, methane, requires at least 35 species and 170 reactions. If all the species and reactions are defined, the combustion process can be formulated in a mathematical model. Such simulations have become widely used since they can provide a deeper understanding of the underlying processes, which might not be accessible in experiments. However, even the simplest system of hydrogen + oxygen is still not completely characterized under all conditions. Further development of our understanding becomes even more important since at the moment hydrogen combustion is receiving increased attention in industry due to reduced pollutant formation if hydrogen is used as a fuel.

One of the most important parameters of a combustible mixture is the laminar burning velocity, which describes how fast the flame can propagate in space. It is important from both practical and fundamental points of view. Knowledge of the laminar burning velocity is required in the design and development of combustion devices, such as internal combustion engines or gas turbines. In addition, the laminar burning velocity is a parameter that is used to develop combustion models and/or judge their performance. Flame structure, i.e. the distribution of species inside the flame, can also serve this objective.

Due to a constant improvement in combustion models, there is an increasing need to provide accurate experimental values of the laminar burning velocities. It is defined theoretically as the speed of an infinitely large freely propagating planar flame. Such conditions can not be reproduced in the laboratory, therefore, the accuracy of the measurements is determined not only by the quality of experimental equipment, it also depends on whether the laboratory system is close enough to these ideal theoretical conditions. A part of the work reported in this thesis concerns the accuracy of the heat flux

method, which is one of the three widely used methods for burning velocity measurement. As a result of the present work, some of the practical issues that can lead to inaccurate values of the burning velocity were identified and recommendations were made with the aim of improving the accuracy of the method.

A major part of this thesis concerns the laminar burning velocity of hydrogen flames and how it changes with increasing temperature of the initial combustible mixture. This was analyzed both experimentally and using combustion models. In some cases, hydrogen flames can lose stability, i.e. they start to form irregular structures, or cells. When this occurs, the experimental procedure for determination of the burning velocity has to be modified. The approach applied in this thesis made it possible to perform measurements in such unstable flames without losing the accuracy. As for the temperature dependence of the burning velocity, it has a complex behavior, which is often disregarded in engineering applications. In the present work, this behavior was discussed and analyzed.

The last part of the thesis is related to the flame structure of fuels relevant to hydrogen energy, ammonia (NH_3) and methane (CH_4). Such fuels are often referred to as hydrogen carriers, i.e. they can be stored, transported and later converted to H_2. This procedure can be advantageous due to the explosive nature of hydrogen. In this thesis, CH_4 systems were studied under conditions relevant to hydrogen production, for which the combustion models are still underdeveloped. On the other hand, ammonia is a simple fuel which does not contain carbon, so the aim of the ammonia project was therefore to study fundamental nitrogen chemistry. Several existing combustion models were applied to simulate the structure of ammonia and methane flames, with the aim to find out how these models can be developed in the future.

List of papers

Paper I: V.V. Zamashchikov, V.A. Alekseev, A.A. Konnov, Laminar burning velocities of rich near-limiting flames of hydrogen, Int. J. Hydrogen Energy 39 (2014) 1874–1881; http://dx.doi.org/10.1016/j.ijhydene.2013.11.054.

Paper II: V.A. Alekseev, M. Christensen, A.A. Konnov, The effect of temperature on the adiabatic burning velocities of diluted hydrogen flames: A kinetic study using an updated mechanism, Combust. Flame 162 (2015) 1884-1898; http://dx.doi.org/10.1016/j.combustflame.2014.12.009.

Paper III: V.A. Alekseev, M. Christensen, E. Berrocal, E.J.K. Nilsson, A.A. Konnov, Laminar premixed flat non-stretched lean flames of hydrogen in air, Combust. Flame 162 (2015) 4063-4074;
http://dx.doi.org/10.1016/j.combustflame.2015.07.045.

Paper IV: C. Brackmann, V.A. Alekseev, B. Zhou, E. Nordström, P.-E. Bengtsson, Z. Li, M. Aldén, A.A. Konnov, Structure of premixed ammonia + air flames at atmospheric pressure: laser diagnostics and kinetic modeling, Combust. Flame (2015);
http://dx.doi.org/10.1016/j.combustflame.2015.10.012.

Paper V: V.A. Alekseev, M. Christensen, J.D. Naucler, E.J.K. Nilsson, E.N. Volkov, L.P.H. de Goey, A.A. Konnov, Experimental uncertainties of the heat flux method for measuring burning velocities, *submitted to Combustion Science and Technology.*

Paper VI: A. Fomin, T. Zavlev, I. Rahinov, V.A. Alekseev, A.A. Konnov, S. Cheskis, Intracavity laser absorption spectroscopy study of HCO radicals during methane to hydrogen conversion in very rich flames, Energy Fuels 29 (2015) 6146-6154; http://dx.doi.org/10.1021/acs.energyfuels.5b01497.

Paper VII: A. Fomin, T. Zavlev, I. Rahinov, V.A. Alekseev, A.A. Konnov, V.M. Baev, S. Cheskis, Fiber Laser Intracavity Spectroscopy of hot water for temperature and concentration measurements, Appl. Phys. B: Lasers Opt. (2015); http://dx.doi.org/10.1007/s00340-015-6236-4.

Related work

L. Sileghem, V.A. Alekseev, J. Vancoillie, K.M. Van Geem, E.J.K. Nilsson, S. Verhelst, A.A. Konnov, Laminar burning velocity of gasoline and the gasoline surrogate components iso-octane, n-heptane and toluene, Fuel 112 (2013) 355-365; http://dx.doi.org/10.1016/j.fuel.2013.05.049.

L. Sileghem, V.A. Alekseev, J. Vancoillie, E.J.K. Nilsson, S. Verhelst, A.A. Konnov, Laminar burning velocities of primary reference fuels and simple alcohols. Fuel 115 (2014) 32-40; http://dx.doi.org/10.1016/j.fuel.2013.07.004.

Contents

Chapter 1

Introduction

Detailed kinetic modeling is one of the most widespread instruments in combustion studies. Development of detailed kinetic mechanisms is important both from fundamental and practical points of view. Kinetic modeling of combustion can provide a deeper understanding of the underlying processes, which might not be accessible for experiments. On the practical side, correct and comprehensive description of the combustion process will lead to accurate prediction of pollutant formation, which is often a main goal for model development. Detailed reaction mechanisms also serve as a basis for reduced mechanisms, necessary for CFD simulations of practical combustion devices, e.g., engines or gas turbines.

A detailed mechanism consists of a number of elementary reactions, whose rate constants are commonly determined via so-called *direct* measurements, where the effect of a specific reaction is isolated in a dedicated experiment, e.g., in a shock tube or a flow reactor. In addition, elementary reaction rates are often determined using quantum chemistry calculations. However, another method to study individual reaction rates as well as the overall performance of the mechanism is to conduct *indirect* experiments, where a certain integral physical parameter is measured in a laboratory environment that correspond to the idealized 0D or 1D configurations. Laminar burning velocity, S_L, is a main indirect target for kinetic model validation. Accurate values of S_L are equally important for practical applications, e.g., they often serve as an input parameter for the CFD models.

Conditions in the practical combustion systems are usually different from those that can be reproduced in the laboratory experiments, namely, the "real" combustion occurs at elevated temperatures and pressures. For that reason, not only a single value of S_L must be determined in the experiments, but also its temperature and pressure dependence should be studied, which in turn would allow extrapolation of the measured values to the desired conditions. Such dependences can typically be characterized by a number of scalar quantities in a certain functional dependence. Both temperature and pressure

dependence of S_L of a specific mixture is represented via an empirical power law equation, which can be respectively written as:

$$S_L = S_L^0 \cdot \left(\frac{T_g}{T_g^0} \right)^{\alpha} \tag{1.1}$$

$$S_L = S_L^0 \cdot \left(\frac{p}{p_0} \right)^{\beta} \tag{1.2}$$

where S_L is the burning velocity at a specific unburned gas temperature T_g or pressure p, and S_L^0 is the burning velocity at a reference temperature T_g^0 or pressure p_0. The power exponents α and β are often referred to as temperature or pressure dependence themselves, since they are single scalar quantities characterizing S_L at all temperatures or pressures. The power exponents α or β can be derived from S_L values obtained in the laboratory experiments, and then used for extrapolation of S_L to the conditions of practical combustors. They can also serve as indicators of the consistency of the experimental burning velocity data. In addition, power exponent β is an independent target quantity (together with S_L) that can be used in model development.

There are four commonly used methods that allow determination of S_L: the conical flame method, the spherical flame method, the counterflow flame method and the heat flux method. All methods are built on different principles and, therefore, their accuracy is determined by different parameters. An analysis of the uncertainty factors, specific for each method, should be performed to define the accuracy of S_L. The experimental uncertainty range has to be considered when making comparison between the values obtained in the measurements and by detailed kinetic modeling, and consequently, when the predictive ability of the mechanism is evaluated.

Laminar burning velocity is not the only parameter, valuable for kinetic model development, that can be determined in flame experiments. Flame structure, i.e., spatial profiles of species concentrations and temperature, is another indirect target for model validation. With the modern non-intrusive laser diagnostics methods, the concentration of important flame intermediates can be accurately determined at conditions that can be directly reproduced with 1D detailed kinetic modeling.

The development of comprehensive combustion models is often hierarchical, i.e., different sub-parts of the mechanism are created one after another. One of the most important parts is the H/O sub-mechanism which involves reactions between species that consist only of H and O atoms. The H/O sub-mechanism is small, but it contains a number of elementary reactions that affect the predictive ability of the mechanism at all conditions. This sub-mechanism can be fully revealed if it is studied in an isolated system, such as combustion of hydrogen (H_2). Hydrogen is important not only from a fundamental point of view, but also as a practical fuel, since it is a component of syngas (H_2 + CO). The H/O sub-mechanism can be further extended to a larger H/N/O system, which also has a practical importance. The H/N/O sub-system covers some

of the major pathways for NO production. Ammonia (NH_3) can serve as a laboratory fuel that allows isolation of the H/N/O sub-mechanism.

Ammonia, as well as CH_4, are often referred to as hydrogen carriers, i.e. they can be stored, transported and later converted to H_2 or syngas. This procedure can be advantageous due to explosive nature of hydrogen. Syngas fuels can be produced by partial oxidation of rich CH_4 mixtures, however, the detailed reaction mechanisms for CH_4 at these conditions still require further development.

The overall goal of this thesis was to study, experimentally and numerically, combustion of fuels related to hydrogen. The thesis is build on the contents of several papers. Paper I is related to the laminar burning velocity of rich hydrogen + air mixtures determined from spherical flame propagation data, and in Paper III S_L of lean H_2 + air mixtures is studied with the heat flux method. The temperature dependence of S_L is discussed in Papers II and III. In Paper V, the experimental uncertainties related to the use of the heat flux method for measuring laminar burning velocities, are analyzed.

Papers IV, VI and VII are related to flame properties other than laminar burning velocity, their experimental determination and reproducibility in the kinetic simulations. Paper IV discusses flame structure of NH_3 flames and how adequately it can be simulated with the contemporary kinetic mechanisms. Paper VI is dedicated to HCO, an important intermediate in hydrocarbon combustion, which is studied with Intracavity Laser Absorption Spectroscopy (ICLAS) under conditions relevant to syngas production. Finally, in Paper VII, the use of H_2O absorption in the infrared for determination of the flame temperature is discussed.

Chapter 2

Experimental and modeling methods

2.1 Laminar burning velocity

2.1.1 Definitions and experimental methods

Laminar burning velocity is the speed of a free-propagating planar adiabatic flame relative to the unburned mixture. While direct implementation of the S_L definition for its measurement is not possible, since it requires to create an infinite and perfectly planar flame, three main geometries are utilized for S_L measurement: burner-stabilized planar flames, spherical flames and counterflow/stagnation flames. Figure 2.1 presents a schematic view of the three geometries and defines the main flame parameters. As mentioned in the Introduction, there are also conical (Bunsen) flames, however, as concluded in, e.g., [1], the Bunsen flame method can only be used for rough estimation of S_L, therefore, it is not considered in the following. In the planar configuration, the flame can be seen stationary in the laboratory coordinate system. The unburned mixture is characterized by its velocity S_u and density ρ_u, and the product zone by S_b and ρ_b, respectively. The conservation of mass readily yields:

$$S_u \cdot \rho_u = S_b \cdot \rho_b \tag{2.1}$$

In the coordinate system relative to the fresh gas, the flame velocity is the laminar burning velocity S_L, equal to S_u. Planar flame geometry is utilized in the heat flux method, where flat adiabatic flames are stabilized on a specially designed burner. S_L in these experiments is readily obtained since S_u can be easily determined.

In the spherical flame configuration, the products have zero velocity in the laboratory coordinate system, however, Eq. (2.1) holds in a system relative to the flame, assuming it to be infinitely thin. Thus, the visible flame front

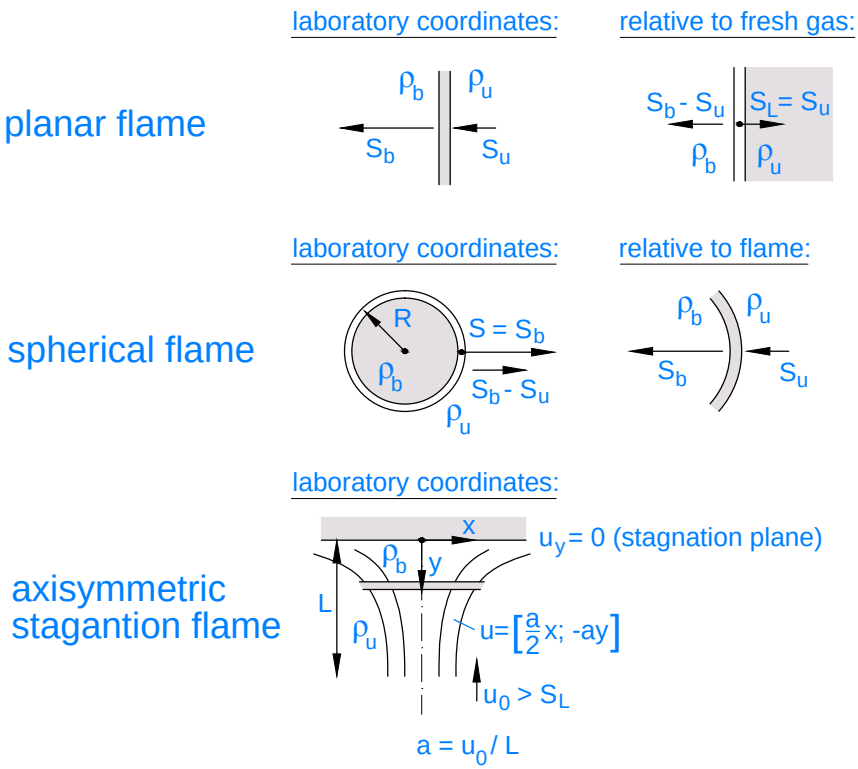

Figure 2.1: *Main flame geometries for S_L measurement: planar flames (top), spherical flames (middle) and counterflow/stagnation flames (bottom). The subscripts "u" and "b" correspond to the unburned mixture and products, respectively. Shaded areas have zero velocity in the chosen coordinate system.*

speed S is equal to S_b. As opposed to the planar case, S_u is not equal to S_L, since the flame is not planar, and its properties are affected by flame stretch, existing due to its curvature. S is a function of the flame front radius R. The dependence $S(R)$ can be recorded with an optical system, and then S_b is extrapolated to the stretch-free velocity S_b^0. Then it is recalculated to $S_u^0 = S_L$ with Eq. (2.1).

In stagnation flames, the flame is stabilized in decelerating and diverging flow issued from the nozzle with initial cold flow velocity u_0. In order to stabilize the flame, this velocity must be higher than the laminar burning velocity. The flow is diverged by the presence of stagnation surface, or symmetry plane in the case of twin opposed jets, and this configuration is called counterflow. The flame, as in the spherical configuration, is stretched, but due to aerodynamic strain. Applying one of the velocimetry techniques, the unburned gas velocity close to the flame front can be measured, and by varying u_0, its dependence on the stretch rate can be determined. Then S_L is obtained by

extrapolation to zero stretch.

The three methods for laminar burning velocity determination: spherical bomb method, counterflow method and the heat flux method utilize the flame geometries of Figure 2.1. They are built on different principles, therefore, each of them has its own advantages and range of applicability. The main advantage of the spherical bomb method is its higher pressure range. The maximum working pressures for determination of S_L were specified to be about 50 atm [2], however, measurements at 60 atm were demonstrated [3]. In comparison, for the counterflow method, burning velocities of CH_4 flames at 4.5 atm were reported [4]. Figura and Gomez [5] instead studied *counterflow diffusion flames* at pressures up to 30 atm and concluded that above 10 atm, the inert component in the mixture should be substituted to He, in order to suppress flame instabilities due to increasing Reynolds number. The same approach was used by Goswami et al. [6] to obtain S_L of syngas fuels up to 10 atm with the heat flux method, while in N_2-diluted mixtures, S_L at 1-4 atm was reported for syngas [7] and at 1-5 atm for CH_4 [8]. The heat flux method also has a limitation in velocities, so that S_L up to about 40-60 cm/s can be measured, and above that, the flame area would become disturbed by the presence of the perforated burner plate.

The main advantage of the heat flux method is that the flames are flat, thus a direct determination of the laminar burning velocity is possible, without correction for stretch or curvature at the data processing stage. The propagation velocity of a stretched flame must be extrapolated to zero stretch employing one of the existing theoretical or empirical models, thus the procedure for stretch correction becomes a source of uncertainty in the determined value of the laminar burning velocity.

The uncertainties in the experimental procedure or data processing can lead to discrepancies in the values of the burning velocities determined for the same mixture with different methods, or even with the same method but interpreting the measured results differently, e.g., using different stretch correction models. Figure 2.2 (taken from Paper III) shows an example of the existing scattering in experimental S_L values for lean H_2 + air mixtures. All results [10–28] were obtained in spherical or counterflow flames, and the color codes denote the measurement method and stretch-correction model implemented: green – spherical flame, linear model [29]; blue – spherical flame, non-linear model of Kelley and Law [30]; red – counterflow burner, linear model (LM) originated from [31]; orange – counterflow burner, non-linear extrapolation (NLM) based on the study of Tien and Matalon [32] for the data of Das et al. [27], and on the work of Wang et al. [33] for the data of Park et al. [28]. Stretch correction model is probably the most important issue affecting the burning velocity derived from the counterflow or spherical flames. Direct comparison of the measurements performed in the counterflow configuration by Das et al. and processed using linear [26] or non-linear model [27] shows that the non-linear extrapolation yields S_L about 32% lower when equivalence ratio, ϕ, equals 0.3. Park et al. [28] demonstrated that non-linear extrapolation lowers the S_L values significantly in lean flames with $\phi = 0.32$ and 0.45 as compared to the

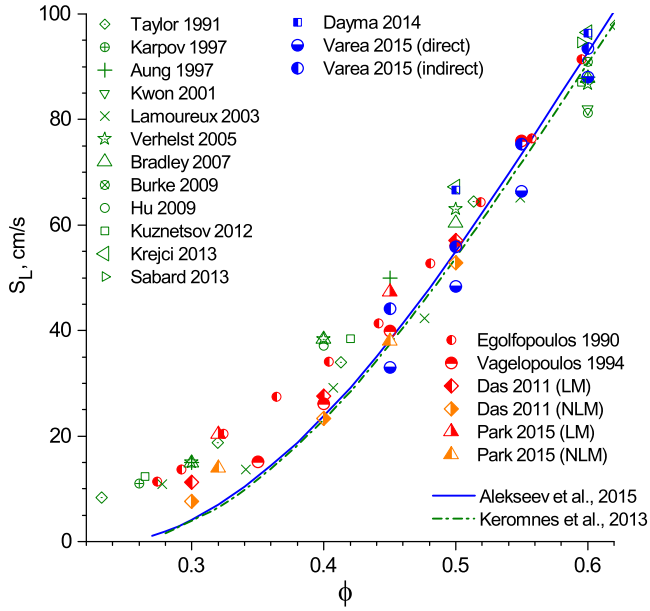

Figure 2.2: *Laminar burning velocity of lean H_2 + air flames at standard conditions(298 K, 1 atm). Symbols: experiments, lines: calculations using the models developed in Paper II and by Keromnes et al. [9]. The source of experimental data: green - Taylor [10], Karpov et al. [11], Aung et al. [12], Kwon and Faeth [13], Lamoureux et al. [14], Verhelst et al. [15], Bradley et al. [16], Burke et al. [17], Hu et al. [18], Kuznetsov et al. [19], Krejci et al. [20], Sabard et al. [21]; blue - Dayma et al. [22], Varea et al. [23]; red - Egolfopoulos and Law [24], Vagelopoulos et al. [25], Das et al. [26], Park et al. [28]; orange – Das et al. [27], Park et al. [28].*

linear model. For the spherical flames, Wu et al. [34] showed that all existing methods for stretch correction overestimate the laminar burning velocity at the conditions of Figure 2.2, and for the classical linear model [29] the difference can reach up to 60%. The experimental approach can also affect S_L. Varea et al. [23] used the technique for direct measurement of the local instantaneous unburned gas velocity [35, 36] (denoted "direct" in Figure 2.2) and compared the results to the S_L determined with a common approach by assuming jump conditions across the flame and validity of Eq. (2.1) (the dataset is denoted "indirect" in Figure 2.2). It was clearly demonstrated that these two methods lead to different values of S_L, with increasing discrepancy for lower ϕ, even though the numerical simulations predict similar values for both formulations.

As a consequence of the limitations of the S_L measurement methods, a discrepancy between experimental data and kinetic modeling is observed for the temperature dependence of H_2 flames. Figure 2.3 (from Paper II) presents the power exponents α from Eq. (1.1) for H_2 + air mixtures at standard conditions. The available experiments [15, 37–40] suggest α independent on ϕ, contradicting to several modeling studies [41–45], which indicate the rise of α

when the equivalence ratio becomes close to the flammability limits. While in some of the kinetic studies [18, 45, 46], α were obtained for standard conditions, the results from [41–44, 47] served as correlation parameters in wider ranges of temperatures and pressures (relevant for engines). The comparison of Figure 2.3 indicates that, in addition to ϕ, α depends on the correlation interval, e.g., the values of [18] and [43] differ, though obtained with the same kinetic scheme [48].

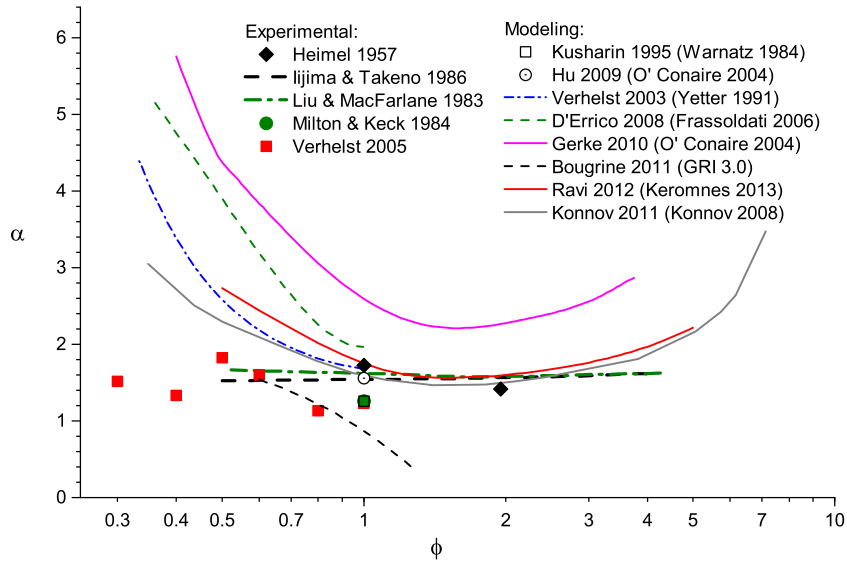

Figure 2.3: *Power exponent α for hydrogen + air flames at conditions close to 298 K and atmospheric pressure. Solid symbols and thick lines: experiments of Heimel [37], Iijima and Takeno [38], Liu and MacFarlane [39], Milton and Keck [40], Verhelst et al. [15]; open symbols and thin lines: modeling and correlations (with the kinetic mechanism in parenthesis) of Kusharin et al. [46] (Warnatz [49]), Hu et al. [18] (O'Conaire et al. [48]), Verhelst and Sierens [41] (Yetter et al. [50]), D'Errico et al. [42] (Frassoldati et al. [51]), Gerke et al. [43] (O'Conaire et al. [48]), Bougrine et al. [47] (GRI 3.0 [52]), Ravi and Petersen [44] (Keromnes et al. [9]), Konnov [45] (Konnov [53]).*

2.1.2 Determination of S_L from spherical flames

In the spherical flame configuration, the visible flame front speed S can be measured, however, its recalculation to the unburned mixture by Eq. (2.1) would not yield S_L, as in the case of planar 1D flames. The flame is curved, and thus affected by stretch, which can be defined as:

$$K = \frac{1}{A} \cdot \frac{dA}{dt} \tag{2.2}$$

Here A is an infinitesimal element of the flame surface, e.g., of an isotherm. The stretch rate K can be calculated as [54]:

$$K = \nabla_t \cdot \vec{u}_t + (\vec{V} \cdot \vec{n})(\nabla \cdot \vec{n}) \tag{2.3}$$

where $\vec{n}$ is a unit vector normal to the surface element A, $\vec{V}$ is the velocity of the *surface*, $\vec{u}_t$ and ∇_t are tangential components of the *flow* velocity $\vec{u}$ and ∇, respectively. For an infinitely thin spherical flame Eq. (2.3) yields:

$$K = \frac{2}{R} \cdot \frac{dR}{dt} \tag{2.4}$$

where R is the instantaneous flame front radius (see Figure 2.1). Laminar burning velocity S_L, visible flame speed S and stretch rate K (or flame radius R) can be related to each other using one or several scalar quantities via one of the extrapolation models. Wu et al. [34] summarized all models used by different authors, and they are listed in Table 2.1. Here, the unstretched burning velocity relative to products S_b^0 is related to S_L via Eq. (2.1), L_b is the Markstein length and C is a fitting parameter. Model 1 defines a linear relation between S_b and K and is therefore called the Linear Model (LM), while other four are non-linear (NLM) relative to stretch.

In the present work, three models: LM, NLM1 and NLM2 were considered in relation to the propagation of rich near-limiting H_2 + air flames. The base equation for the linear model, Eq. (2.5), can be applied directly to obtain S_b^0 using the experimentally recorded flame propagation ($R(t)$) and Eq. (2.4), knowing that $S_b = dR/dt$. It can also be integrated, so the fitting curve would be $R(t)$ itself [57]. For LM, integration of Eq. (2.5) gives:

$$R - R_0 + 2L_b \cdot \ln\left(\frac{R}{R_0}\right) = S_b^0 \cdot (t - t_0) \tag{2.10}$$

where R_0 and t_0 are the flame radius and time at the starting point of the integration. Equation (2.10) allows obtaining of S_b^0, L_b and R_0 by the least-square method from the experimentally recorded $R(t)$ starting at t_0. For NLM1, a similar expression can be obtained:

$$R - R_0 + 2L_b \cdot \ln\left(\frac{R - 2L_b}{R_0 - 2L_b}\right) = S_b^0 \cdot (t - t_0) \tag{2.11}$$

Table 2.1: *Extrapolation models for spherical flames*

No.	Abbr.	Ref.	Equation	
1	LM	[29]	$S_b = S_b^0 - L_b \cdot K$	(2.5)
2	NLM1	[55]	$\frac{S_b}{S_b^0} = 1 - \frac{2L_b}{R}$	(2.6)
3	NLM2	[30]	$\frac{S_b}{S_b^0}\, ln\left(\frac{S_b}{S_b^0}\right) = -\frac{2L_b}{R}$	(2.7)
4	NLM3	[56]	$\frac{S_b}{S_b^0} \cdot \left[1 + \frac{2L_b}{R} + \frac{4L_b^2}{R^2} + \frac{16L_b^3}{3R^3} + o^4\left(\frac{L_b}{R}\right)\right] = 1$	(2.8)
5	NLM4	[34]	$\frac{S_b}{S_b^0} = 1 - \frac{2L_b}{R} + \frac{C}{R^2}$	(2.9)

and the same fitting procedure can be applied. Integration of Eq. (2.7) for NLM2 was performed by Kelley and Law [30]. Their solution can be rewritten to resemble Eq. (2.11):

$$t - t_0 = \frac{2L_b}{S_b^0}\left(-\int_{z_0}^{z}\frac{e^{-z}dz}{z} - \frac{1}{\xi^2 ln\xi} + \frac{1}{\xi_0^2 ln\xi_0}\right) \tag{2.12}$$

where ξ is the implicit radius, so that: $R = -\frac{2L_b}{\xi \ln \xi}$, $R_0 = -\frac{2L_b}{\xi_0 \ln \xi_0}$, $z = 2\ln\xi$ and $z_0 = 2\ln\xi_0$. Hence, the three parameters S_b^0, L_b and ξ_0 are obtained from the least-square fit, and then R_0 is calculated via known L_b and ξ_0. Since the fitting of the experimental curve $R(t)$ with NLM2 is more difficult than NLM1, the parameters from NLM1 can be used as the initial guess. It can also be seen from the notation of $R(\xi)$, that for $L_b > 0$ flame radius must be $R > 2e \cdot L_b$. Therefore, when the initial parameters of NLM1 violate this condition, the fitting of NLM2 was not performed. In the present work, the fitting method of NLM2 allowed solutions at radii R_0 close to and above critical, whose definition will be given in Section 3.2.1. To determine the density ratio, necessary to convert S_b^0 into S_L (Eq. (2.1)), equilibrium calculations can be used assuming the jump conditions in the flame front.

2.1.3 Heat flux method

The following section is based on the contents of Papers III and V. The main objective of the work reported here was to analyze the accuracy of the method and determine the influencing factors. One of the main findings of the work is the modified method for data processing, which improved the accuracy of S_L measurements in unstable flames. A method to test the asymmetry of the heat fluxes in the burner plate was proposed. The asymmetric heat fluxes were found to be one of the reasons for discrepancies in the published burning velocity data, which were obtained on different heat flux burners in Lund.

2.1.3.1 Experimental setup and principle of the method

The S_L measurements in the present work were performed on a heat flux setup built in Lund. All parts of the experimental setup controlling flows, temperature and data acquisition, are assembled from commercial equipment, except for the burners, which were produced in mechanical workshops. The setup is shown in Figure 2.4 taken from Paper V. Essential parts of this heat flux installation are similar to those used in the earlier studies [58–60], but the data processing procedure has been updated and improved, as will be elucidated in Section 2.1.3.3. The scheme in Figure 2.4 is divided into four sections according to their main function: liquid and gas preparation (A), flow control and mixing (B), transfer and temperature control of the mixture (C) and burning velocity measurement (D). Two different mixing panels are available in Lund; Panel 2 has the same principal structure as Panel 1 shown in

Figure 2.4, but with just two gas channels and with the evaporator of a smaller capacity. The mass flow controllers (MFCs) and other parts of the setups (burners, water baths) are interchangeable. In the following description, if a particular element of Panel 2 is different from Panel 1, its specification will be given in parenthesis.

A liquid fuel or diluent (H_2O) is pressurized by an inert gas (N_2 or Ar) in a 5 L (2 L) fuel tank. The gases are fed from the central supply system or gas bottles in the laboratory to the mixing panel. The flow rates of the gas components are set by thermal MFCs from Bronkhorst High-Tech B.V., EL-FLOW F-201CV and F-201AV, and the liquid flow is controlled by a Coriolis "mini Cori-Flow" MFC, Bronkhorst High-Tech B.V., model M13. The MFCs are operated from a computer through a LabVIEW interface. Buffering vessels are installed upstream of the gas MFCs, damping possible fluctuations in the inlet flows. These vessels have a volume of 3 L following recommendations of the manufacturer of the MFCs [61]:

$$V \geq 2.02 \cdot 10^{-3} \frac{\Phi \cdot T_{MFC}^{0.5}}{p_1} \tag{2.13}$$

where the vessel volume V is expressed in L, Φ is the flow rate, L_n/min (normal liters per minute, equal to the volumetric flow at $T_0 = 0$ °C and $p_0 = 1$ atm), p_1 is the upstream pressure, bara, and T_{MFC} is the gas temperature, K, when it passes the MFC. Equation (2.13) is valid for conditions when the pressure drop at the MFC is more than 50% of p_1, and for a typical experiment the resulting volume V would be about an order of magnitude lower than the actually used volume (3 L).

All lines have particulate filters (Swagelok, FW Series) upstream of the MFCs, and plug valves (Swagelok) are installed upstream and downstream for safety reasons, i.e., in order to shut the line manually if the flows are uncontrolled. In addition, the valves are used to keep the lines shut when they are not in operation during measurements. For the gas MFCs, it is recommended to have the flow in a 10-90% range of the MFC maximum capacity. These constraints determine the required maximum capacities of MFCs for each mixture component. In Lund setups, MFCs with maximum flows from 4 to 30 L_n/min are used.

Liquid fuel or diluent is evaporated in the C.E.M. (Controlled Evaporator and Mixer) from Bronkhorst High-Tech B.V., model W-303A (W-202A). The capacity of the evaporator determines the maximal set flow of the Cori-Flow, 1200 g/h (200 g/h). The carrier gas, necessary for the operation of the C.E.M., can be selected by switching the 3-way valves (Swagelok) on two of the gas lines, and otherwise the C.E.M. can be by-passed if it is not in use.

The mixture is fed into the plenum chamber of the burner through a 4 m teflon tube, allowing time for complete mixing. If the measurements involve liquid fuels or diluents, the teflon tube is replaced by a 2 m (1 m) heating tube (KLETTI GmbH) to prevent fuel condensation. The required unburned gas temperature, T_g, is set by a thermostatic water bath (Grant Instruments,

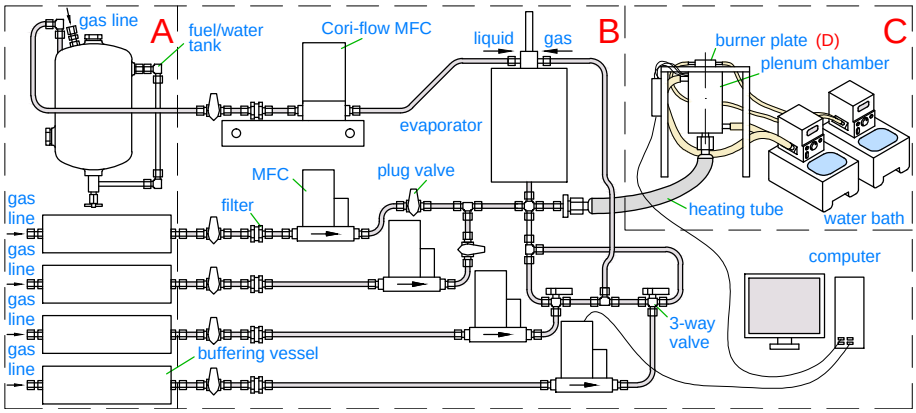

Figure 2.4: *Schematic of the experimental setup (Panel 1, not to scale).*

model GD120), which creates a circuit around the plenum chamber. The second water bath keeps the temperature of the burner plate at (typically) 368 K through a heating jacket on the burner head, as shown in a schematic of the burner in Figure 2.5.

The design of the burner head, presented in Figure 2.5, largely repeats the design introduced in [58]. A 2 mm thick brass burner plate, perforated with 0.5 mm diameter holes at a pitch of 0.7 mm, is attached to the burner head with thermal paste. The hotter top part of the burner head is thermally insulated from the bottom part and from the plenum chamber via a ceramic ring. The temperature distribution in the burner plate is monitored by eight thermocouples (TC), each of them occupying a hole in the burner plate.

In the heat flux method, adiabatic conditions are achieved when the heat

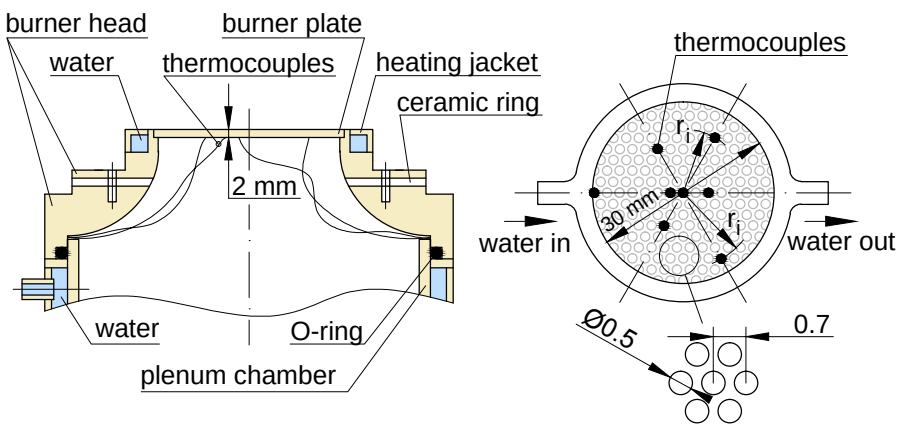

Figure 2.5: *Cross-section and top view of the heat flux burner head designed by Eindhoven University of Technology.*

loss to the burner from the flame, necessary for its stabilization, is compensated by the heat gain to the unburned mixture as it enters the preheated burner plate. Van Maaren et al. [62] developed an analytical expression for the radial temperature distribution in the burner plate, which was later presented [65] in a simplified form:

$$\bar{T_p}(r) = T_{center} - \frac{q}{4\lambda h} r^2 = T_{center} + C \cdot r^2 \tag{2.14}$$

where T_{center} is the temperature of the central point, q is the net external heat transfer per unit area to (from) the burner plate, λ is the thermal conductivity of the plate in radial direction and h is the thickness of the plate. The net heat transfer q is the difference between the heat gain to the burner plate from the flame (q_+) and the heat loss to the preheating gas (q_-), i.e.:

$$q = q_+ - q_- \tag{2.15}$$

The quantity $-q/(4\lambda h)$ is called the parabolic coefficient, C, and it is the key parameter of the method. It is obtained from the measured temperature distribution in the burner plate by fitting it to Eq. (2.14). Consequently, when the unburned gas velocity V_g is adjusted, it affects q, and adiabatic conditions, i.e. $q = 0$, can be identified by observing a uniform temperature profile in the burner plate (Eq. (2.14)). The state with $C < 0$, $V_g < S_L$ is called sub-adiabatic, and the opposite conditions are super-adiabatic. The laminar burning velocity, S_L, is calculated by interpolation of the recorded parabolic coefficient dependence on the average unburned gas velocity V_g. The latter is obtained when the total flow rate set by the MFCs is divided by the cross section of the flow, A:

$$V_g = \frac{p_0}{p} \cdot \frac{T_g}{T_0} \cdot \frac{\Phi_{tot}}{A} \tag{2.16}$$

where Φ_{tot} in $\mathrm{L_n/min}$ is converted to the volumetric flow rate using the unburned gas temperature T_g and ambient pressure p. The total flow rate Φ_{tot} is calculated by the LabVIEW script using its relation to V_g (Eq. (2.16)). The flow rates of each mixture component are set by the LabVIEW script based on the specified value of the equivalence ratio ϕ. Consider the stoichiometric reaction:

$$\begin{aligned} &\textstyle\sum_i f_i \, C_{x_i} H_{y_i} O_{z_i} N_{v_i} + \phi \left(\sum_j o_j \, O_{a_j} ... \right) + ... \\ &= \left(\textstyle\sum_i f_i x_i \right) CO_2 + \frac{1}{2} \left(\textstyle\sum_i f_i y_i \right) H_2O + ... \end{aligned} \tag{2.17}$$

where the ellipses correspond to any components other than oxygen in the oxidizer and to the inert components in reactants and products (e.g., N_2, Ar or He), f_i and o_j are the flow rates of the fuel and oxidizer components, and ϕ is the proportionality coefficient, equal to the equivalence ratio:

$$\phi = \frac{2\sum_i f_i x_i + \frac{1}{2}\sum_i f_i y_i - \sum_i f_i z_i}{\sum_j o_j a_j} \tag{2.18}$$

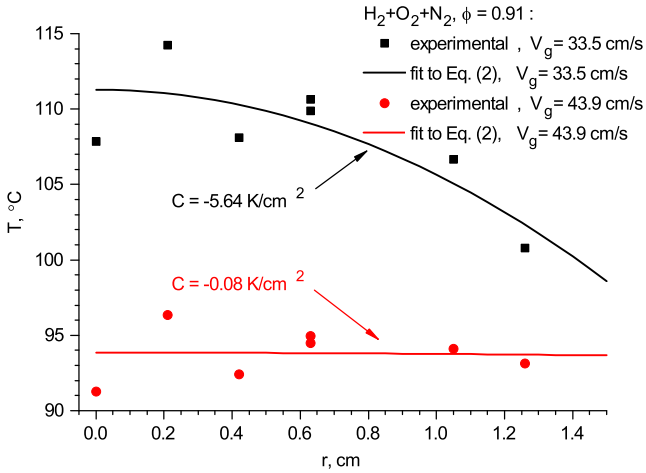

Figure 2.6: *Temperature distribution in the burner plate for an $H_2 + O_2 + N_2$ flame ($O_2/(O_2 + N_2) = 0.1077$) at $\phi = 0.91$, $T_g = 318$ K and $V_g = 33.5$ cm/s (black), $V_g = 43.9$ cm/s (red). Symbols: experimental, line: parabolic fit to Eq. (2.14).*

Using Eq. (2.18), the flow rates f_i and o_j can be readily calculated through the total fuel and oxidizer flows, $f = \sum_i f_i$ and $o = \sum_j o_j$, if the fractions $n_{f_i} = f_i/f$ and $n_{o_j} = o_j/o$ are specified. In the formulation of Eqs. (2.17, 2.18), $a_j = 0.42$ for air.

Determination of the laminar burning velocity in flat flames stabilized at adiabatic conditions is carried out by obtaining the parabolic coefficient C (Eq. (2.14)) as a function of the inlet gas velocity V_g. To illustrate this procedure, Figure 2.6 (taken from Paper III) shows two radial temperature profiles in the burner plate during the measurements in an $H_2 + O_2 + N_2$ mixture with $O_2/(O_2 + N_2) = 0.1077$ at $\phi = 0.91$ and $T_g = 318$ K. The profiles correspond to sub-adiabatic conditions ($V_g = 33.5$ cm/s, $C = -5.64$ K/cm^2) and conditions near the adiabatic state ($V_g = 43.9$ cm/s, $C = -0.08$ K/cm^2). The lines in Figure 2.6 represent the fits of the experimental temperature profiles to Eq. (2.14), obtained via linear regression in T-r^2 coordinates. At the edge of the burner plate, i.e. at $r = 1.5$ cm, both lines are close to $T = 95$ °C, which is the set temperature of the heating water jacket. At sub-adiabatic conditions, the temperature increases towards the center of the burner plate.

In a typical heat flux experiment, after recording the $C(V_g)$ dependence, the location of $C = 0$, $V_g = S_L$ is found by linear interpolation of the points in the vicinity of this state, but in some cases, extrapolation from sub-adiabatic conditions is necessary. Figure 2.7 from Paper III illustrates the process for the same mixture as in Figure 2.6 at two temperatures: $T_g = 298$ K and $T_g = 318$ K. The points used for S_L determination are fitted linearly, as shown by the thick green lines. At $T_g = 298$ K, S_L is obtained by interpolation. At 318 K, the flames showed some instabilities around adiabatic conditions. Therefore, the super-adiabatic point $V_g = 45$ cm/s was not included into the

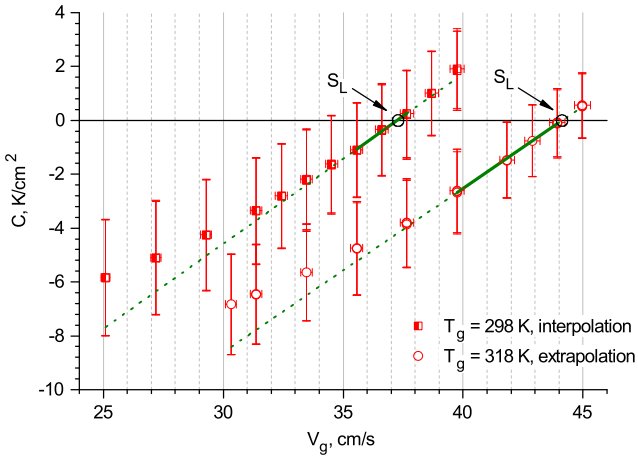

Figure 2.7: *Determination of S_L from the $C(V_g)$ dependence for the H_2 + O_2 + N_2 flame with $O_2/(O_2 + N_2)$ = 0.1077 at ϕ = 0.91 and T_g = 298 K and 318 K.*

fitting domain, and S_L was obtained by extrapolation. Green dotted lines show extrapolation of the fitted line to all recorded points with the aim to visualize the behavior of $C(V_g)$ at sub-adiabatic conditions.

2.1.3.2 Safety precautions

The experimental setup depicted in Figure 2.4 is operated in open air in the lab with a point-wise suction ventilation placed above the burner. Yet, when gases or liquids are noxious, the experiments are performed on Panel 2, which is placed in a ventilated fume cupboard. The major safety concern for the measurements on the heat flux burner is flashback, which may occur if the mixture composition deviates from the set parameters. A typical perforation of the burner plate of 0.5 mm is below the quenching diameter for most of the hydrocarbons burning in air. However, it is not the case for mixtures with pure oxygen [63]. Therefore, if the oxidizer mixture is formed by its pure components, i.e. with separate channels for O_2 and diluent gas, compositions with increased oxygen concentration could be formed as a result of two unwanted scenarios:
a) the response time of the MFCs is not the same, and older MFCs might react slower. Thus, if all MFCs are not opened simultaneously when generating a combustible mixture, the first mixture pocket might be mostly fuel + oxygen. If the flame is ignited immediately, it can propagate backwards into the plenum chamber and cause explosion.
b) if the inert component is completely consumed in the gas bottle. The decrease of the flow is rapid. Therefore, if no risk reducing measures are performed, the operator should constantly monitor the pressure regulators or the temperature of the burner plate, because if oxygen fraction in the mixture is

increased, the flame may flash back or the burner plate might be damaged due to overheating.

To reduce the risk of unwanted gas mixture compositions, the LabVIEW interface controls the ratio between the measured flow rates of O_2/fuel and inert components, and if it goes above a certain value, the script will shut the O_2 MFC. On the other hand, this critical ratio depends on the studied conditions, and in addition, a decrease of pressure and flow can occur quite fast when the gas is run out. Therefore, a configuration with pressure gauges between the MFC and the buffering vessel seems to be advantageous – in that case, potential loss of flow is detected at least about 10 seconds before it occurs.

To avoid the issues related to the MFC response time prior to ignition, the LabVIEW script always sets the flow of the inert component first and waits until it is reached. When changing flame conditions, the script performs it gradually with several intermediate steps and controls that all flows reach them. Apart from the risks related to the oxidizer mixture, the script also reduces the risks related to the fuel, e.g., in experiments with hydrogen flames, where rapid change of one of the flow components may create a temporary mixture of high or low reactivity. This can result in a flashback or a blow off, respectively. At the end of experiments, the installation is flushed by nitrogen or air, so that combustible mixture is not stored in the plenum chamber. Liquid fuel from the tank is removed and the fuel line is rinsed with C_2H_5OH to prevent corrosion of the O-rings and consequently, clogging of the C.E.M. and gas lines.

2.1.3.3 Experimental uncertainties

The accuracy of the laminar burning velocity measurements can be affected by numerous factors related to the experimental setup and procedure. They are summarized in Table 2.2. For convenience of understanding, they were sorted by their appearance from upstream of the flow. Following the notation in Figure 2.4, Factors 1-3 can thus be attributed to liquid and gas preparation (A), Factors 4-5 to the mixing panel (B), Factors 6-8 to the temperature control (C) and, finally, Factors 9-22 are related to the burner head and the flame (D). The approximate effect on S_L for each factor is given for typical burner system and mixtures, specifying which parameters each of the uncertainty factors depends on. For more details and accurate quantification of ΔS_L, the reader is addressed to Paper V. Some of the factors have been comprehensively studied in literature (1,9,10,14,15,17,18,19,21), and they are only briefly outlined in Table 2.2. The table presents references to the main sources, where the influence of the factors was studied and quantified, and a more comprehensive review can be found in Paper V. Table 2.2 also summarizes possible methods to control or evaluate each of the uncertainty factors. If the influence on S_L from a particular factor cannot be uncoupled from another one, or the influence of several factors can be controlled altogether, references are made between different factors presented in the table.

Table 2.2: *Uncertainty factors in the heat flux measurements.*

No.	Factor	ΔS_L	Note	Method to control or investigate	Ref.
1	fuel hygroscopicity	negligible		chemical analysis	[64]
2	fuel purity		fuel-specific		
3	air composition	see text	depends on O_2/N_2 blending method	measurements in O_2 + N_2 mixtures	
4	MFC	$\sim 1\%$	depends on MFC calibration method	calibration of the MFC	
5	instability of C	negligible	only for liquid fuel, depends on evaporation system, estimate by Eq. (2.24)	selection of appropriate evaporator range	
6	mixing	< 0.15 cm/s	estimate coupled with daily variations in S_L	heating hose, long tube	Pap.V
7	T_g	0.3-2%	mixture-specific	TC in the flow	
8	p	$\sim 1\%$	mixture-specific, error of $\sim 1.5\%$ for previous measurements	record pressure in the room	
9	burner head insulation	negligible	insulation of the burner head is necessary	together with No. 10	[65]
10	$\Delta T = T_{hj} - T_g$	negligible	increased error for T_{hj}–$T_g < 30$ K	change T_{hj}	[66]
11	TC scattering	see text	burner- and mixture-specific, estimate by Eqs. (2.28, 2.29)	note maximum temperature difference at $C = 0$	
12	TC perturbation	unclear	depends on TC type and wire width	together with No. 10	
13	burner plate attachment	together with No. 22		together with No. 22	
14	radical loss	negligible			[66, 67]
15	V_g uniformity	~ 0.5 cm/s	depends on V_g and burner diameter	change diameter of the burner	[68, 69]
16	surface area	see text	burner-specific, can be compensated for	estimate surface area based on perforation pattern	
17	air entrainment, radial diffusion	negligible	depends on $S_L(\phi)$	together with No. 15, change ambient atmosphere	[59]
18	perforation	$\sim 0.5\%$	burner-specific, varies with V_g	CFD simulation	[70]
19	stretch	negligible			[62, 68]
20	cell formation	see text	mixture-specific, dep. on $\Delta T = T_{hj} - T_g$	confirm linearity of C, use Eq. (2.35)	
21	radiation	< 0.5 cm/s	mixture-specific	kinetic modeling	[71]
22	asymmetric heat flux	up to 2-3 cm/s	burner-specific	check symmetry of the TC readings	

Air composition, No. 3

For the measurements of the burning velocity of fuel + air mixtures, the air can be obtained in three different ways: a) compressed atmospheric air, b) factory-blended O_2 + N_2 mixture of known composition in gas bottles, and c) mixture of O_2 and N_2 blended during the measurements. The uncertainty in the dilution ratio, $O_2/(O_2 + N_2)$, might have an influence on S_L. Burke et al. [72] showed by experiments and detailed modeling that by altering the dilution ratio as 0.21±0.005, the burning velocity of propene + air flames changes by ±2.5 cm/s. The uncertainty of ±0.005 is stated for the synthetic air from AGA Gas AB used in Lund. However, the actual O_2 fraction, obtained with a Rosemount OXYNOS 100 analyzer, was found to be in the interval 0.21±0.0007, comparable to the drift of the analyzer during the day. Also, for the measurements on the same burners over a long time, i.e. using different gas bottles, no significant changes were observed. Naucler et al. [71] measured S_L of CH_3OH + O_2 + CO_2 flames, with oxidizer mixture blended at the factory and produced during the experiments. Very consistent results were observed, indicating that in practical situations, the deviations from the nominal composition in the factory-blended mixtures (AGA Gas AB) are lower than the stated uncertainty. For the air obtained by mixing O_2 and N_2 during the measurements, a 1.2% error in the flows of pure components was estimated (see below). Then the resulting uncertainty in the dilution ratio is 0.21±0.0028, about 2 times less than that evaluated by Burke et al. [72]. Dyakov et al. [59] observed a difference in CH_4 + air burning velocity of about 0.6-1.4 cm/s between the dry compressed air and the O_2 + N_2 mixture produced on site.

Flow control, No.4

The gas velocity is proportional to the total flow rate Φ_{tot} according to Eq. (2.16). Consequently, the uncertainty in S_L due to the flow rate measurement is:

$$\Delta S_L^{MFC} = S_L \frac{\Delta\Phi_{tot}}{\Phi_{tot}} = S_L \frac{\sqrt{(\sum \Delta\Phi_i)^2}}{\Phi_{tot}} \tag{2.19}$$

where $\Delta\Phi_{tot}$ is the uncertainty in Φ_{tot} and $\Delta\Phi_i$ are the uncertainties in the flow rates of each mixture component "i". Here, the square sum rule was used to determine $\Delta\Phi_{tot}$. The gas MFCs have to be calibrated prior to measurements. For the data reported in the present work, MesaLabs DryCal Definer 220 and Defender 530 positive displacement flow meters were used for calibration. Calibration curves in the form of third or fourth degree polynomials are introduced into the LabVIEW operating program and used for the correction of the flow rates before they are sent to MFCs. The calibration is always performed with the gas to be used in the measurements, as discussed in detail in Paper V. The uncertainty $\Delta\Phi_i$ in the flow rate of each gas component is a sum of 1% stated accuracy of the Definer 220 plus the stated flow repeatability of the MFC, which equals to 0.2% for Bronkhorst thermal flow controllers, so that:

$$\Delta\Phi_i = \pm 0.012\Phi_i \tag{2.20}$$

For the liquid components, due to higher reliability of the Coriolis flow meters,

the stated accuracy of the M13 Cori-Flow can be used:

$$\Delta\Phi_i = \pm(0.002\Phi_i + 0.5 \text{ g/h}) \tag{2.21}$$

then converted to L_n/min. Since the flow of oxidizer constitutes a major fraction of the total flow, then ΔS_L^{MFC} is generally around 1% (see Eqs. (2.19,2.20)).

For the uncertainty in the equivalence ratio, defined as Eq. (2.17), the error propagation rule gives the following expression:

$$\frac{\Delta\phi}{\phi} = \sqrt{\frac{\sum_i \left[\left(2x_i + \frac{1}{2}y_i - z_i\right)\Delta f_i\right]^2}{\left(2\sum_i f_i x_i + \frac{1}{2}\sum_i f_i y_i - \sum_i f_i z_i\right)^2} + \frac{\sum_j \left(a_j \Delta o_j\right)^2}{\left(\sum_j o_j a_j\right)^2}} \tag{2.22}$$

where Δf_i and Δo_j are the uncertainties in the flows of the fuel components "i" and the oxidizer components "j", respectively. For a single-fuel, single-oxidizer mixture Eq. (2.22) reduces to:

$$\frac{\Delta\phi}{\phi} = \sqrt{\left(\frac{\Delta f}{f}\right)^2 + \left(\frac{\Delta o}{o}\right)^2} \tag{2.23}$$

For gaseous fuels $\Delta\phi$ becomes equal to 1.7% according to Eqs. (2.20, 2.23).

Even though the uncertainty in the flow rate after calibration is comparable to the MFC stated accuracy, it is important to calibrate the MFCs, as was first pointed out by van Maaren and de Goey [68]. The flow rates can drift from the nominal values over time well beyond stated accuracy, and even show day-to-day variations as observed by Dyakov et al. [59]. Dirrenberger et al. [73] observed a jump in the C_2H_6 + air burning velocity measured with MFCs of different capacity. Konnov et al. [64] used two calibrated MFCs to produce the air flow. By varying the ratio of the flows between the two channels, S_L changed by 0.7 cm/s at most, within the uncertainty range of the measurements [64]. Therefore, the systematic drifts of the MFCs from nominal values can be successfully eliminated by calibration. For the Lund setups, it was observed that the measured flow rates can drift by about 1% over long periods of time, which was also confirmed by using a Ritter TG10 drum-type gas meter with 0.5% stated accuracy. Therefore, a more conservative error of 1% of Definer 220, used for calibration before each experimental campaign, was found to be acceptable. The drift from the factory settings for Bronkhorst thermal MFCs was generally found to be higher than 1%, again, indicating the importance of calibration.

Stability of the liquid flow, No. 5

When the measurements involve liquid fuels, operation of the evaporator (C.E.M.) may introduce oscillations in the fuel flow, higher than those for the gaseous components, thus resulting in changes in ϕ and consequently, in the instant S_L value and the measured parabolic coefficient C. The oscillations increase for low flow rates (relative to the evaporator capacity). Since

the burning velocity is obtained by linear regression of the recorded $C(V_g)$ dependence, the uncertainty in the determination of C at $V_g = S_L$ by the regression equation can be calculated at a confidence level of 95% using basic statistics [74]:

$$\Delta C = t_{0.025,n-2} \cdot \sqrt{\frac{\sum_{i=1}^{n}(C^i - s \cdot V_g^i - C_0)^2}{n-2} \left(\frac{1}{n} + \frac{n(S_L - \overline{V_g})^2}{n \sum_{i=1}^{n}(V_g^i)^2 - \left(\sum_{i=1}^{n} V_g^i \right)^2} \right)} \tag{2.24}$$

where V_g^i and C^i are the measured gas velocities and parabolic coefficients, respectively, in the velocity domain selected for S_L determination, while n is the number of measured points, $\overline{V_g}$ is the mean of the gas velocities, $s \cdot V_g^i - C_0$ is the linear regression for the $C(V_g)$ dependence (as in Figure 2.7), and $t_{0.025,n-2}$ is the value of t-distribution for one-sided 2.5% probability and $n-2$ degrees of freedom. Then ΔC is divided by the regression coefficient s, or parabolic coefficient sensitivity, to obtain the estimated error in S_L. This value generally appears to be negligible for the large Bronkhorst W303-A 1200 g/h evaporator (below 0.1 cm/s) provided that the fuel flow is above 5-10% of the evaporator capacity and the sample size is large. However, care should be taken since the approach assumes that the oscillations are unbiased, i.e. the flow of liquid averaged in time matches the set value of the Cori-Flow. The described approach was first used by Naucler et al. [71].

Artificial oscillations of the liquid flow measured by the Coriolis MFC were observed by Sileghem et al. [75], which were found to be caused by vibrations of the mixing panel introduced by motors in the water baths. It is therefore advised to place water baths on a table separated from the mixing panel. In addition to that, to reduce oscillations, evaporators of smaller capacity should be used, if possible.

Unburned mixture temperature control, No. 7

The unburned gas temperature T_g is set by the thermostatic water circuit in the plenum chamber. As described by Bosschaart and de Goey [58], the heat transfer to the unburned mixture occurs not only through the walls of the plenum chamber, but also through the perforated distributor plate installed at the bottom inlet. Effective temperature control would imply that the gas mixture approaching the burner plate has the same temperature independent on the temperature it had when entering the plenum chamber and that this temperature is equal to the temperature of the water circulating in the jacket of the plenum chamber. Konnov et al. [64] reported that S_L was not influenced by changing the C.E.M. temperature from 363 K to 403 K, which would in turn affect the gas temperature at the inlet of the plenum chamber, and concluded that the temperature control is efficient. To actively monitor the unburned gas temperature, an additional thermocouple can be installed inside the burner head [76, 77], or gas temperature can be measured outside the burner in cold flow experiments [59]. Dyakov et al. [59] reported an error of 2 K for their

measurements at 298 K and the same value was obtained by Gillespie et al. [76] for unburned gas temperatures ranging from 298 to 398 K. While the issue of temperature control probably requires more thorough investigation in a wide range of velocities and unburned gas temperatures, the use of the heating hose seems to be advantageous also for controlling T_g.

The uncertainty in T_g directly affects the burning velocity. The gas velocity V_g is determined by Eq. (2.16), thus V_g is proportional to T_g. At the same time, the burning velocity depends on temperature according to the empirical power law of Eq. (1.1). Therefore, if real unburned gas temperature in the experiments was $T_g^{set} + \Delta T_g$, then, according to Eqs. (1.1, 2.16), i.e., taking into account changes in both gas velocity and flame speed, the burning velocity at the desired (set) temperature T_g^{set} is proportional to $(T_g^{set} + \Delta T_g)^{1-\alpha}$. Consequently, the uncertainty in the burning velocity is:

$$\frac{\Delta S_L}{S_L} = (1-\alpha)\frac{\Delta T_g}{T_g} \tag{2.25}$$

For stoichiometric hydrocarbon mixtures, $\alpha \approx 1.5$, thus assuming ΔT_g to be 2 K, the resulting error in S_L is about 0.3%, which can be considered negligible. However, in mixtures closer to flammability limits, α can reach higher values of 3-4 as observed in Paper III, and in that case, for the same error of 2 K, the uncertainty in S_L increases to about 2%.

Atmospheric pressure variations, No. 8

The exact pressure of the unburned gas of $p_0 = 1$ atm cannot be set during measurements. In reality, burning velocity at pressure $p = p_0 + \Delta p$ is measured. Pressure dependence of the burning velocity can be written in the same way as the temperature dependence of Eq. (1.1):

$$S_L = S_L^0 \cdot \left(\frac{p}{p_0}\right)^{\beta} \tag{2.26}$$

where β is the pressure power exponent. Using the same approach as for unburned gas temperature, it can be written:

$$\frac{\Delta S_L}{S_L} = -\beta\frac{\Delta p}{p} \tag{2.27}$$

In Eq. (2.27), however, Δp is not the uncertainty in pressure, but the difference between the actual pressure and $p_0 = 1$ atm. Again, considering that for hydrocarbons β is rarely lower than -0.5 [78], for atmospheric pressure variations of 2% ($\sim$20 hPa), the upper estimate for the day-to-day variations of the burning velocity is $\pm 1\%$.

TC scattering, No. 11

The scatter in thermocouple readings together with the mass flow control are generally seen in the literature as main factors contributing to the total uncertainty of the laminar burning velocity. Bosschaart and de Goey [58] were the first to estimate how S_L is affected by the TC accuracy σ_{TC}. They

estimated σ_{TC} as deviations from the parabolic fit of Eq. (2.14) and got a value of 0.5 K after correcting the TC readings for the difference in their vertical positions. Their value of σ_{TC} is comparable to a typical type-T thermocouple accuracy of 0.5-1 K [79].

For the Lund burners, the observed scatter generally exceeded 0.5 K (see Figure 2.6) and was found not to be related to the vertical positions of TCs as was suggested in [58]. On the other hand, the original approach of [58] might overestimate the uncertainty in S_L as explained in Paper V. Therefore, a different approach was used, recently presented by the Lund group [80]. Since C is obtained from linear regression of the measured burner plate temperature as a function of the squared radius r^2 (Eq. (2.14)), the standard error of C was considered as its uncertainty, σ_C:

$$\sigma_C = \sqrt{\frac{\frac{1}{n-2}\sum_{i=1}^{n}(T_i - C\cdot(r^2)_i - T_{center})^2}{\sum_{i=1}^{n}\left[(r^2)_i - \overline{(r^2)}\right]^2}} \tag{2.28}$$

where n is the number of TCs, T_i are TC readings at radii r_i, and $\overline{(r^2)}$ is the average of the squared radii. Then the uncertainty in S_L due to scatter in TCs becomes:

$$\Delta S_L^{TC} = \frac{\sigma_C}{s} \tag{2.29}$$

where s is the parabolic coefficient sensitivity:

$$s = \left.\frac{dC}{dV_g}\right|_{V_g=S_L} \tag{2.30}$$

which is the slope of the curves in Figure 2.7 at $V_g = S_L$.

The parabolic coefficient uncertainty calculated with Eq. (2.28) is a characteristic of the burner, since it was found to be practically constant for different fuels (as was concluded based on a series of measurements with CH_4, CH_3OH and C_2H_5OH on the same burner as well as from previously reported data [75,80]). The difference in ΔS_L^{TC} in each measurement is therefore related to the varying sensitivity, s, of the parabolic coefficient.

It was shown that s changes with the burner plate material [65], geometrical parameters (Eq. (2.14)), and equivalence ratio [81]. In addition, s is weakly dependent on the type of the fuel for the case of lower alkanes [81]. The assumption of local linearity of $C(V_g)$ is sufficient for S_L determination provided that the flame is stable at the adiabatic conditions. However, as can be inferred from Figure 2.7, as well as from the results presented by Bosschaart and de Goey [58] and by Knorsch et al. [82], $C(V_g)$ becomes non-linear far below the adiabatic conditions, with decreasing sensitivity s.

Bosschaart and de Goey [83] developed an analytical expression for s based on Zeldovich theory of flame propagation [84], and it was found to be dependent on several flame and burner plate characteristics including adiabatic flame

temperature T^{ad} and Zeldovich number Ze. To connect the analysis to the experimental data found with the method, an alternative is more useful in practice. In the following, the $C(V_g)$ and s will be derived based on the idea of Botha and Spalding [85] who suggested that the heat transfer to the burner is equivalent to pre-cooling of the initial mixture if no reactions occur upstream of the burner surface, and that any sub- or super-adiabatic flame is equivalent to an adiabatic flame at another initial temperature. From Eq. (2.14), the total amount of heat transferred to the burner, Q:

$$Q = -4\lambda h A \cdot C \tag{2.31}$$

where A is the flame surface area. Q is equal to the heat released from cooling the initial mixture by temperature ΔT:

$$Q = -\frac{\dot{m}}{M} c_p^{\nu} \cdot \Delta T = -\frac{p_0}{R T_g} V_g A \cdot c_p^{\nu} \cdot \Delta T \tag{2.32}$$

where $\dot{m}$ is the total mass flow, M and c_p^{ν} are the initial mixture molar mass and molar heat capacity, respectively, and R is the gas constant. At the same time, the non-adiabatic flame with heat loss Q is equivalent to the adiabatic flame at the temperature $T_g' = T_g + \Delta T$. Therefore, the common power-law temperature dependence of the burning velocity can be used (Eq. (1.1)):

$$S_L' = S_L \left(\frac{T_g + \Delta T}{T_g} \right)^{\alpha} \tag{2.33}$$

where S_L and S_L' are the burning velocities at temperatures T_g and T_g', respectively. Finally, since the total mass flow is constant, then:

$$\frac{S_L'}{T_g + \Delta T} = \frac{V_g}{T_g} \tag{2.34}$$

Combining Eqs. (2.31-2.34), the parabolic coefficient C becomes equal to:

$$C = \frac{p_0}{4\lambda h R} \cdot c_p^{\nu} \cdot V_g \left[\left(\frac{V_g}{S_L} \right)^{\frac{1}{\alpha - 1}} - 1 \right] \tag{2.35}$$

and the sensitivity s at $V_g = S_L$ (see Eq. (2.30)):

$$s = \left. \frac{dC}{dV_g} \right|_{V_g = S_L} = \frac{p_0}{4\lambda h R} \cdot c_p^{\nu} \cdot \frac{1}{\alpha - 1} \tag{2.36}$$

In the derivation of Eqs. (2.35, 2.36) it was assumed that presence of the burner plate does not change the flame properties, and that Eq. (2.14) is valid outside the near adiabatic conditions. For stoichiometric hydrocarbon-air flames, $\alpha \approx 1.5$, therefore, the dependence $C(V_g)$ is approximately a third order polynomial according to Eq. (2.35). However, α can increase significantly at other equivalence ratios, which results in a decrease of s in lean or rich flames observed in, e.g., [81]. While $\alpha = 1$ is a special case, since Eq. (2.36) would

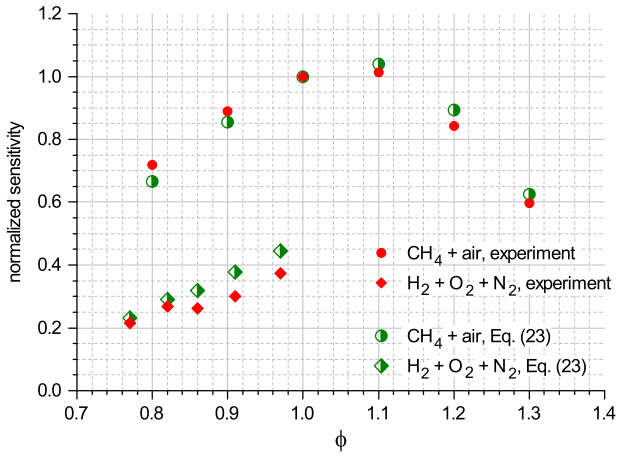

Figure 2.8: *Comparison of the parabolic coefficient sensitivities obtained from experimental $C(V_g)$ dependencies and by using Eq. (2.36).*

suggest infinitely large sensitivity, mixtures with such α, e.g. H_2 + O_2 (see Section 3.2.3), are not accessible for the heat flux measurements. For error estimation, the practical range of α can be considered to be $\alpha \geq 1.5$.

Equation (2.36) also reveals the power exponent α as the main parameter determining the accuracy of the burning velocity measurements for a specific burner, characterized by λ and h. The intrinsic non-linearity of the $C(V_g)$ dependence described by Eq. (2.35) becomes important when adiabatic conditions $V_g = S_L$ are not attainable due to, e.g., cell formation, as will be discussed below.

To check the validity of Eq. (2.36), the sensitivities s, obtained in experiments (as the slopes of $C(V_g)$ in Figure 2.7) and by using Eq. (2.36), are compared in Figure 2.8 (taken from Paper V) for CH_4 + air flames and H_2 + O_2 + N_2 mixtures ($O_2/(O_2 + N_2) = 10.77\%$). While the calculated absolute values were found to be about 30% lower than the experimental results for CH_4 + air mixtures, a good agreement holds for normalized quantities. In Figure 2.8, all sensitivities were normalized by the corresponding values in stoichiometric CH_4 + air mixtures. Thus, Eq. (2.36) can be used for approximate estimation of s or for prediction of ΔS_L^{TC} for a particular burner. In the calculations of the absolute values, the thermal conductivity of the burner plate $\lambda = \lambda_{br} \cdot \epsilon$, where λ_{br} is the thermal conductivity of brass and geometrical constant ϵ is equal to 0.362 for burners with 0.5 mm holes and 0.7 mm pitch, as discussed by van Maaren et al. [62].

Based on the above, the uncertainty in S_L due to scatter in measured temperatures depends on mixture properties, burner plate material, thickness and perforation pattern, as well as the quality of the TC attachment. Therefore, ΔS_L^{TC} can vary in each case. To give some typical values, for the burner with

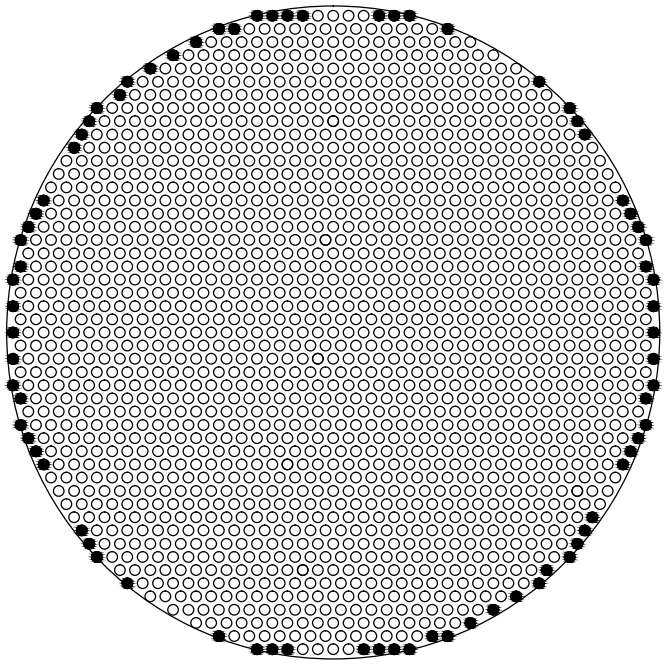

Figure 2.9: *Difference in perforation patterns for the two TU/e burner designs (denoted by filled holes).*

2-mm burner plate and hole diameter of 0.5 mm, used in the present work for determination of the burning velocity of lean H_2 + air mixtures (Paper III), $\Delta S_L^{TC} \approx$ 0.7-1.3 cm/s in CH_4 + air flames at ϕ = 0.7-1.3, lowest at around stoichiometry. For the burner designed at Zhejiang University (see, e.g. [86]), which has the same perforation pattern and burner plate thickness, $\Delta S_L^{TC} \approx$ 0.2-0.3 cm/s at the same conditions due to much lower temperature scatter. The uncertainty increases in mixtures with higher temperature exponent α (see Eq. (2.36)), e.g., in lean H_2 + air, as described in detail in Paper III.

Surface area, No. 16

Apart from the uncertainty in the flame properties at the edges, the perforation pattern at the border of the burner plate can affect the total flame surface area. The burners produced by the Eindhoven University of Technology (TU/e) with 0.5 mm holes have two different perforation patterns at the border of the burner plates as shown in Figure 2.9 (taken from Paper V), where the holes not drilled in the second design are denoted by filled circles. It was discovered that the effective surface area A for the second design is about 5% lower than the inner cross section. This could potentially affect the gas velocity V_g, and consequently, the measured value of S_L.

A dedicated experiment was performed to test how S_L is affected. The burning velocity was measured on the burner of design 1, then the border holes were blocked with a thermal paste (Electrolube EHTSP50T), the same

Table 2.3: *Difference in S_L for the partly blocked burner plate.*

ϕ	0.7	0.8	0.9	1	1.1	1.2	1.3
$\Delta S_L, \%$	-8.61	-8.6	-8.36	-8.17	-8.14	-7.85	-7.48

that is used to attach the burner plate, and S_L was measured again. Finally, the burner head was disassembled, photographed, and the difference in the surface area was calculated. The decrease of the measured value of burning velocity for CH_4 + air flames is presented in Table 2.3, and the surface area difference was estimated to be about 8.5%. Some of the holes, however, appeared to be only partially blocked. Therefore, this estimate involves some uncertainty. The results indicate that V_g is indeed inversely proportional to the open area of the burner plate. It can be also noted that difference in S_L in Table 2.3 systematically decreases with ϕ. While this behavior can be attributed to the edge effects, or to the partial blocking, it is still within the typical uncertainty intervals for heat flux measurements. However, the origin of this systematic behavior and its influence on S_L should be studied together with the issues related to V_g uniformity (uncertainty factor No. 15) in wider range of conditions. Such investigation could include the use of burner plates of different diameters.

The observed difference of S_L for an unblocked and a partly blocked burner plates suggests that the surface area of the perforation should be used in Eq. (2.16) for the determination of V_g. The difference in surface area for the burner used in the present study for determination of H_2 + air burning velocity was carefully measured. Assuming that the gas jets exiting the outer holes expand to the same amount as for the inner holes, the decrease in the surface area was found to be $\Delta A = 5.25\%$. That means that some of the previously published burning velocities have to be increased by $1/(1–\Delta A) = 5.5\%$. A complete list of measurements on the burner of the second design is presented and discussed in Paper V.

Flame stability and extrapolation, No. 20

The issue of flame stability is attributed to cell formation, which affects the burning velocity measurements in case when cellular structures are formed near the adiabatic conditions, making it impossible to find S_L by interpolation. Cell formation on a heat flux burner was first investigated experimentally by Konnov and Dyakov [87–89] in the flames of CH_4, C_2H_6, C_3H_8 burning in oxy-fuel oxidizing atmosphere (O_2 + CO_2). They showed that the propagation speed of adiabatic cellular flame is higher than the laminar burning velocity due to increase of the flame surface area. It was also concluded that the structure of the cells was not related to the perforation pattern of the burner. However, increasing the temperature difference between the burner plate and the unburned gas mixture can suppress cell formation, due to stabilizing effect of the burner when flame moves closer to it. This effect was also confirmed numerically [90]. Later, cell structures were observed in oxy-fuel mixtures of CH_3OH [71], CH_4 + H_2 [91], H_2 + CO [92, 93] and H_2 [94]. For the mixtures

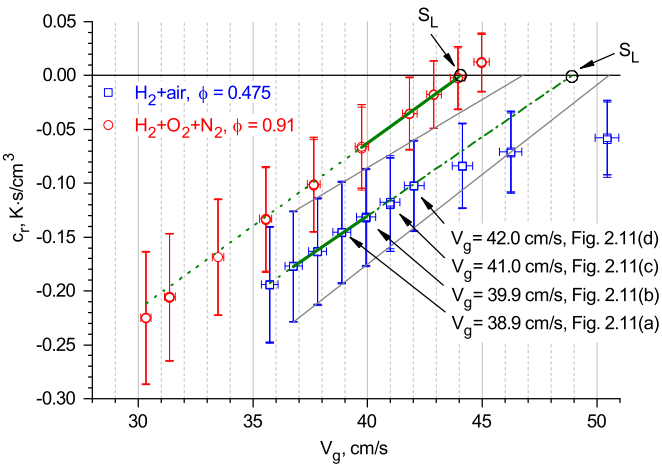

Figure 2.10: *Determination of S_L from the c_r dependence for H_2 + air flame at 318 K and $\phi = 0.475$ (blue) and H_2 + O_2 + N_2 flame with $O_2/(O_2 + N_2) = 0.1077$ at 318 K and $\phi = 0.91$ (red).*

of syngas [92] and hydrogen (Paper III), cellular flames were also observed for oxidation in air.

If the laminar burning velocity has to be determined when adiabatic conditions are not accessible due to cell formation, the parabolic coefficient dependence $C(V_g)$ can be extrapolated from flat sub-adiabatic flames ($C < 0$, see Figure 2.7) as was first reported by Sileghem et al. [80]. However, care should be taken due to non-linearity of $C(V_g)$, as follows from Eq. (2.35) and Figure 2.7. Naucler et al. [71] performed extrapolation assuming local linearity, since the extrapolation range (the difference between the highest achievable V_g and the derived S_L) never exceeded 2 cm/s. On the contrary, the measurements in lean H_2 + air flames required extrapolation in much longer velocity intervals.

A modified method of the data processing was used in the present study. Instead of directly plotting C as a function of V_g, a normalized relative quantity $c_r = C/V_g$ was used. The approach is based on the work of Botha and Spalding [85], who used a porous plug burner and determined S_L by recording the amount of heat transferred from the flame to the cooling water. The data were then extrapolated to zero loss conditions. They plotted the heat loss normalized over the volume of fuel and found that the obtained curves were linear in very wide ranges of cold gas velocities. For the case of the present study, this quantity is equivalent to c_r since $C \sim q$ and V_g is proportional to the volumetric fuel flow for a given ϕ and T_g.

Examples of the procedure of S_L determination from the measured c_r data is illustrated in Figure 2.10 (from Paper III) for two cases: H_2 + air flame with $\phi = 0.475$ and H_2 + O_2 + N_2 flame with $O_2/(O_2 + N_2) = 0.1077$ and $\phi = 0.91$, both at $T_g = 318$ K. In the latter mixture, denoted by red circles,

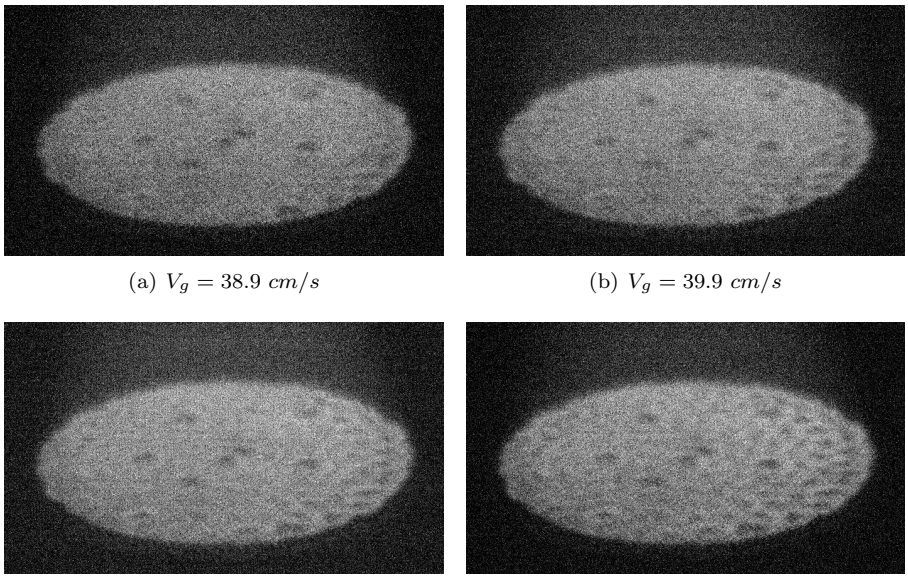

(a) $V_g = 38.9\ cm/s$ (b) $V_g = 39.9\ cm/s$

(c) $V_g^* = 41.0\ cm/s$ (d) $V_g^* = 42.0\ cm/s$

Figure 2.11: *Images of the OH* emission in the H_2 + air flames at $\phi = 0.475$ and $T_g = 318$ K for different cold gas velocities V_g. The asterisks denote velocities filtered out due to growing corrugation.*

a point at conditions very close to adiabatic is available, which is not the case for the H_2 + air flame (blue squares). No super-adiabatic points ($c_r > 0$) exist due to corrugation of the flame and subsequent decrease of the slope of the c_r dependence. Therefore, the points where the flames are not flat had to be filtered out, and based on the remaining points, S_L had to be obtained by fitting the extrapolation line. The filtering was done using the corresponding images of OH^* emission recorded with a EM-CCD camera simultaneously to the parabolic coefficient measurement. A band-pass filter was installed in order to block emission from the products. Figure 2.11 (from Paper III) gives an example of these images for the H_2 + air flame of Figure 2.10. The position of the holes blocked by the thermocouples is seen on the images as "dips" in the flame front on the radii located at 60° to each other. Generally, the instabilities start to grow at the right side of the burner Figure 2.11(c), possibly because the thermal contact between the burner plate and the burner head can not be made ideally uniform for the present burner design. At that time, most of the flame is still undisturbed, while with further increase of V_g, the corrugation spreads over the whole flame front Figure 2.11(d). In the data processing, points with small localized instabilities were considered in the measurements, since they did not affect the parabolic coefficient. The conditions with developed corrugation were filtered out. For the case of H_2 + air flame in Figures 2.10, 2.11, the points corresponding to Figures 2.11(a), 2.11(b) (V_g = 38.9 cm/s and 39.9 cm/s) were kept and higher velocities were removed (Figures 2.11(c), 2.11(d), V_g = 41 cm/s and 42 cm/s). The noticeable change of the slope of

c_r in this mixture occurs at c.a. 45 cm/s where cells start to merge with each other.

In Figure 2.10, similarly to Figure 2.7, points used for S_L determination in the H_2 + air mixture are fitted with the thick green line, which is further extrapolated to $c_r = 0$ (dash-dot green line). For H_2 + O_2 + N_2 mixture, the extrapolation back to sub-adiabatic flames is denoted with the green dot line to visualize the linearity of c_r dependence. Comparing Figure 2.7 and Figure 2.10, it can be seen that the relative parameter c_r shows a linear dependence much longer than the original $C(V_g)$.

The extrapolation was typically performed using 4 experimental points (if available), which was found to be sufficient to reduce random scatter occurred in the recorded c_r. On the other hand, in a wider range c_r start to deviate from a straight line due to a systematic non-linear behavior (see the red symbols and the dotted line in Figure 2.10), therefore, the lower velocities were also removed from the extrapolation domain.

For the H_2 + air flame in Figure 2.10, the corrugation began $\sim$ 3 cm/s before the noticeable change of the slope of $C(V_g)$. Generalizing over all H_2 + air mixtures, it occurred at velocities about 10-15% above the last value where corrugation was still localized, i.e. the last point used for S_L determination. These higher velocities of the linear part of the curve were removed at the data processing stage. Nevertheless, it does not affect significantly the slope of the extrapolation line, as evident from Figure 2.10. If these points were considered in the data processing, the corresponding S_L values would increase generally by about 2-4%.

The influence of extrapolation was estimated as the following. According to Eq. (2.35), the $C(V_g)$ in stable flat flames on a particular burner depends on the burning velocity S_L, temperature exponent α and molar heat capacity c_p^ν. Therefore, if two arbitrary mixtures have all these parameters in common, then the shape of c_r as a function of V_g can also be expected to be similar. For the case of lean H_2 + air flames, such a counterpart was found in diluted flames. The five H_2 + air mixtures measured in the present work were associated with the corresponding H_2 + O_2 + N_2 mixtures ($O_2/(O_2 + N_2) = 0.1077$), which had the same mole fraction of H_2 and c_p^ν for all pairs. Burning velocities and temperature exponents, obtained with detailed modeling, were also found to be very similar for the two sets of mixtures as presented in Paper III.

The resemblance of the counterpart mixtures in terms of shape and location of the c_r curves in V_g-c_r coordinates can be assessed from Figure 2.10. It can be seen that the slope of the two c_r dependencies is identical and the velocity range is similar. Here it has to be emphasized that the proposed method is not intended to "correct" the obtained S_L for extrapolation, the aim was to estimate the degree of introduced uncertainty.

The influence of extrapolation is illustrated in Figure 2.12 (taken from Paper III) for the two flames of Figure 2.10. The experimental c_r dependence for the diluted mixtures was used, where the real value of S_L is known. First,

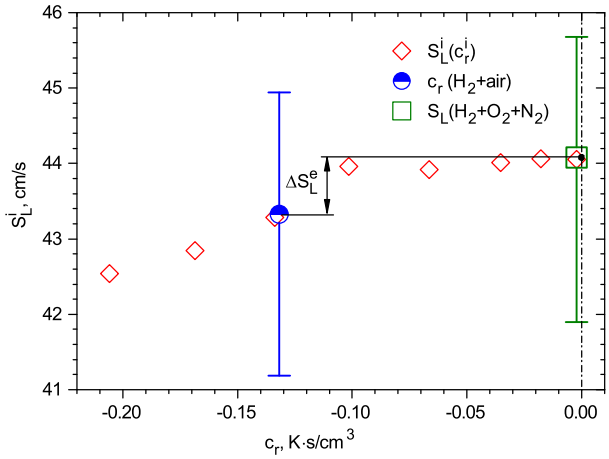

Figure 2.12: *Determination of the ΔS_L originating from extrapolation. The symbols are: $S_L^i(c_r^i)$ – red diamonds; real S_L of the H_2 + O_2 + N_2 mixture – green square; position of c_r of the H_2 + air mixture – blue circle. The error bars correspond to S_L uncertainty from TC scattering. The distance ΔS_L^e corresponds to the extrapolation uncertainty.*

the "sub-adiabatic" burning velocities of H_2 + O_2 + N_2 mixture were determined by extrapolation from sub-adiabatic data points. For each point c_r^i of the dependence in Figure 2.10, the higher values, i.e. $c_r > c_r^i$; $V_g > V_g^i$, were removed and the corresponding burning velocities were determined by extrapolation. The obtained function, $S_L^i(c_r^i)$, is shown in Figure 2.12. The real burning velocity of the H_2 + O_2 + N_2 mixture is plotted with the error bars representing uncertainty of the TC scattering. Then, the c_r value of the last available experimental point from the corresponding H_2 + air flame, c_r^{max}, is found on the obtained curve by linear interpolation. The c_r^{max} is shown in Figure 2.12 with a circle, and the error bars of the H_2 + air S_L are also given for comparison. Assuming that the shape of c_r curves in H_2 + air and H_2 + O_2 + N_2 mixtures is not significantly different, the extrapolation uncertainty in S_L can be estimated by looking at S_L^i values in the domain $c_r^{max} < c_r^i < 0$. This extrapolation uncertainty, denoted in the figures as ΔS_L^e, was estimated as the difference between the maximum and minimum observed S_L^i. For the higher unburned gas temperatures, T_g = 338 K, 358 K, where the real burning velocity in H_2 + O_2 + N_2 mixtures itself was in fact "sub-adiabatic" and found by extrapolation, an additional error, ΔS_L^{add}, was added to ΔS_L^e. These quantities were estimated based on all available S_L^i dependencies, as reported in Paper III. In the same way, the extrapolation uncertainty was estimated for the H_2 + air mixtures at 278 K, where no measurements in H_2 + O_2 + N_2 mixtures were performed due to short or zero extrapolation interval in H_2 + air mixtures.

The extrapolation in c_r coordinates underpredicts S_L for all $\alpha > 2$ as follows from Eq. (2.35), therefore, the value of ΔS_L^e should be added to the

positive side of the combined error bar from TC scattering and MFCs. The latter factors are independent and each of them is centered around the mean, they were added together in a square sum to get the approximate values of the positive and negative random components of the total error bars. Then ΔS_L^e was added to the positive side in an algebraic sum.

In liquid fuels, oscillations of the parabolic coefficient cause an increased uncertainty in S_L if it is obtained by extrapolation. Within the linearity range of the relative parabolic coefficient c_r, Eq. (2.24) can be used to estimate the associated uncertainty by replacing C by c_r, and the error increases for longer extrapolation domains. However, it has to be emphasized that Eq. (2.24) does not take into account non-linearity of the parabolic coefficient, and when it is significant, the related uncertainty has to be evaluated separately. The non-linearity also imposes constraints on the interpolation domain for S_L determination from $C(V_g)$. Generally, 4-5 points in a 2 cm/s interval are sufficient to damp any random scatter of the parabolic coefficient, while still being within the local linearity of $C(V_g)$.

The advantage of using relative c_r coordinates for extrapolation also follows from Eq. (2.35), since it can be easily shown that for any $a > 0$, a dependence of the form $x \cdot (x^a - 1)$ has a larger curvature than $(x^a - 1)$ at $x = 1$, where $x = V_g/S_L$ in the notation of Eq. (2.35). While Eq. (2.35) suggests that the parabolic coefficient is linear against $V_g \left[(V_g/S_L)^{\frac{1}{\alpha-1}} - 1\right]$, direct use of Eq. (2.35) in the data processing seems to be more problematic, since the parameters S_L and α are unknown before the measurements. However, they can be determined with an iterative algorithm as will be presented below. To show how Eq. (2.35) can linearize the parabolic coefficient, it was plotted as a function of the velocity-dependent term of Eq. (2.35) for the two diluted H_2 mixtures of Figure 2.7. The results are shown in Figure 2.13 (taken from Paper V), and a linear dependence is observed in a longer range of V_g as compared to Figures 2.7, 2.10 (i.e. for all recorded points V_g = 25-40 cm/s and V_g = 30-45 cm/s in the mixtures at 298 K and 318 K, respectively). While the slope of the line might not match exactly the constant term of Eq. (2.35), the power dependence of $C(V_g)$ is well reproduced.

Equation (2.35) can be used for S_L determination directly. Extrapolation method based on the relative parabolic coefficient c_r was described above, and it was used in Paper III to obtain S_L of lean H_2 + air flames. However, to completely eliminate the extrapolation uncertainty, $C(V_g)$ dependencies of mixtures at different unburned gas temperatures can be processed simultaneously to determine S_L and α using Eq. (2.35) in an iterative procedure. Another advantage is that no additional measurements (for the present study, in H_2 + O_2 + N_2 mixtures) are required. For a specific H_2 + air mixture studied in Paper III (defined by ϕ), there were 5 datasets recorded at T_g = 278, 298, 318, 338 and 358 K. S_L and α determined with the c_r method were used as the initial guess to calculate the velocity-dependent term of Eq. (2.35) for each mixture. Then, linear regressions in the form shown in Figure 2.13 were used to determine S_L and α for the next iteration. S_L are obtained by

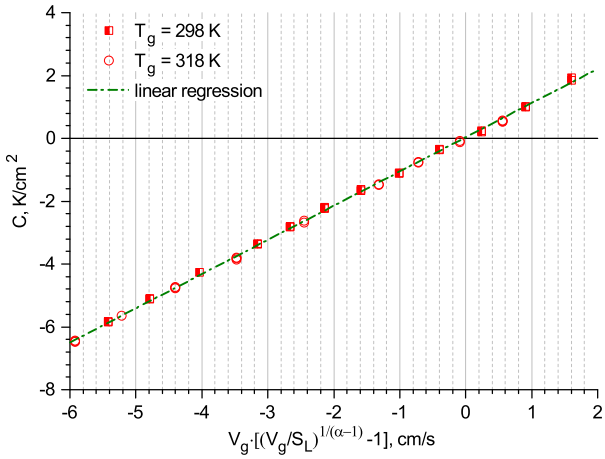

Figure 2.13: *Linearized parabolic coefficient dependence based on Eq. (2.35) for two H_2 + O_2 + N_2 mixtures with ϕ = 0.91 and $O_2/(O_2+N_2)$ = 10.77%.*

calculating V_g in the crossing point of the regression line and $C = 0$ (see Figure 2.13). After a few iterations, the distance between the crossing point and the origin reduces by several orders of magnitude for each T_g, meaning that the $C(V_g)$ dependencies were successfully linearized. To estimate the uncertainty in S_L, the uncertainties in the parabolic coefficients due to scatter in the TCs and in the gas velocities due to MFCs for each of the $C(V_g)$ dependencies were treated as independent factors. One of the $C(V_g)$ was modified by setting $C = C_0 \pm \Delta C$ or $V_g = V_g^0 \pm \Delta V_g$, where C_0 and V_g^0 are the nominal values and ΔC and ΔV_g are the corresponding uncertainties. Then the iterative algorithm was run to estimate the influence of each of the uncertainty factors on S_L and α. In such formulation, the uncertainty in S_L at each T_g depends on ΔC and ΔV_g of the other datasets (at different T_g), since they affect α. The uncertainties in S_L from ΔC are asymmetric, therefore, all individual errors were sorted based on their sign and the total positive and negative error bars of S_L and α were obtained independently in a square sum of the individual positive and negative components. The obtained values of S_L and α, as well as their uncertainty ranges, were found to be close to those published in Paper III, as will be shown in Section 3.2.

Radial asymmetry, No. 22

One of the main assumptions of the heat flux method is the rotational symmetry of the heat transfer processes in the burner plate, which allows Eq. (2.14). The heat transfer is expected to be symmetric if a perfect thermal contact between the burner plate and the heating jacket is obtained. However, for the burner design developed in Eindhoven, the burner plate is attached to the burner head with a thermal paste, which in some cases was found to introduce tangential asymmetry into the temperature profiles.

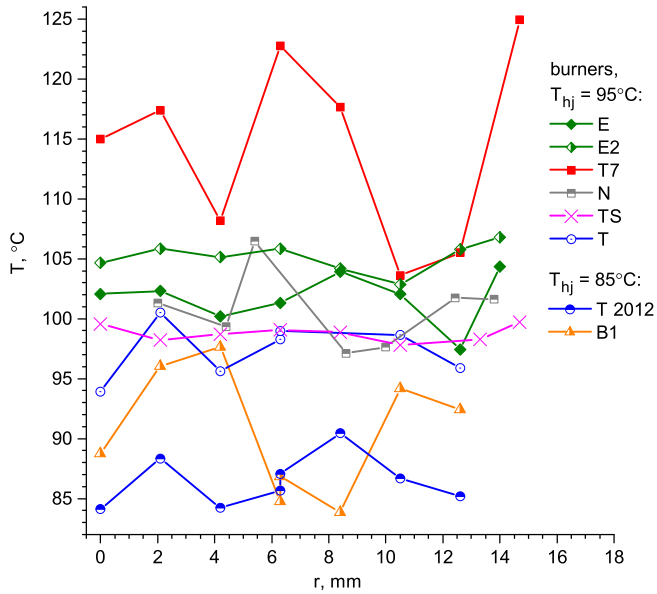

Figure 2.14: *Temperature distribution in Lund burners for the adiabatic case (temperature of the heating jacket T_{hj} is given for each profile).*

Bosschaart [65] observed radial temperature gradients in the burner plate in no-flow situations, and they occurred at the direction of the water flow in the heating jacket. In the present work, only flame conditions were analyzed. However, the asymmetry showed no correlation with the direction of the water flow.

The tangential temperature distribution in the heat flux burner can be investigated with, e.g., 2D temperature mapping employing thermographic phosphors [95] or infrared thermometry [65]. The presence of the asymmetry can also be determined by using only available TC readings. Figure 2.14 from Paper V shows the temperature profiles recorded at the adiabatic conditions

Table 2.4: *Characteristics of the Lund burners.*

burner	TC type	hole ID and pitch, mm	TC shielded	burner plate design
T/T2012	T	0.5x0.7	no	TU/e
T7	T	0.5x0.7	no	TU/e
B1	T	0.5x0.7	no	TU/e
E	E	0.5x0.7	yes	TU/e
E2	E	0.5x0.7	yes	TU/e
N	N	0.3x0.4	yes	TU/e
TS	T	0.5x0.7	no	Zhejiang

on burners used in Lund. The characteristics of the burners are given in Table 2.4. Burner "T" is the same burner as "T 2012" but with one non-operational thermocouple. One of the burners was repaired several times, and denoted in Table 2.4 as "T7", "B1", "E" and "E2". Each time the burner plate was reattached and TCs were changed, except for the burner "E2", when the TCs from burner "E" were reattached. Burner "TS" was designed by Zhejiang University and has a burner plate integrated with the heating jacket, and a teflon burner head as presented in, e.g., [86]. Temperature profiles for all burners were recorded at the heating jacket temperature of 95° C, except for burners "B1" and "T2012", for which it was equal to 85° C. For all profiles, the parabolic coefficient C obtained by linear regression of Eq. (2.14) is close enough to zero to consider the flame to be adiabatic. The profiles for all burners possess some scatter which can be attributed to: the instrumental error of the TCs, the axial position of the thermocouple in the burner plate, the heat contact between the thermocouple and the burner plate, conduction by the TC wire. Still, a contribution to the scatter that comes from the possible tangential asymmetry can be determined. Since each thermocouple is positioned in the burner plate at a specific radius r and polar angle, the thermocouple readings can be projected to a direction x at some polar angle α as shown in Figure 2.15 (taken from Paper V). Then the obtained profiles are fitted with linear regression and R^2 statistics is calculated. By varying the polar angle, a direction with the maximum R^2 can be found, i.e., the direction in which the asymmetric heat transfer occurs. Figure 2.16 from Paper V presents the temperature profiles for different burners in the direction with the maximum R^2.

Also given in Figure 2.16 are the significance levels p for maximum R^2 coefficients, which were estimated using the following method. Assuming that the temperature distribution of Figure 2.14 is caused by factors independent of the thermocouple location in the burner plate, this distribution can be

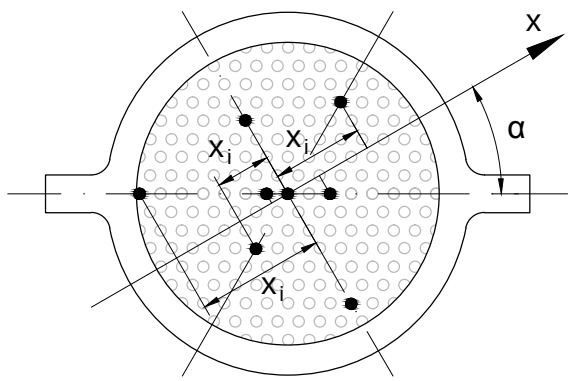

Figure 2.15: *Projections of the thermocouple readings to the direction x.*

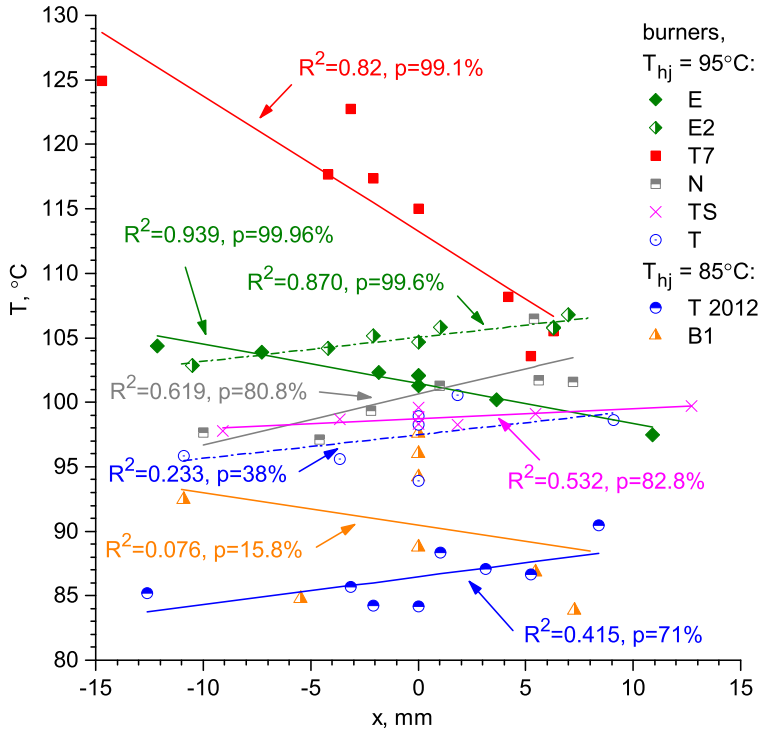

Figure 2.16: *Temperature distribution in the Lund burners for the direction (polar angle) with maximum R^2 coefficient (temperature of the heating jacket T_{hj} is given for each profile). The values of R^2 and corresponding confidence levels p for each burner are also shown.*

simulated by a random temperature scatter in the range of observed maximum temperature difference for each burner. This random scatter also has to be constrained by the parabolic coefficient $C \approx 0$, therefore, randomly generated profiles were later filtered to contain only those representing conditions close to adiabatic. Then the same procedure of finding the maximum R^2 is applied for the random profiles. The probability distribution of the maximum R^2 is obtained and the real value of R^2 (presented in Figure 2.16) is used to determine the confidence level p. These probability distributions were found to be slightly different for each burner, since the patterns of thermocouple placement are different. Practically, R^2 and p indicate to what extent the scatter in TC readings can be explained by the asymmetric heat fluxes, and they are independent of the absolute temperature difference itself: $R^2 \to 1$, $p \to 1$ if all scatter occurs due to asymmetry; $R^2 \to 0$, $p \to 0$ if it is caused by other reasons, not related to the radial and angular position of the TCs in the burner: instrument error, axial position of the TCs, heat contact between the TCs and the burner plate etc.

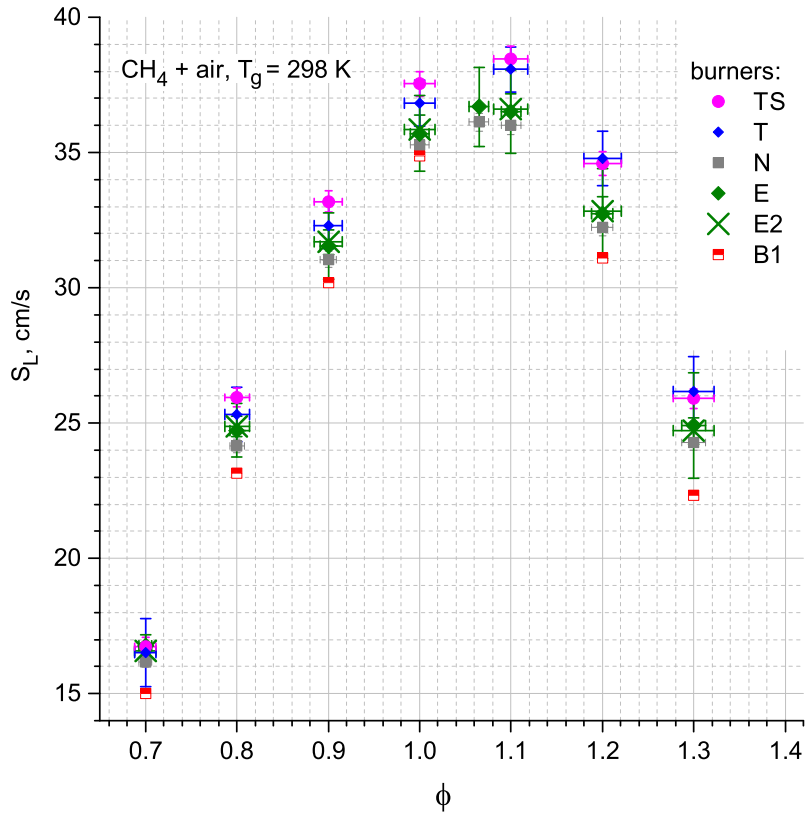

Figure 2.17: *CH_4 + air burning velocity measured with different burners in Lund. The values are corrected for the surface area A.*

The data in Figure 2.16 indicate that there is a correlation between the asymmetry (radial temperature gradient) and the average temperature, which at the adiabatic conditions should be equal to the heating jacket temperature of 95° C (85° C for burners "T2012" and "B1"). The largest gradients are observed for burner "T7", used in the measurements of [96–100]. In [96], the observed big scatter in TC profiles of burner "T7" was explained by anomalous behavior of the last thermocouple (located at 14.7 mm in Figure 2.14 and at −14.7 mm in Figure 2.16), whose readings were filtered out in the data processing. The results of Figure 2.16 clearly indicate that readings from this TC are in line with the others, and that data measured on burner "T7" are affected by the asymmetry. Moreover, significant difference between the average burner plate temperature and the temperature of the heating jacket is an indication of anomaly in the heat fluxes, and such burners should not be used.

Other burners can be compared in terms of S_L of CH_4 + air flames, and the results are shown in Figure 2.17 (taken from Paper V). The data were corrected

using the surface area of perforation for burners "N", "T" and "TS". The two burners with lower asymmetry and average temperature close to 95° C, "T" and "TS", show close results, higher than burners "N", "E" and "E2". The latter three burners have higher asymmetry and higher average temperature as seen from Figure 2.16. High error bars for burner "E" are due to increased, for unclear reason, temperature scatter, which occurred sometime after the results of [101] were obtained. The data from [101] were used to represent burner "E" in Figures 2.14, 2.16.

Figure 2.17 includes results measured on burner "B1" as well. The TC profiles showed no clear asymmetric behavior, as seen from Figure 2.16. However, the scatter itself was rather big (around 10-15 K at adiabatic conditions – see Figures 2.14, 2.16), and burning velocities of CH_4 + air flames were found to be the lowest among all burners, though comparable to the data from burners "T" and "N" before the surface area correction.

Burner "TS" with improved design of the burner plate showed the best performance in terms of the temperature scatter (see Figures 2.14, 2.16), and these results suggest that the reason for asymmetry in the other burners is the thermal contact between the burner plate and the burner head. Traditional design of the Eindhoven burners employs thermal paste (Electrolube EHTSP50T) for mounting the plate and providing heat transfer to/from the water jacket. It is believed that asymmetry might be introduced during the mounting of the burner plate (e.g., by having non-uniform layer of the paste).

2.1.4 Extraction of the temperature dependence of S_L

Generally, temperature dependence of the laminar burning velocity for different mixtures is presented in literature in two ways: in the form of Eq. (1.1), i.e., determining the power exponent α, or as plots of S_L at different unburned gas temperatures T_g. The use of α seems to be more practical, since it allows comparison of data obtained at different T_g. In the present work, α was determined from the experimental results of Section 3.2.2, from available literature data ($S_L(T_g)$) and from kinetic modeling.

To obtain α, $S_L(T_g)$ is fitted by linear regression in logarithmic coordinates (see Eq. (1.1)). If several burning velocities $S_L^{T_i}$ at temperatures T_i are known, then:

$$\alpha = \frac{\sum_i \ln S_L^{T_i} \ln \frac{T_i}{T_0} - \frac{1}{n} \sum_i \ln \frac{T_i}{T_0} \sum_i \ln S_L^{T_i}}{\sum_i \ln^2 \frac{T_i}{T_0} - \frac{1}{n} \left(\sum_i \ln \frac{T_i}{T_0} \right)^2} \tag{2.37}$$

It is also essential to estimate the accuracy of α, which can possess rather high uncertainty, especially for smaller temperature ranges. Using the error propagation rule on Eq. (2.37) and having $\Delta S_L^{T_i}$ as the errors of individual

$S_L^{T_i}$, the uncertainty in α becomes:

$$\Delta\alpha = \frac{\left(\sum_i \left[\left(\ln \frac{T_i}{T_0} - \overline{\ln \frac{T_i}{T_0}} \right) \cdot \frac{\Delta S_L^{T_i}}{S_L^{T_i}} \right]^2 \right)^{0.5}}{\sum_i \ln^2 \frac{T_i}{T_0} - n \cdot \left(\overline{\ln \frac{T_i}{T_0}} \right)^2} \tag{2.38}$$

where n is the number of data points, T_0 is the reference temperature in Eq. (1.1) and the mean logarithmic normalized temperature is equal to:

$$\overline{\ln \frac{T_i}{T_0}} = \frac{\sum_i \ln \frac{T_i}{T_0}}{n} \tag{2.39}$$

Eq. (2.38) can be used for estimation of error in α, if the regression line of Eq. (1.1) lies within $S_L^{T_i} \pm \Delta S_L^{T_i}$. However, for cases with asymmetric errors, i.e., when S_L is obtained with the heat flux method from the relative c_r dependency (Figure 2.10), Eq. (2.38) does not strictly hold. An approximate uncertainty range of α can be determined as following. First, the random components of the positive and negative errors in $S_L^{T_i}$, $\Delta S_L^{T_i+}$ and $\Delta S_L^{T_i-}$, respectively, should be regrouped based on whether they increase or decrease α, and that is determined by the sign of the difference $\ln \frac{T_i}{T_0} - \overline{\ln \frac{T_i}{T_0}}$. Then, Eq. (2.38) is applied to determine the positive and negative sides of the error bar of α. Finally, a quantity $\Delta\alpha^e = \alpha(S_L^{T_i} + (\Delta S_L^e)^{T_i})) - \alpha(S_L^{T_i})$, which represents the systematic term due to S_L extrapolation, is added to one of the sides of the error bar, depending on the sign of $\Delta\alpha^e$. For lean H_2 + air flames discussed in Section 3.2.2, all ΔS_L^e are positive, increasing at larger T_i, therefore, $\Delta\alpha^e$ contributes to the positive side of the error bar. The uncertainty estimation for α obtained with the iterative algorithm was described in Section 2.1.3.3.

2.2 Flame structure

2.2.1 Flat flame burner

In the studies of flame structure, a commercially available McKenna burner was used, its cross section is shown in Figure 2.18. The McKenna burner has a 1 cm thick sintered burner plug with a brass coil inside it. A flow of water in the coil takes the heat from the flame and prevents the burner plug from overheating. A separate chamber around the plenum chamber with another sintered plug serves to produce a co-flow around the flame, which isolates it from the ambient atmosphere. A stabilizer can be installed above the burner (typically, at 1-2 cm) that acts as the stagnation plane. The burner can be placed in a low pressure chamber to study flame structure at pressures below atmospheric.

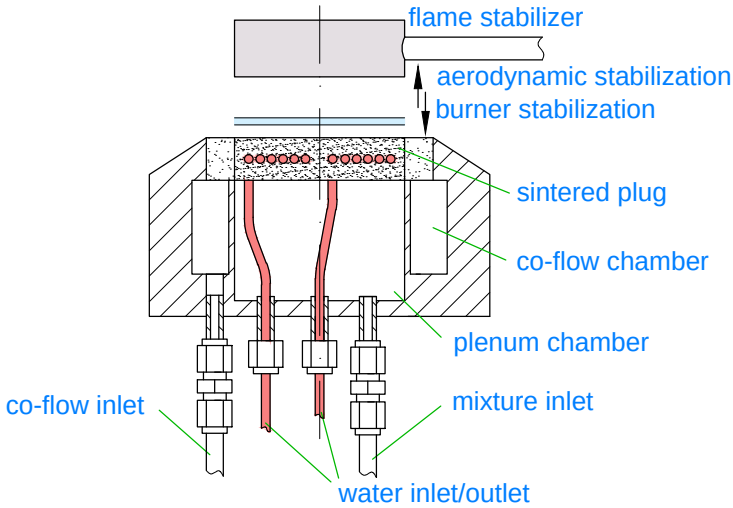

Figure 2.18: *Flat-flame burner for flame structure studies*

Two flame regimes can be produced with the flat-flame burner. First, the unburned gas velocity is set lower than laminar burning velocity, $V_g < S_L$, and the stabilizer is not installed. The flame is attached to the burner and stabilized due to conductive heat loss to the burner plug. The heat is removed from the system by the water circuit. Flame geometry is one-dimensional. If $V_g > S_L$ and the stabilizer is installed, then it acts as the stagnation plane. Flame is lifted above the burner surface and stabilized due to aerodynamic strain (see also Section 2.1.1). The latter regime can be favorable for flame structure studies, since the whole flame front can be resolved with laser diagnostics methods and since no chemical reactions occur at and below the burner surface. However, due to asymmetry in the flow and heat transfer, existing in a practical experimental setup, the flame might lose homogeneity. Also, aerodynamically stabilized flames are much more sensitive to external flow disturbances. In Figure 2.18, the two flame regimes are denoted schematically by arrows: an increase of the inlet flow moves the flame away from the burner, and a decrease of the flow results in a burner-stabilized flame.

In most studies, the flames are burner-stabilized. It was shown by Olofsson et al. [102] that the radial temperature distribution in such flames is homogeneous, as was evident from CARS measurements at 1 cm above the burner in atmospheric-pressure C_2H_4 + air flames. On the other hand, some differences were found in terms of the soot volume fraction, the same was observed in [103]. Bachmann et al. [104] reported highly inhomogeneous PAH profiles in a low-pressure benzene + air flame, obtained with mass spectrometry.

Flames stabilized by strain can possess larger asymmetry. As an example, Figure 2.19 from Paper IV shows the distribution of NH in three NH_3 + air flames, which indicates that the flames are not flat. While it indicates that any line-of-sight measurements in such flames are not possible, spatially

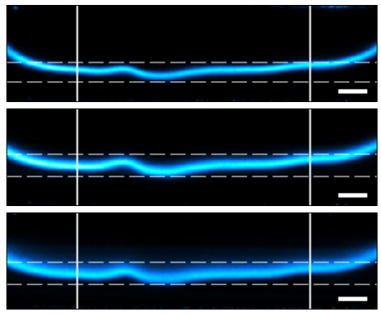

Figure 2.19: *NH images in three NH_3 + air flames: ϕ = 0.9 (top), ϕ = 1.0 (middle), ϕ = 1.2 (bottom).*

resolved techniques can still be applied, since the absolute species concentrations showed no dependence on the local flame curvature, as was concluded from the results presented in Paper IV. Also, the description of the procedure for determination of the radical species (with LIF) and temperature (with CARS) can be found there, since it is outside the scope of the present thesis.

2.2.2 Intracavity absorption spectroscopy

Despite the development of spatially resolved techniques for studying flame structure, the "line-of-sight" methods still remain important for laminar flames due to simplicity of quantification of the measured spectroscopic data. Absorption spectroscopy is one of these methods. The issue of the line-of-sight measurement is not critical for flame conditions relevant for kinetic studies, since the modeling is also performed in one dimension. The applicability of the experimental data for kinetic model validation requires a flat flame, where temperature and species concentrations are dependent only on the axial coordinate. Therefore, under such conditions, there is no need for spatially resolved signals along the radial coordinate, and absorption techniques would become a good choice, which may provide information about species concentrations and temperature in the same measurement. In flame diagnostics, the three following techniques are commonly used: Cavity Ring-down (CRDS), Cavity Enhanced (CEAS) or Intracavity Laser Absorption Spectroscopy (ICLAS). Having a comparable spectral sensitivity, these methods have different advantages and their selection can vary depending on the researcher's convenience. For example, CRDS and CEAS utilize a simple detection equipment, but require a high-finesse cavity [105]. In ICLAS, the cavity loss can be as high as 50%. The whole spectrum can be obtained in one shot, and it gives the most easily interpretable spectral data for narrow weak absorption lines [106].

ICLAS has been discussed in detail by Baev et al. [106]. The method originates from the study of Pakhomycheva et al. [107]. The absorbing medium is placed inside the laser cavity, forcing the laser light to pass this medium many times. The laser gain compensates broadband cavity losses, e.g. mirror

transmission, resulting in a very high spectral sensitivity [106]. If a multi-mode laser and absorbing medium with narrow-band absorption lines are considered, then the number of photons in mode q can be expressed as [106]:

$$M_q(t) = M^s \frac{\sqrt{\gamma t/\pi}}{Q} \exp\left[-\left(\frac{q-q_0}{Q}\right)^2 \gamma t\right] \exp\left(-n\sigma(\nu)\frac{l}{L}ct\right) \tag{2.40}$$

where M_q is a function of time, γ is the broadband cavity loss, q_0 is the central mode, Q is HWHM of the maximum gain at the central mode, M^s is the total number of photons, n is the absorber density, $\sigma(\nu)$ is the absorption cross section at wavelength ν, l and L are the lengths of the absorber and cavity, respectively, and c is the speed of light. In Eq. (2.40), M^s is a constant value. It can be seen that Eq. (2.40) is equivalent to the Beer-Lambert law:

$$I(\nu) = I_0(\nu)\exp(-n\sigma(\nu)L) \tag{2.41}$$

where $I(\nu)$ and $I_0(\nu)$ are the transmitted and incident light intensities at wavelength (ν), L is the length of the absorber. Therefore, in ICLAS, the effective absorption path length is defined as:

$$L_{eff} = \frac{l}{L}ct \tag{2.42}$$

Equation (2.40) holds until $t = t_s$, where t_s is the spectral saturation time, i.e., the time when the emission in the central mode becomes stationary. Thus, the fundamental limit of the spectral sensitivity of ICLAS is determined as $L_{eff} = ct_s$. The saturation time t_s can take values around 10^{-2}-10^2 ms for different types of lasers as summarized in [106]. As t_s is the highest for dye lasers, the values of L_{eff} as high as 70000 km can be achieved [108]. In practical measurements, however, t has to be selected less than t_s.

The ICLAS setup in Tel Aviv, first used in [109], is shown in Figure 2.20(a) (adapted from Paper VI). The setup is an external-cavity dye laser built around a low-pressure chamber. A jet of Kiton-620 dye is pumped by a cw Nd-YAG laser at 532 nm. Spherical mirror M1 is used to focus the pump beam, spherical mirror M2 is the high reflector of the laser cavity, and spherical mirror M3 is used to direct the beam through the low-pressure chamber. The three mirrors have high reflectivity. The output coupler (OM) is a planar mirror. The chamber has two mirrors W1 and W2, wedged to avoid the interference fringes. The central wavelength of the dye laser is tuned with a pellicle beam splitter (BS). The transmitted laser beam is recorded with a 1D CCD array installed in a spectrograph.

Two acousto-optic modulators (AOM) are installed in the optical path. The first AOM chops the pump beam and produces a sequence of pulses of duration t_g. The second AOM selects the last portion of the transmitted beam, corresponding to the laser generation time $t = t_g$, which is used to calculate L_{eff} (Eq. (2.42)).

Instead of a dye laser, an optical fiber doped with a rare earth metal can be used as the lasing medium. The technique is called Fiber Laser Intracavity

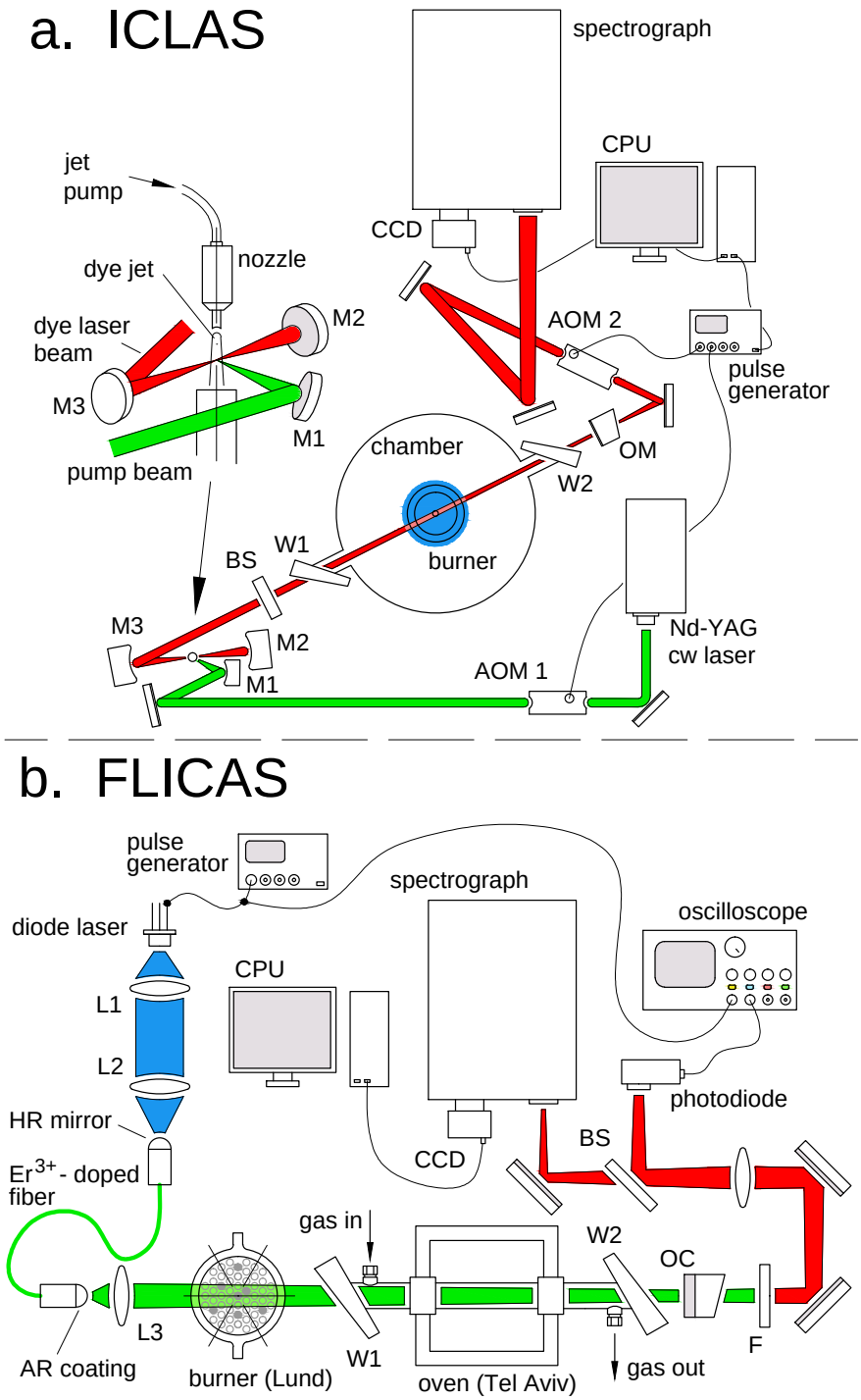

Figure 2.20: *Intracavity absorption setups: ICLAS setup in Tel Aviv (a) and FLICAS setups in Tel Aviv and Lund (b).*

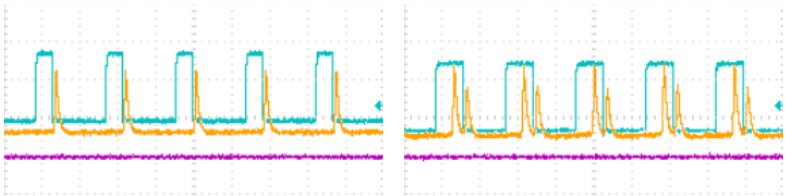

(a) (b)

Figure 2.21: *FLICAS oscillograms showing pump pulses (cyan) and relaxation peaks (yellow): single (a) and double (b).*

Absorption Spectroscopy (FLICAS). Its main advantage is a low cost of the laser fibers and pump sources. Two FLICAS setups built in Tel Aviv and Lund, similar to [110], are shown in Figure 2.20(b) (from Paper VII). A diode laser is used to pump the Er^{3+} fiber at 980 nm. One end of the fiber is a high reflectivity mirror at the laser wavelength (∼1500 nm), which transmits the pump wavelength. The second end of the fiber has an anti-reflective coating (AR), and spherical lens L3 focuses the pump beam on the output mirror OC. The central mode of the generation beam can be selected by moving lens L3, utilizing the effect of chromatic aberrations. A long pass filter (F) blocks the pump wavelength, and the transmitted signal is collected at the spectrograph. The absorbing medium can be an atmospheric-pressure flame (in Lund) or a cell in the oven (in Tel Aviv).

Opposed to ICLAS with the dye laser, the fiber laser generates one or several relaxation oscillations [111]. The number of the relaxation peaks depends on the intensity and duration of the pump pulse. These parameters should be selected to produce only one relaxation peak. The relaxation peaks can be viewed on an oscilloscope using a beam splitter (BS) and a photodiode, together with the pump pulses. The appearance of the maximum peak intensity determines the generation time t in Eq. (2.42). To estimate this time, the duration of the pump pulse is increased until the second peak appears, and about a half of the interval between the peaks corresponds to the time t. An example of such oscillograms with single and double relaxation peaks is shown in Figure 2.21.

The exposure time of the CCD array in ICLAS or FLICAS setups can be set to collect several generation pulses in a single shot, and then the single shots are further averaged on a computer. Prior to the measurements, the spectral range and instrument function of the FLICAS spectrometer was calibrated by recording the absorption of CO_2 in an open T-shape tube at room temperature.

2.3 Modeling

For detailed modeling, a commercially available software package, CHEMKIN IV [112], was used. It provides the reactor models for the simulation of various

0D and 1D combustion environments. The following section describes the basic modeling approach and mathematical description of the combustion systems studied in Papers I-VII.

2.3.1 Reaction rate formulation

A detailed reaction mechanism consists of a number of reactions. Primarily, the reactions are elementary, i.e., they proceed as stated by the reaction equation through collisions between the reactant species. Consider a typical bimolecular reaction:

$$CH_3 + O = CH_2O + H \tag{R2.1}$$

Its rate in the forward direction depends on the concentrations of the initial reactants, $[CH_3]$ and $[O]$, and the rate constant k_+:

$$r_+ = k_+ \cdot [CH_3][O] \tag{2.43}$$

The rate constant is expressed in the so-called modified Arrhenius form:

$$k_+ = AT^n \cdot exp\left(-\frac{E_a}{RT}\right) \tag{2.44}$$

where A is the pre-exponential factor, n is the temperature exponent, E_a is the activation energy and R is the gas constant. Most often, the elementary reactions in the CHEMKIN input files are specified to be reversible, with the rate constant of the backward reaction k_-:

$$k_- = \frac{k_+}{K} \tag{2.45}$$

where K is the equilibrium constant of the reaction, calculated using the thermodynamic data of the participating species.

Some reactions require a collision with a third body species, for example:

$$H + O_2 \ (+M) = HO_2 \ (+M) \tag{R2.2}$$

Here "M" denotes any species. Some third bodies can be more efficient collisional partners than others, then the pre-exponential factor is modified with the collisional efficiency a. For reaction (R2.2), the forward rate becomes equal to [116]:

$$r_{0+} = \left(\sum_i a_i[X_i]\right) k_{0+} \cdot [H][O_2] \tag{2.46}$$

where index "i" applies to all species. Thus, when all $a_i = 1$, $\left(\sum_i a_i[X_i]\right) = [M]$:

$$r_{0+} = k_{0+} \cdot [H][O_2][M] \tag{2.47}$$

In reaction (R2.2), the third body species M is written in parenthesis, which denotes a pressure-dependent reaction. Lindemann [113] described such reactions as two-step:

$$\mathrm{H} + \mathrm{O_2} = \mathrm{HO_2}^* \tag{R2.3}$$

$$\mathrm{HO_2}^* + \mathrm{M} = \mathrm{HO_2} + \mathrm{M} \tag{R2.4}$$

where at first, (R2.3), the activated complex is formed, and then it is deactivated by a collision with M (R2.4). At low pressures, the rate determining step is (R2.4) [114], and the resulting rate constant is proportional to [M], Eq. (2.47), which is the low-pressure limit of reaction (R2.2). At high pressure, [M]$\rightarrow \infty$, so that the collisional deactivation (R2.4) is much faster than the formation of the activated complex (R2.3) [114]. The collisions are at equilibrium, and the reaction rate becomes independent of [M]:

$$r_\infty = k_\infty \cdot [\mathrm{H}][\mathrm{O_2}] \tag{2.48}$$

In the CHEMKIN input files, pressure-dependent reactions are defined by their low- and high-pressure rate constants, and by a function which describes the behavior at intermediate pressures, in the so-called "fall-off" region. The rate constant of pressure-dependent reactions is obtained via:

$$k = \frac{k_\infty k_0[\mathrm{M}]}{k_0[\mathrm{M}] + k_\infty} F \tag{2.49}$$

where F represents a functional dependence. In the commonly used Troe form [115], F is a function of four constants, temperature and the reduced pressure $P_r = k_0[\mathrm{M}]/k_\infty$.

Any reaction can be represented as:

$$\sum_{i=1}^{n_{reac}} \nu_i R_i = \sum_{j=1}^{n_{prod}} \nu_j P_j \tag{2.50}$$

where n_{reac} and n_{prod} are the number of reactants and products, ν_i and ν_j are the stoichiometric coefficients of i-th reactant R_i and j-th product P_j, respectively. The total rate, accounting for the forward and backward reactions, becomes:

$$r = k_+ \sum_{j=1}^{n_{prod}} [\mathrm{P}_j]^{\nu_j} - k_- \sum_{i=1}^{n_{reac}} [\mathrm{R}_i]^{\nu_i} \tag{2.51}$$

The reaction equation Eq. (2.50) can be written in a generic form:

$$\sum_{i=1}^{n} \nu_i Z_i = 0 \tag{2.52}$$

where n is the total number of species (Z_i) in the system, $\nu_i > 0$ for products, $\nu_i < 0$ for reactants and $\nu_i = 0$ for non-participating species and third bodies. Finally, if chemical mechanism contains K reactions, the molar production of species "i" becomes:

$$\dot{\omega}_i = \frac{d[\mathrm{Z}_i]}{dt} = \sum_{k=1}^{K} \nu_{i,k} r_k \tag{2.53}$$

where $\nu_{i,k}$ is the stoichiometric coefficient for species "i" in reaction "k" from Eq. (2.52), r_k is the rate of k-th reaction Eq. (2.51). $\dot{\omega}_i$ is expressed in mol/(s·m^3).

2.3.2 0D reactor systems

Zero-dimensional reactor models, or homogeneous batch reactors, are widely used for modeling ignition and conversion of species in flow reactors. The mathematical description of a batch reactor is simple, since there is no spatial coordinate, and all variables depend only on time. The system of equations for batch reactors [116] contains the species conservation:

$$\frac{dY_i}{dt} = \frac{\dot{\omega}_i W_i}{\rho} \tag{2.54}$$

where Y_i is the mass fraction of species "i", W_i is its molar mass, $\dot{\omega}_i$ is calculated by Eq. (2.53), and the density ρ:

$$\rho = \frac{m}{V} \tag{2.55}$$

Here m is the total mass and V is the reactor volume. The system is closed by the energy balance, which determines the temperature. The energy balance is written differently for the constant-pressure and constant-volume reactors. An example of the former is a flow reactor, and the latter formulation is typically used for simulating ignition in a shock tube. For the constant-pressure systems, the energy balance reads:

$$\rho c_p \frac{dT}{dt} + \sum_{i=1}^{n} h_i \cdot \dot{\omega}_i \cdot W_i = 0 \tag{2.56}$$

where h_i is the specific enthalpy (J/kg), and c_p is the constant-pressure heat capacity of the system, calculated using the heat capacities of its components $c_{p,i}$:

$$c_p = \sum_{i=1}^{n} Y_i c_{p,i} \tag{2.57}$$

To calculate the changing volume, the ideal gas law is used:

$$pV = \frac{m}{\overline{W}} RT \tag{2.58}$$

where $\overline{W}$ is the molar mass of the system.

For the constant-volume systems:

$$\rho c_v \frac{dT}{dt} + \sum_{i=1}^{n} \left(h_i - \frac{RT}{W_i} \right) \cdot \dot{\omega}_i \cdot W_i = 0 \tag{2.59}$$

and the constant-volume heat capacity of the mixture c_v is obtained from c_{v_i} similar to Eq. (2.57).

Due to very different timescales of the reactions, the equation system is stiff, and should be solved by an implicit algorithm. In CHEMKIN, backwards-differencing method is used [117]. The solver allows specification of the maximal timestep, and its decrease is necessary in some cases in order to obtain smooth ignition delay dependencies from several runs at different conditions. The ignition delays, reported in Section 3.1, were calculated using the

CHEMKIN solutions by applying different ignition criteria with the aim to reproduce those used in the corresponding experiments. For simulation of Rapid Compression Machines (RCM) and facility-affected processes in shock tubes, experimental pressure or volume histories were implemented. For the flow reactors, where the starting time is undefined, the modeling profiles were shifted typically to the position where the mole fraction of fuel in the experiments equals 50% of its inlet value.

2.3.3 1D reactor systems

The one-dimensional steady-state laminar flame model allows simulation of free-propagating, burner-stabilized and stagnation flames. For the former two cases, where the flow is purely one-dimensional, the governing system of equations consists of the mass and species conservation, the energy balance and the equation of state [117]. All variables are functions of the spatial coordinate x only, i.e., the system is steady-state. In 1D flames, the mass flow through the surface is constant:

$$\dot{m} = \rho u A \tag{2.60}$$

where u is the bulk velocity and A is the surface. The species conservation:

$$\dot{m}\frac{dY_i}{dx} + \frac{d}{dx}(\rho A Y_i V_i) - A\dot{\omega}_i W_i = 0 \tag{2.61}$$

includes the diffusion term, where V_i is the diffusion velocity of species "i". The energy balance:

$$\dot{m}\frac{dT}{dx} - \frac{1}{c_p}\frac{d}{dx}\left(\lambda A\frac{dT}{dx}\right) + \frac{A}{c_p}\sum_{i=1}^{n}\rho Y_i V_i c_{p,i}\frac{dT}{dx} + \frac{A}{c_p}\sum_{i=1}^{n}\dot{\omega}_i h_i W_i = 0 \tag{2.62}$$

includes the conductive, diffusive and chemical terms, where λ is the thermal conductivity of the mixture. Finally, the equation of state is the ideal gas law Eq. (2.58).

Calculation of the diffusion velocities V_i can be done using two approaches [117]. In the *multicomponent* formulation, the diffusion velocities are defined as:

$$V_i = \frac{1}{X_i\overline{W}}\sum_{j\neq i}^{n} W_j D_{i,j} d_j - \frac{D_i^T}{\rho Y_i}\frac{1}{T}\nabla T \tag{2.63}$$

$$d_i = \nabla X_i + (X_i - Y_i)\frac{1}{p}\nabla p \tag{2.64}$$

In Eqs. (2.63, 2.64), X_i is the mole fraction of species "i", $D_{i,j}$ is the multicomponent diffusion coefficient between species "i" and "j", D_i^T is the thermal diffusion coefficient of species "i".

In the *mixture-averaged* formulation, V_i are obtained from:

$$V_i = -\frac{1}{X_i}D_i^m d_i - \frac{D_i^m \Theta_i}{X_i}\frac{1}{T}\frac{dT}{dx} + V_c \tag{2.65}$$

where D_i^m are the *mixture* diffusion coefficients for species "i", Θ_i is the thermal diffusion ratio of species "i" and V_c is the correction velocity. D_i^m are calculated as:

$$D_i^m = \frac{1 - Y_i}{\sum\limits_{j \neq i}^{n} \frac{X_j}{\mathcal{D}_{ij}}} \tag{2.66}$$

and $\mathcal{D}_{ij}$ is the binary diffusion coefficient between species "i" and "j". The correction velocity V_c is required in the mixture-averaged formulation to set the net diffusive flux to zero:

$$\sum_i Y_i V_i = 0 \tag{2.67}$$

Evaluation of the multicomponent diffusion coefficients $D_{i,j}$ is computationally demanding, and the diffusion velocities V_i in the multicomponent formulation depend on concentration gradients of all species, whereas in the mixture-averaged formulation they depend only on the species' own gradients [117]. The thermal diffusion component can also be switched off in the CHEMKIN simulations. However, for light fuels such as H_2, the use of both thermal diffusion and the multicomponent formulation is necessary.

Solution of the system, Eqs. (2.60-2.62) and Eq. (2.58), is obtained after discretization of the spatial domain and solving the system of algebraic equations using the damped modified Newton algorithm [117]. The first solution is obtained on a rough grid, which is continuously refined until the desired solution is reached. A grid-independent solution implies at least 300-500 grid points. In CHEMKIN, the desired number of grid points cannot be specified directly, instead, the quality of the solution is controlled by the allowed difference in parameters between the neighboring grid points [117]:

$$|\phi_{n,j} - \phi_{n,j-1}| \leq \delta[max(\phi_n) - min(\phi_n)] \tag{2.68}$$

$$\left| \left(\frac{d\phi_n}{dx} \right)_j - \left(\frac{d\phi_n}{dx} \right)_{j-1} \right| \leq \gamma \left[max \left(\frac{d\phi_n}{dx} \right) - min \left(\frac{d\phi_n}{dx} \right) \right] \tag{2.69}$$

where ϕ is any solution variable, index "j" corresponds to the grid point, "n" to the variable number, and the quantities δ and γ are user-specified numbers, called GRAD and CURV in the CHEMKIN notation. In this formulation, Eqs. (2.68, 2.69), GRAD constrains the absolute difference of the variables in the neighboring points, and CURV - the difference in their first derivatives. To achieve a grid-independent solution, GRAD is selected to be about 0.005-0.02. Constraining CURV is optional, since the difference of the first derivatives typically decreases together with the decrease of $|\phi_{n,j} - \phi_{n,j-1}|$.

In the simulation of burner-stabilized flames, the CHEMKIN interface allows specification of the temperature profile, in that case the energy equation (Eq. (2.62)) is excluded from the system. Simulations with experimental temperature profiles are common, since measurement of temperature is required for determination of the absolute concentrations in the experiments. In the

modeling, the use of fixed temperatures results in better convergence of the solution. It also becomes possible to use kinetic schemes that do not reproduce the laminar burning velocities, for flame structure studies.

The boundary conditions constrain the mass flux and temperature at the cold boundary [117]:

$$\mathcal{Y}_i = Y_{i,1} + \left(\frac{\rho A Y_i V_i}{\dot{m}} \right)_{j=1\frac{1}{2}} \tag{2.70}$$

$$T_1 = T_g \tag{2.71}$$

where $\mathcal{Y}_i$ is the specified inlet fraction of the species "i", T_g is the specified cold boundary temperature and indices "1" and "$1\frac{1}{2}$" correspond to the first and 1.5-th grid elements. On the hot boundary, i.e., in the product zone, it is required to have zero gradients [117]:

$$\frac{Y_{i,J} - Y_{i,J-1}}{x_J - x_{J-1}} = 0 \tag{2.72}$$

$$\frac{T_J - T_{J-1}}{x_J - x_{J-1}} = 0 \tag{2.73}$$

where "J" corresponds to the last grid element. The hot boundary conditions imply that the spacial domain is selected to be long enough for all gradients to vanish. At the cold boundary, it is allowed to have the heat and diffusive flux into the burner, therefore, in free-propagating flames, the absence of gradients at the cold boundary should be ensured by the user. As in the product zone, it is done by selecting a long spatial domain.

In burner-stabilized flames, mass flow $\dot{m}$ is specified by the user. In the free-propagating flames, $\dot{m}$ is the solution variable, therefore, one additional boundary condition should be specified. In CHEMKIN, it is done by fixing the flame position, i.e., by assigning temperature in one of the grid points to a value above T_g, so that the system of equations is closed.

2.3.4 Stagnation flames

Stagnation flame geometry (see Figure 2.1) can be described by a quasi-1D system of equations, even though the flow is two-dimensional. The stagnation/counterflow model in CHEMKIN is based on the work of Kee et al. [118]. The formulation employs the idea [119] that the quotient of the radial velocity v_r and radius r is a function of the axial coordinate only:

$$\frac{v_r}{r} = f(x) \tag{2.74}$$

The system of equations Eqs. (2.60-2.62) for the axisymmetric stagnation flow contains a modified continuity equation and is supplemented with the radial momentum equation [116]:

$$\frac{d(\rho u)}{dx} + \frac{2\rho v_r}{r} = 0 \tag{2.75}$$

$$\rho u \frac{d(v_r/r)}{dx} + \frac{\rho v_r^2}{r^2} = -H + \frac{d}{dx}\left(\mu \frac{d(v_r/r)}{dx}\right) \tag{2.76}$$

where μ is the gas viscosity and H is a constant eigenvalue [117].

At the cold boundary, it is added that $v_r/r = 0$. If counterflow flames are simulated, then the system has two cold boundaries, defined similarly to the 1D case. The inlet velocities, temperatures and the composition of the reactants can be different at the two inlets. If stagnation flames are simulated, then one of the boundary conditions is defined at the stagnation plane and it includes the axial velocity, temperature and the species' fluxes [117]:

$$u = 0 \tag{2.77}$$

$$T = T_{pl} \tag{2.78}$$

$$\rho Y_i (u + V_i) = 0 \tag{2.79}$$

where T_{pl} is the user-specified temperature of the stagnation plane.

2.3.5 Sensitivity analysis

One of the common tools for investigation of the mechanism performance is the sensitivity analysis, i.e., the determination which elementary reactions have the largest influence on a specific indirect target. The sensitivity coefficient for each reaction, with the forward rate constant represented as Eq. (2.44), is defined as:

$$s_k = \frac{\partial \ln x}{\partial \ln A_k} = \frac{A_k}{x}\frac{\partial x}{\partial A_k} \tag{2.80}$$

where x is the studied quantity (laminar burning velocity, ignition delay or species concentrations) and A_k is the pre-exponential factor of reaction "k". Equation (2.80) implies that s_k relates the change in x to the variation of A_k in normalized units. In CHEMKIN, the sensitivity coefficients for 0D and 1D reactor models do not have to be estimated by a brute-force variation of A_k, but instead can be calculated from the quantities obtained by the CHEMKIN solver during the search for a solution [117].

2.3.6 Uncertainties in the model predictions

The experimental initial conditions, e.g., the mixture composition and inlet temperatures, possess certain uncertainties, thus the results of the modeling with nominal parameters may not correspond to the real measured flame conditions. For that reason, the influence of the uncertainties in the initial mixture parameters can be estimated by performing the simulations with these parameters varied within their accuracy range. This procedure was performed for the NH_3 + air flame structure of Section 3.3.

For the simulations based on the experimental temperature profiles, the resulting radical concentrations are affected by uncertainties in the equivalence

ratio, the inlet flow rate and the experimental temperature. The mass flow controllers give an uncertainty of ±1% in each component's flow rate after calibration and the accuracy of the CARS temperature measurements is ±3% as discussed in Paper IV. Each of the flow rates and temperature were treated as independent factors that affect the peak radical concentrations. Thus the total uncertainty was estimated using the square summation rule, and its components were obtained by re-runs of the models with one of the parameters varied. For the simulations based on solving the energy equation, the uncertainties in the mixture properties affect the flame front position as well as the peak radical concentrations. Since the experimental temperature profiles were not applied, the accuracy of the inlet gas temperature of around ±10 K was incorporated.

Chapter 3

Results

3.1 Validation of the new H_2 mechanism

Laminar burning velocities of the H_2 flames, described in this chapter, were simulated using a new detailed reaction mechanism presented in Paper II. The mechanism was validated against a wide range of conditions which covered ignition experiments in shock tubes and rapid compression machines (RCM) from 900 to 2700 K and from sub-atmospheric pressures up to 87 atm; hydrogen oxidation in flow reactors at temperatures around 900 K from 0.3 up to 15.7 atm; in jet-stirred reactors at 800-1150 K and 1-10 atm; laminar burning velocities in hydrogen + oxygen + inert mixtures from 0.35 up to 25 atm at room and elevated temperatures up to 443 K; hydrogen flame structure at pressures from 0.05 to 10 atm. A comprehensive set of about 140 cases was run to validate the new mechanism, here a few notable examples will be shown, in particular, those indicating the main improvements of the model compared to the previous version [53]. The comparison is also made to the best contemporary model of Keromnes et al. [9]. In the following figures, these models are referred to as "Konnov 2008" and "Keromnes 2013" and plotted with dashed and dash-dotted lines, respectively.

Figure 3.1 from Paper II shows the flow reactor data of Mueller et al. [120] for $H_2 + O_2 + N_2$ mixture at 3.02 atm. The experimental points are plotted with the uncertainties specified in [120]. The modeling data were shifted to the position where the mole fraction of H_2 equals 50% of the initial value. The results from [120] were included in the validation set for the previous version of the mechanism [53], and the discrepancy was found to be significant. For the current version, the agreement was found to be very good.

The previous version of the mechanism [53] was validated against a wide range of ignition delay times measured in shock tubes, however, other types of experiments were not covered. In the current work, the mechanism performance was tested against several studies where species profiles were recorded

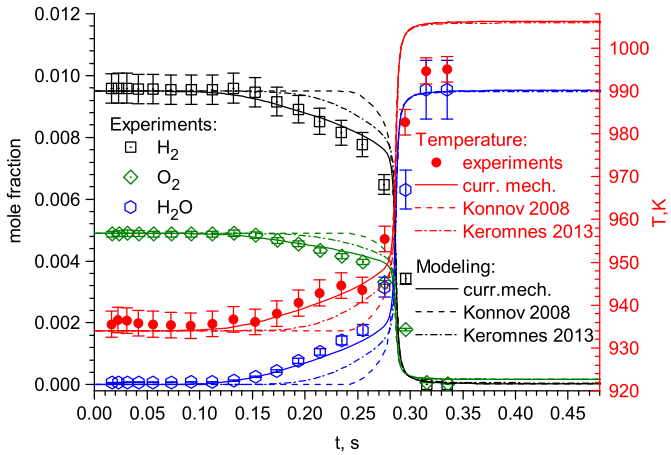

Figure 3.1: *Profiles of major species and temperature in a flow reactor oxidation of a stoichiometric mixture (H_2 = 0.95%, O_2 = 0.49%) at 3.02 atm [120]. The mixture is diluted by N_2.*

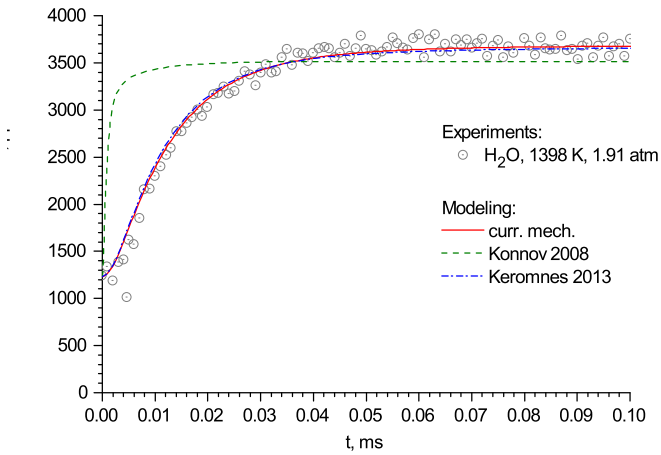

Figure 3.2: *Profile of H_2O in the shock wave decomposition of H_2O_2 [121]. The initial conditions are: H_2O_2 = 2540 ppm, H_2O = 1234 ppm, O_2 = 617 ppm, T = 1398 K, p_0 = 1.91 atm. The mixture is diluted by Ar.*

in shock tubes [121–124]. As an example, a profile of H_2O from H_2O_2 decomposition study of Hong et al. [121] is shown in Figure 3.2 from Paper II. For the conditions of [121,123], there was a significant improvement compared to the previous model [53] due to the change of the rate constants of several reactions. Reaction

$$HO_2 + OH = H_2O + O_2 \qquad \text{(R3.1)}$$

was adopted from Hong et al. [125], which overrode the previously determined value [123]. The experimental data of Hong et al. [121] allowed determination of the rate constants of two reactions:

$$H_2O_2 + OH = HO_2 + H_2O, \qquad \text{(R3.2)}$$

$$H_2O_2\ (+M) = OH + OH\ (+M). \qquad \text{(R3.3)}$$

The rate constant of reaction (R3.2) was directly taken from [121], and for reaction (R3.3), a value from Troe [126] was used, which is close to [121]. These modifications resolved the issues in the predictive ability of the previous version of the mechanism [53] observed by Hong et al. [127] for the conditions of [121]. As Figure 3.2 suggests, there is an excellent agreement between the data of [121] and the predictions of the current model.

Figure 3.3 contains the measurements conducted in a shock tube by Keromnes et al. [9], which constituted a part of the validation set for the mechanism [9]. This figure illustrates the importance of the selection of the ignition criterion for short ignition delays. The experimental ignition delay times are based on $[OH^*]^{max}$, but they are modeled with $(d[OH]/dt)^{max}$ for the purpose of comparison between the three models, since the current mech-

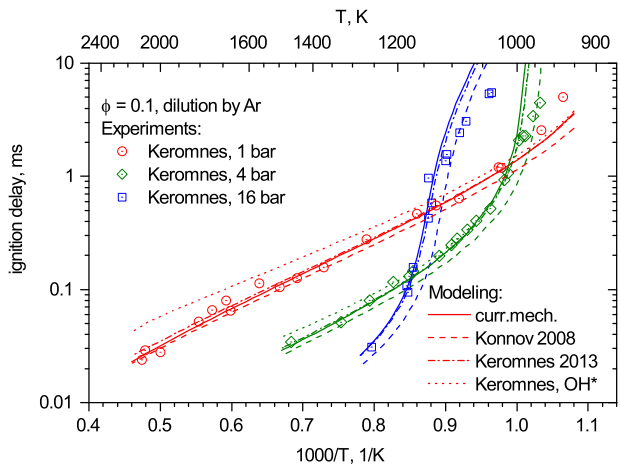

Figure 3.3: *Ignition delay times for lean (ϕ = 0.1) H_2 + O_2 + Ar mixtures at different pressures from the study of Keromnes et al. [9]: p_0 = 1 bar (red circles), p_0 = 4 bar (green diamonds), p_0 = 16 bar (blue squares). The initial concentrations are H_2 = 0.81%, O_2 = 4.03%.*

anism and its previous version [53] do not include excited species' chemistry. The mechanism of Keromnes et al. [9] allows the simulation of [OH*], however, selection of the correct ignition criterion results in a deviation from the experimental data at shorter ignition delays, making the original agreement between the three models and experiments to be misleading. Nevertheless, it can be seen that the current mechanism has an improved performance as compared to the previous version [53].

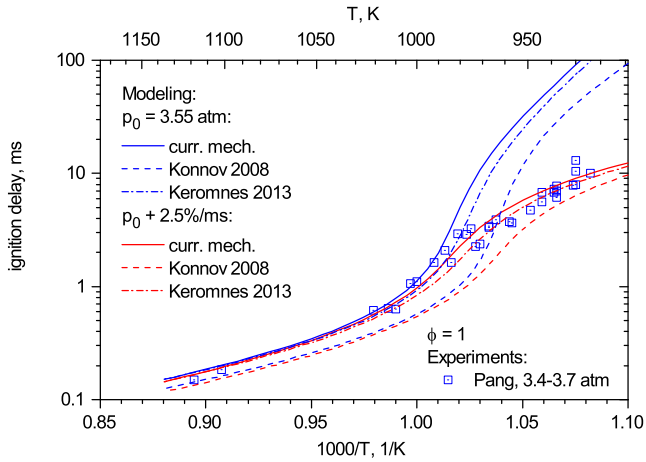

Figure 3.4: *Ignition delay times for H_2 + O_2 + Ar mixtures at pressures around p = 3.4-3.7 atm from the study of Pang et al. [128]. The initial conditions are H_2=4%, O_2=2%. These conditions are modeled at p = 3.55 atm by using the constant volume model (blue curves) and by implementing the experimental pressure profiles (red curves), 2.5%/ms rise.*

The range of data from [9] includes temperatures around and below 1000 K. Hence, the corresponding ignition delay times are of the order of several ms. For such long delay times, the self-ignition processes are generally affected by the facility-related pressure and temperature rise, which accelerate the ignition. The authors of [9] took the gas-dynamic effects into account by recording the pressure and temperature histories of non-igniting mixtures and coupled them to the reactor model by using an in-house written extension to Chemkin II. The gas-dynamic effects can result in a large discrepancy between the modeling and experiments, as evident from Figure 3.3, opposed to the simulation results from [9], where the agreement was found to be very good. If the pressure history is provided together with the published ignition delay data, as in the study of Pang et al. [128], the current mechanism is able to reproduce long ignition delays adequately, as evident from Figure 3.4. It contains the ignition delay times for H_2 + O_2 + Ar mixtures at 3.4-3.7 atm. The simulations with the experimental pressure profiles are compared to the simulations under the common constant-volume assumption. Even though the rise of pressure for different experimental runs varied with temperature, it was found that a single value of 2.5%/ms can be used. The experimental ignition

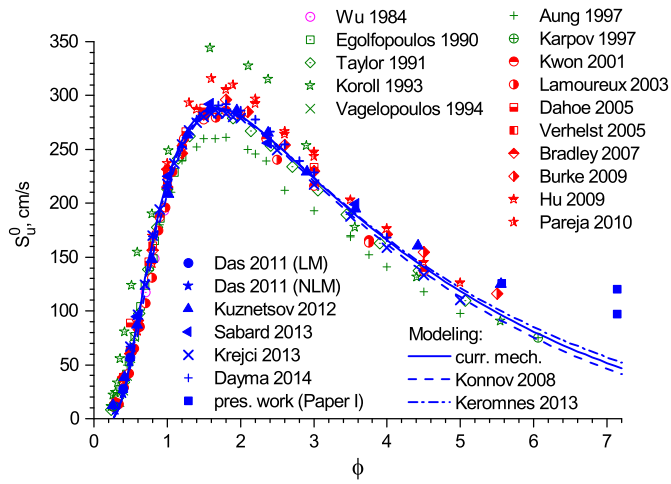

Figure 3.5: *Laminar burning velocity of H_2 + air flames at standard conditions (T = 298 K, p = 1 atm) for ϕ = 0.25-7. The source of experimental data: before 1990 (purple symbols) - Wu and Law [31]; from 1990 to 2000 (green symbols) - Egolfopoulos and Law [24], Taylor [10], Koroll et al. [129], Vagelopoulos et al. [25], Aung et al. [12], Karpov et al. [11]; from 2000 to 2010 (red symbols) - Kwon and Faeth [13], Lamoureux et al. [14], Dahoe [130], Verhelst et al. [15], Bradley et al. [16], Burke et al. [17], Hu et al. [18], Pareja et al. [131]; after 2010: Das et al. (LM - linear model, NLM - non-linear extrapolation) [26, 27], Kuznetsov et al. [19], Sabard et al. [21], Krejci et al. [20], Dayma et al. [22], present work (Paper I).*

delay times are defined by determining $(dp/dt)^{max}$ and $(d[\mathrm{OH}^*]/dt)^{max}$ and subsequent linear extrapolation to the initial values of p and $[\mathrm{OH}^*]$. The same procedure was performed in the modeling: the ignition is defined by extrapolation using $(dp/dt)^{max}$ for the constant volume model, and with $(d[\mathrm{OH}]/dt)^{max}$ to $[\mathrm{OH}] = 0$ for the simulations with the experimental pressure profiles, where it was not possible to use the first criterion.

Figures 3.5, 3.6 from Paper II show the laminar burning velocity of H_2 + air mixtures at 1 atm [10–22, 24–27, 31, 129–131] at room and elevated temperatures, respectively. It can be seen that both the current model and the previous version [53] agree well with the most recent experimental data in a wide range of equivalence ratios except for very lean and very rich flames. As will be shown in Section 3.2.3, in the range where good agreement with the burning velocities was observed, the temperature exponent α (see Eq. (1.1)) also agrees well with the experimental values extracted from, e.g., the recent study of Krejci et al. [20]. In the very lean mixtures ($\phi < 0.5$), the burning velocities from literature possess higher relative scattering and disagree with the model predictions both in terms of S_L, and consequently, in values of α.

Overall, the new H_2 model resolves the issues of the previous version [53], observed in flow reactors and shock-wave decomposition, mostly due to implementation of rate constants of reactions involving HO_2 and H_2O_2, recently

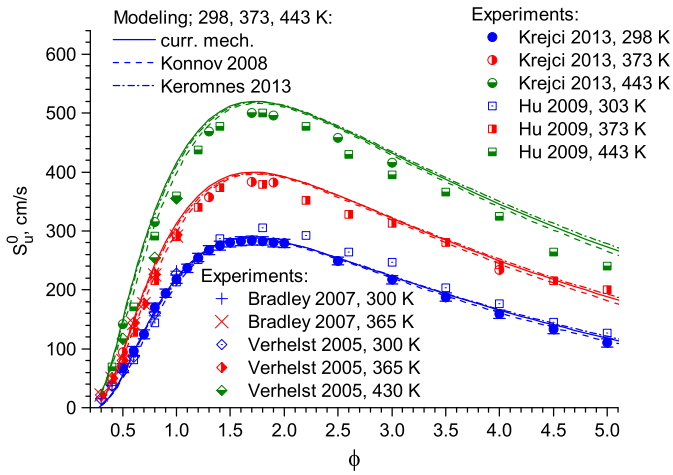

Figure 3.6: *Laminar burning velocity of H_2 + air flames at standard conditions (blue color) and elevated temperatures (≈373 K - red; ≈443 K - green) for ϕ = 0.3-5. The source of experimental data: Krejci et al. [20], Hu et al. [18], Bradley et al. [16], Verhelst et al. [15].*

measured by Hong et al. [121–123,125,132]. In terms of laminar burning velocities and ignition delay times, the three models showed similar results. Olm et al. [133] ranked the performance of 19 H_2 kinetic schemes and found the mechanism of Keromnes et al. [9] to be the best, with the Konnov model [53] being in the short list. It has to be noted, however, that the authors [9] adjusted several rate constants, as opposed to the current model. As the validation results suggest, no rate constant modifications were required to achieve a predictive ability comparable to the model of Keromnes et al. [9].

3.2 Laminar burning velocity of hydrogen flames

3.2.1 Rich near-limiting flames

This subsection is based on the contents of Paper I. The goal of the study was to determine laminar burning velocity of rich near-limiting mixtures of H_2 + air in stretched flames and analyze the influence of the applied stretch correction models. The study revealed a discrepancy between the kinetic modeling and experimental results in the limiting mixture, which occurred for all three tested stretch correction models.

The experimental data on flame propagation in a spherical bomb apparatus ($R(t)$) were obtained in the Institute of Chemical Kinetics and Combustion, Novosibirsk, by Dr. V.V. Zamashchikov, and the corresponding experimental

details can be found in Paper I. The $R(t)$ dependencies were recorded with an optical Schlieren system and processed using three models for stretch correction referred to as LM, NLM1 and NLM2 in Section 2.1.2. The experiments covered two mixtures: 70% H_2 + 30% air and 75% H_2 + 25% air ($\phi = 5.55$ and 7.1, respectively) at pressures 0.7-4 atm.

First, the integration domain for Eqs. (2.10-2.12) was determined. The choice of the time t_0 (which corresponds to a certain R_0) is very important, since it affects the accuracy of the extracted unstretched burning velocity and the Markstein length. Indeed, the influence of stretch appears mainly at small flame radii where the flames might still be affected by the spark ignition. If the selected initial flame front radius R_0 is relatively large, the laminar flame speed weakly depends on flame curvature and the measurement errors increase, especially for the Markstein length. The choice of the initial flame front radius R_0 is usually based on the analysis of experimental or calculated dependencies of the flame speed as a function of the flame radius or stretch. Most often, a single critical radius is applied over a range of pressures and equivalence ratios. In the present work, each experimental dependence of the flame front radius as a function of time has been processed to determine the appropriate t_0. Even when neglecting the impact of the spark and processing all available points using Eqs. (2.10-2.12), the obtained fitted curves $R(t)$ were in apparent agreement with the measurements. However, if the initial time t_0 is considered to be a parameter, the experimental curve $R(t)$ could be processed using the least-square method to obtain R_0, S_b^0 and L_b by removing the initial data points from the dataset step-by-step, that is incrementally increasing t_0 and R_0. As an example, Figure 3.7 from Paper I shows the unstretched flame speed S_b^0, obtained using the three stretch correction models as explained

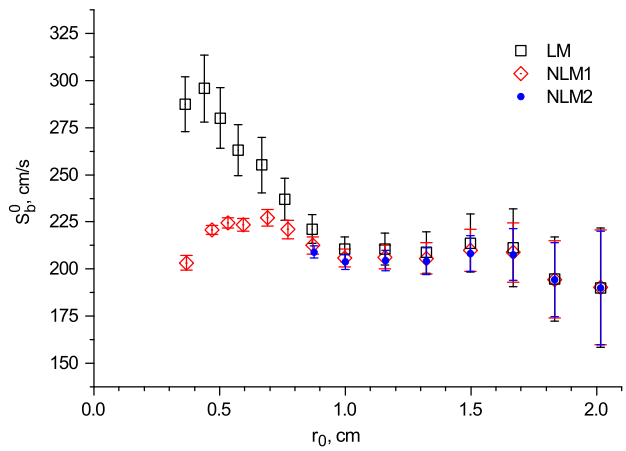

Figure 3.7: *Dependence of the extracted speed S_b^0 of an unstretched flame on the flame front radius R_0 in 70% H_2 + air flame at 3.95 atm: squares – LM; diamonds – NLM1; points – NLM2.*

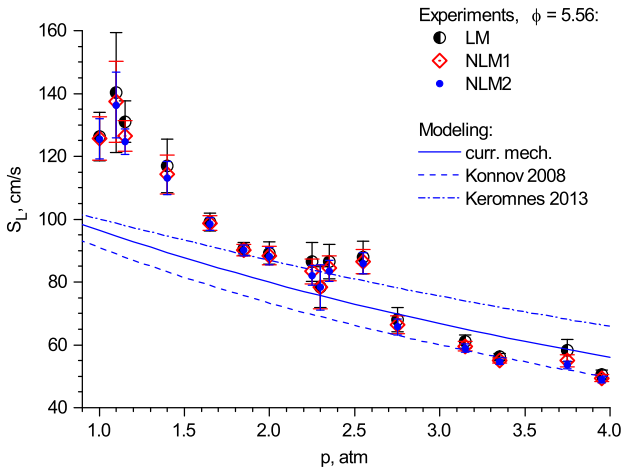

Figure 3.8: *Pressure dependence of the extracted laminar burning velocity in 70% H_2 + air flames. Symbols: experiments, lines: modeling. Circles: LM, diamonds: NLM1, points: NLM2. Solid line: current mechanism, dashed line: Konnov [53], dash-dot line: Keromnes et al. [9].*

in Section 2.1.2. The standard deviations of the least square fit coefficients were considered as the measurement uncertainty and plotted as error bars in Figure 3.7. This approach of data processing allows a clear identification of three distinct regions: from very small initial radii till the critical radius, the extracted characteristics are affected by the spark. Further in time, both the unstretched flame speed S_b^0 and the Markstein length L_b do not vary much, meaning that the linear dependence between the visible flame front speed S_b and flame stretch is valid. Finally, with even higher flame front radii R_0, the uncertainties in both characteristics increase, as discussed above. In the present work, S_b^0 and L_b were extracted at the beginning of the plateau that is close to the critical radius. Even though for some pressures the plateau zone could not be identified, the same critical radii of 10 mm and 15 mm were used for the two investigated mixtures of 70% H_2 and 75% H_2, respectively, over the entire pressure range, since it was shown [134] that the critical radius is scattered within 1-2 mm in a pressure range of 1-10 atm. The values of R_0 used in the present study are in good agreement with available literature data: 7 mm and 12 mm for $\phi = 4.5$ and 5.5, respectively [135]. Consistently with the theoretical models [134,135], the critical radii in rich hydrogen flames increase with equivalence ratio.

Pressure dependence of the extracted laminar burning velocities relative to the unburned mixture, S_L, in 70% H_2 and 75% H_2 flames is shown in Figures 3.8, 3.9. From the two figures it can be concluded that the type of the model for stretch correction has a minor influence on the laminar burning velocity for the present conditions. For both mixtures, LM values are systematically higher than NLM1, and NLM1 is higher than NLM2. However, in

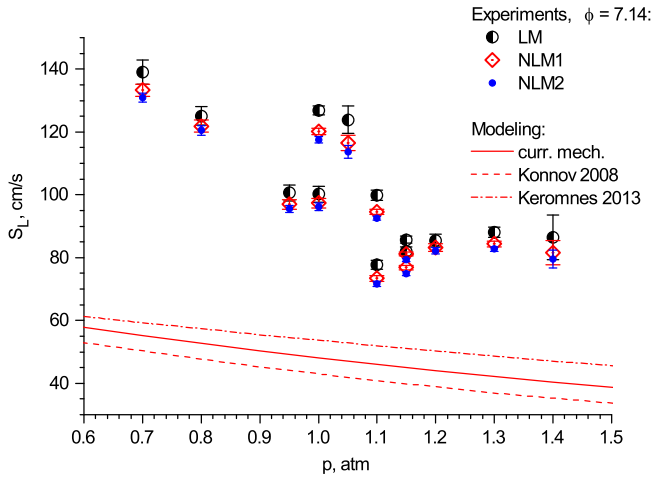

Figure 3.9: *Pressure dependence of the extracted laminar burning velocity in 75% H_2 + air flames. Symbols: experiments, lines: modeling. Circles: LM, diamonds: NLM1, points: NLM2. Solid line: current mechanism, dashed line: Konnov [53], dash-dot line: Keromnes et al. [9].*

the leaner mixture, the difference for each point is within 0.5-4.5 cm/s except two points (up to 6 cm/s), and for the near-limiting mixture this difference is 3-8 cm/s except two points (up to 10 cm/s). Therefore, the linear model can be considered applicable for determination of S_L at the conditions considered. Also shown in both figures are the calculations performed using three detailed kinetic models for hydrogen combustion as described in Section 3.1. For consistency, the selection of mechanisms is different from Paper I, which, however, does not affect the comparison between experiments and simulations. In the leaner mixture, good agreement with current mechanism and its previous version [53] is observed at higher pressures above 2.6 atm, while the mechanism of Keromnes et al. [9] is the closest to the experiments at p = 1.6-2.5 atm. In the near-limiting mixture, Figure 3.9, all models significantly under-predict the extracted laminar burning velocity.

It should be noted that the measurements close to 1 atm in the 70% mixture can be affected by the low number of measured points. Indeed, after the removal of the below-critical radii, the three parameters R_0, S_b^0 and L_b had to be fitted with, e.g., 5 experimental points at 1 atm, with 8 points at 2.25 atm, etc. That could be one of the reasons for the discrepancy with the models at lower pressures in the leaner mixture.

For the mixture of 75% H_2 + air, the experimental values of the flame radius were obtained by averaging a number of measurements in the vicinity of the direction perpendicular to the electrodes on both sides. Instead, only one of these measured points can be chosen randomly at every moment of time in order to evaluate how the uncertainty in the flame radius determination influences the extracted values of S_L. The fitting algorithm of NLM1 was

run several times for selected pressures, and this resulted in the variation of burning velocity about ±20% at $p < 1$ atm and ±10% at $p \geq 1$ atm. The uncertainty of the least square fit coefficients increased about one order of magnitude. However, these results never got close to the model predictions as well as the values processed in a regular way.

Concerning the extracted Markstein lengths L_b, the two non-linear models provided values about 0.5-1.5 mm for the mixture of 70% H_2 + air, and about 2-2.5 mm for 75% H_2 + air. Values of L_b extracted with the linear model were systematically higher, suggesting that for the present conditions, determination of the Markstein lengths requires implementation of the non-linear stretch correction. The Markstein lengths in very rich hydrogen flames increase with equivalence ratio, consistently with the theoretical model [136]. On the contrary, L_b in the present work showed no pressure dependence, opposed to the available literature results [136].

Lipatnikov et al. [137] investigated how S_L and L_b can be affected by the selection of the flame radii domain as well as by the choice of extrapolation model. The authors [137] processed the flame propagation data from Paper I at 1.6 atm in the 75% H_2 + air mixture, which was not considered for S_L determination in the present study, since it was found to be at the limit of extinction. However, even for this extreme case it was shown that a proper definition of the critical radius makes S_L rather weakly dependent on the processing radius range, if a non-linear extrapolation model is selected. The authors recommended NLM1 for the studied conditions, especially for large flame radius ranges, in line with the conclusions of the present work. However, the reasons for the large discrepancy between the experiments and modeling results in 75% H_2 mixtures (Figure 3.9) remain unclear.

3.2.2 Lean flames

This subsection is mostly based on the results presented in Paper III. The first measurements of H_2 + air burning velocity in flat flames were reported, and they possessed a non-negligible difference to the literature values obtained in stretched flames.

Figure 3.10 presents the laminar burning velocities of lean H_2 + air flames at standard conditions (1 atm, 298 K) determined in the present work together with selected set of literature data. The color code is identical to that in Figure 2.2. The S_L values were determined using the relative parabolic coefficient c_r (and they are presented in Paper III) and using the iterative algorithm. As can be seen, at $T_g = 298$ K the difference between the two methods is negligible, since the extrapolation distance is relatively short. The error bars were also found to be very similar, therefore, they are only shown for the values obtained with the c_r method.

As was discussed in Section 2.1.1, the existing scatter in the S_L data at standard conditions can possibly be explained by the data processing methods. For the measurements performed in spherical flames, the results from [22, 23]

obtained with the non-linear stretch correction, are plotted. For the counterflow measurements, since it was shown that burning velocity also varies non-linearly with stretch [32, 33, 138], the data from Das et al. [26, 27] and Park et al. [28] obtained with the non-linear models of Tien and Matalon [32] and Wang et al. [33], respectively, are shown in the figure. Symbols represent the experimental data, while lines show detailed kinetic modeling performed with the current (new) mechanism and the scheme of Keromnes et al. [9].

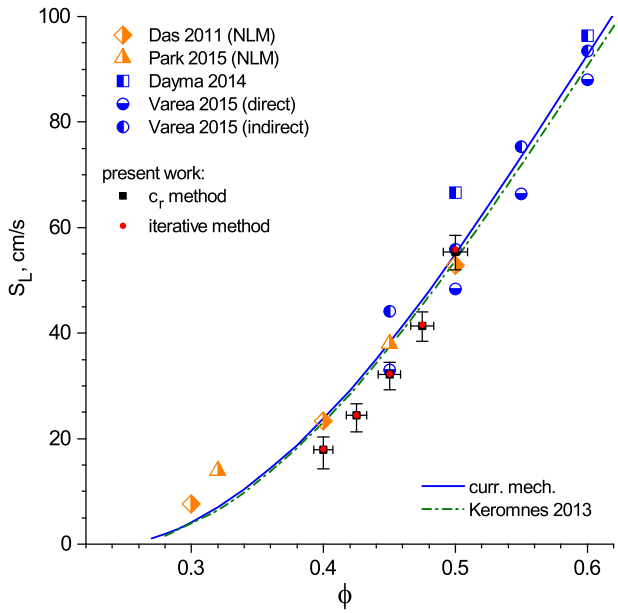

Figure 3.10: *Laminar burning velocity of lean H_2 + air flames at standard conditions (T_g = 298 K, p = 1 atm). Symbols: experiments, lines: calculations using current mechanism and model of Keromnes et al. [9]. Experimental: black – current measurements, c_r method; red - current measurements, iterative method; blue (spherical flame, NLM) – Dayma et al. [22], Varea et al. [23]; orange (counterflow, NLM) – Das et al. [27], Park et al. [28].*

The S_L measured in flat flames are generally located below the values obtained in stretched flames for leaner mixtures. This is in agreement with conclusions of Wu et al. [34], who found that for spherical flame configuration, all extrapolation models overpredict S_L, and the effect increases with decreasing ϕ. The present data, however, were found to be in good agreement with a dataset from the recent experiments in spherical flames by Varea et al. [23]. They presented two sets of data: one was obtained using a technique for direct measurement of the fresh gas velocity before the flame front [139], the second set was obtained by a common method utilizing the density ratio of Eq. (2.1) ("indirect" method). The current measurements agree better with the "direct" set at $\phi = 0.45$, and with "indirect" at $\phi = 0.5$. At the higher ϕ one can note that the difference between the two methods of [23] is smaller

compared to lower ϕ. For leaner mixtures, $\phi < 0.45$, there are two datasets available, by Das et al. [26,27] and Park et al. [28], performed in the counterflow configuration. The flat flame measurements are found to be lower than both datasets, and the difference is beyond the evaluated uncertainty for the present results. Moreover, S_L from the present measurements at $\phi = 0.4$ is only slightly above the point of [28] obtained at $\phi = 0.32$. Considering that the stretched flame results processed with the linear model are generally located above the non-linear data (See Figure 2.2), the flat flames show lower S_L at $\phi < 0.45$ than any of the available literature results. Concerning the comparison with the modeling, experimental results from flat flames disagree with the predictions of both mechanisms, which were found to be close to the measurements of Das et al. [26, 27]. The effects of flame corrugation, apart from the fact that they have received special attention in the present work, act to overestimate S_L, so that they can certainly be excluded from consideration of the source of the difference between the flat and stretched flame data. It can be concluded that the difference in the results at 298 K is of fundamental nature.

Figure 3.11 presents the laminar burning velocities as a function of the unburned gas temperature for different equivalence ratios (symbols) and fits of the S_L values using Eq. (1.1) (lines). Figure 3.11 indicates that the data does not deviate from Eq. (1.1), i.e. each fit is located within the error bars. Also given in Figure 3.11 are the S_L values from the literature obtained in spherical flames [15, 16, 18, 20] with linear extrapolation or in the counterflow burner [26, 27] with a non-linear model. The colors correspond to a specific equivalence ratio and allow comparison of the results from the present work to the literature values.

It can be seen that with increasing T_g, the difference between the values obtained with the c_r method and the iterative method increase, due to a larger extrapolation uncertainty for the former method. The iterative method values are higher, since for the studied mixtures, extrapolation in the c_r coordinates underpredicts S_L. Nevertheless, the S_L obtained with the iterative method were found to be within the error bars of the c_r method values. As in Figure 3.10, the error bars are shown only for the c_r method values. For the iterative method, the error bars at lower temperatures ($T_g \leq 318$ K) were found to be comparable. At higher T_g, the positive error bars were reduced due to eliminated extrapolation uncertainty. The data at $\phi = 0.375$ did not allow the use of the iterative method.

The error bars of Figure 3.11 are asymmetrical, higher at the negative side for lower temperatures, due to the use of c_r, and at the positive side for higher T_g, due to increasing extrapolation uncertainty. With increasing T_g, the temperature difference between the gas and the burner plate decreases and consequently, the flame front moves further away from the burner plate. The flames then become less stable, resulting in a decrease of the maximum attainable parabolic coefficient, $c_r^{max}(V_g^{max})$. The extrapolation distance $(S_L - V_g^{max})$ becomes higher. Concerning the extrapolation uncertainty, it was found to be negligible for $T_g \leq 318K$, ΔS_L^e below 1 cm/s, since it constitutes a minor

fraction of the total positive error bar.

It was observed in the present study that H_2 + air flame stability in the heat flux experiments depends mostly on the temperature difference between the burner plate and unburned mixture. This temperature difference determines the distance between the flame front and the burner, and the trend is in agreement with the conclusions of the numerical studies of Yu et al. [90, 140], who identified "a critical stand-off distance" below which the flame can be stabilized on the burner, and with experimental observations in cellular flames of methane [87] and ethane [88] burning in O_2 + CO_2 oxidizer. These previous results together with the experimental data of the present work point to the possibility of having flat adiabatic flames of H_2 + air at standard conditions for ϕ = 0.4-0.5. In the present work this was demonstrated by stabilizing adiabatic flames at lower temperature of 278 K, i.e., with a larger temperature

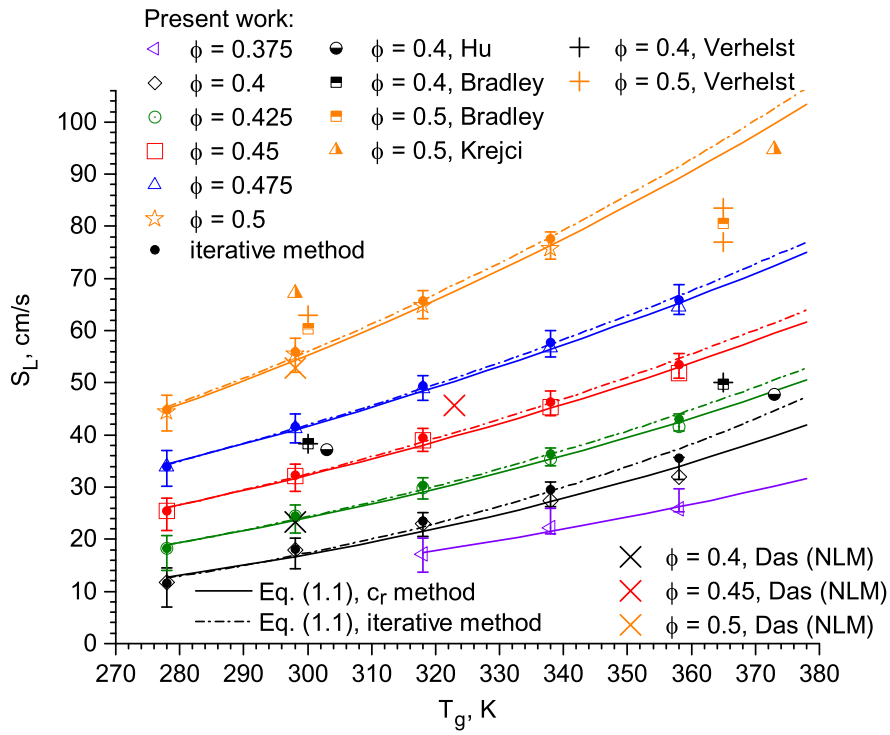

Figure 3.11: *S_L as a function of the unburned gas temperature T_g for different H_2 + air mixtures from the measurements (symbols) and fit with Eq. (1.1) (lines). Color code: violet – ϕ = 0.375; black – ϕ = 0.4; green – ϕ = 0.425; red – ϕ = 0.45; blue – ϕ = 0.475; orange – ϕ = 0.5. The experiments are processed using the relative parabolic coefficient c_r (open symbols, solid lines) and using the iterative method (filled dots, dash-dotted lines). The data of the present work are compared to Hu et al. [18], Bradley et al. [16], Krejci et al. [20], Verhelst et al. [15], Das et al. [26, 27].*

difference between the gas mixture and the burner plate. For higher T_g, burner plate temperature had to be increased in order to obtain flat adiabatic flames.

3.2.3 Temperature dependence of S_L

This subsection is based on Papers II and III, and it is related to the temperature dependence of H_2 flames. The goal of the work was to study the behavior of the temperature exponent α in mixtures with different equivalence ratios, dilution ratios and unburned gas temperatures. Based on the observed experimental and numerical results, it was confirmed that α is a function of all of these parameters and cannot be treated as constant.

The new mechanism was employed to investigate the temperature dependence of the laminar burning velocity of H_2 flames. Figure 3.12 presents power exponents α of H_2 + air flames at standard conditions. The values were obtained with the heat flux method in present work, taken from literature [15,37–40] or extracted from the available S_L data [16,18,20,21,26,27,129,141]. The experimental and modeled temperature intervals are given in the legend of the figure or specified explicitly for the experimental points at $\phi = 0.375$, 0.5, where they were different. The error bars of α were evaluated as described in Section 2.1.4. The uncertainties $\Delta S_L^{T_i}$ were taken from the corresponding studies ([16,20,21,26,129] and from [142] for Verhelst et al. [15]) or evaluated at 95% confidence level from the burning velocity scattering if the uncertainty was not presented directly (for H_2 + O_2 mixtures discussed later in the text). For the experiments of Koroll et al. [129] and for the point $\phi = 0.45$ of Das et al. [26, 27], the burning velocities had to be interpolated, since they were obtained at different equivalence ratios at room and elevated temperatures, and this additional uncertainty was added to $\Delta S_L^{T_i}$. For the study of Hu et al. [18], there was no information available regarding $\Delta S_L^{T_i}$, thus $\Delta\alpha$ was estimated as the standard error of the linear regression coefficient. The same was done for the point $\phi = 0.8$ of [15], where the fitted with Eq. (1.1) burning velocities stood outside the experimental uncertainty interval $S_L^{T_i} \pm \Delta S_L^{T_i}$. For all other cases and studies, where the values of α were based on more than two experimental points, fitted burning velocities lied within this interval.

The vertical error bars on α determined with the c_r method are strongly asymmetrical, higher at the positive side, as a result of larger negative S_L error bars at lower temperatures, and positive error bars at higher temperatures, the latter due to the increased extrapolation uncertainty (See also Figure 3.11). Both factors tend to increase α. The largest error bars are at $\phi = 0.375$, this is due to a relatively narrow temperature interval of just 40 K visited at this equivalence ratio: the flames were accessible from 318 K to 358 K only. The values of α and their uncertainty intervals obtained using the iterative method are very similar to the quantities that correspond to the c_r method.

The two kinetic models were found to give almost identical results. Comparing the calculations to the experimental data, it can be observed that they are in excellent agreement with recent measurements of Krejci et al. [20], who

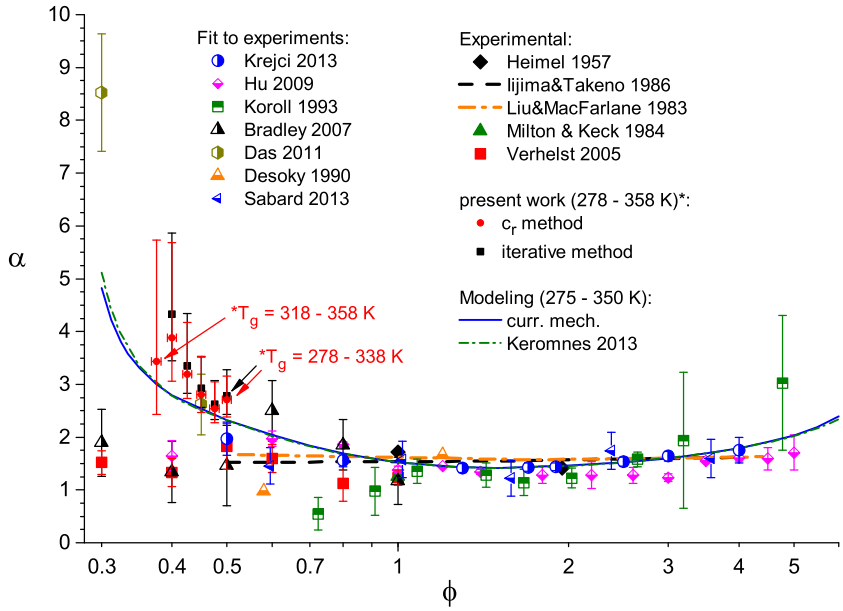

Figure 3.12: *Power exponent α for H_2 + air flames at standard conditions. Red points: present work, c_r method; black squares: present work, iterative method; solid symbols and thick lines: experiments, Heimel [37], Liu and MacFarlane [39], Iijima and Takeno [38], Milton and Keck [40], Verhelst et al. [15]; open symbols: α acquired using S_L data from Koroll et al. [129], Bradley et al. [16], Hu et al. [18], Das et al. [26, 27], Sabard et al. [21], Krejci et al. [20], Desoky et al. [141]; thin lines: modeling with the current mechanism and model of Keromnes et al. [9].*

covered the range of equivalence ratios $\phi = 0.5 - 4$. In this range, most of the available data do not disagree with the models. The same was observed for S_L itself (see Figure 3.5).

However, in the very lean mixtures ($\phi < 0.5$), not covered in [20], different studies predict contradictory trends. The experimental results from the flat flames of the present work provide support for the modeling trend, i.e. the rise of α as the mixture gets leaner. Even with comparably large error bars at lower ϕ, as a result of increased relative uncertainty of low S_L, and narrow temperature interval for $\phi = 0.375$, it is evident that α is significantly larger compared to the commonly adopted values of ≈ 1.5. Most of the available experimental studies indicate α independent on ϕ, except the study of Das et al. [26,27], which is also the only source for α obtained a) from the measurements using the counterflow burner, and b) by performing non-linear stretch correction. For the point $\phi = 0.45$, the agreement between the value extracted from the data of [26,27] and the present experimental results is excellent, even though a difference was observed for S_L. The point $\phi = 0.3$ cannot be compared directly, since it was not accessible with our experimental apparatus, i.e. the burning velocities would become too low, $S_L \ll 10$ cm/s (see Figure 3.10).

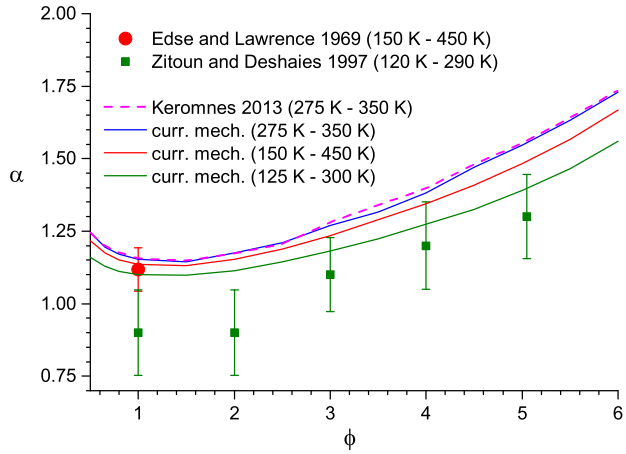

Figure 3.13: *Power exponent α for H_2 + O_2 flames at atmospheric pressure. Symbols: experimental data of Edse and Lawrence [143] and Zitoun and Deshaies [144], lines: modeling*

In general, α from [26, 27] follow the same trend as values from the present work. This is additional evidence of the deviations in spherical flame data processed with linear extrapolation model in lean mixtures, since none of such studies were able to reproduce the trend from modeling and flat flame experiments. From Figure 3.11 it is seen that S_L is overestimated in the spherical flame studies at room temperature, and at elevated temperatures the results are in better agreement with the heat flux measurements. This explains the observed difference in α.

As can be seen from Figure 3.12, for the H_2 + air mixtures there is a large variety of experimental data, resulting in a large scattering of the extracted values of α. For the H_2 + O_2 + N_2 mixtures of variable dilution, the amount of available experiments is limited. Two studies exist, where the laminar burning velocity of pure H_2+O_2 mixtures was measured from cryogenic temperatures to room conditions: Edse and Lawrence [143] and Zitoun and Deshaies [144]. The comparison between the measurements and modeling for H_2 + O_2 mixtures is shown in Figure 3.13 (taken from Paper II). The error bars for the values of α for both studies [143, 144] were evaluated in the present work from the experimental scattering of the burning velocities.

The investigated temperature range for [143] is about 150 K wider than in [144] and does not match the modeling conditions of Figure 3.12 (275-350 K). For fair comparison, the modeling results in Figure 3.13 are shown for three ranges of temperature. It was found that the effect of temperature on the extracted value of α is non-negligible. The rise of α in the rich mixtures is well predicted by the modeling, though the calculated values are somewhat higher than the experimental ones.

As follows from Figure 3.13, the power exponent α depends on the tem-

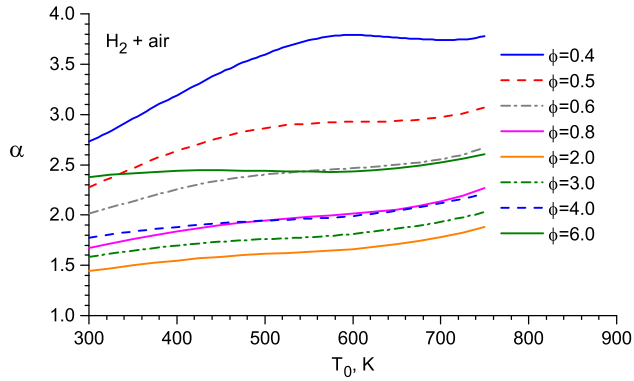

Figure 3.14: *Effect of equivalence ratio and central temperature on power exponent α for H_2 + air mixtures. The new H_2 mechanism was used in the simulations.*

perature range covered. It was observed by Hu et al. [18], who studied the variation of α by extending the temperature range from 300-350 K to 300-950 K. This resulted in values averaged over a very wide temperature range. In the present work, the variation of α as a function of temperature is presented as $\alpha(T_0)$, where at each central T_0 the fitted interval was chosen to be 100 K: from $T_0 - 50$ K to $T_0 + 50$ K. As an example, the results obtained with the current model for H_2 + air mixtures are shown in Figure 3.14 (from Paper II).

The variation of α is significant in lean mixtures, while for conditions close to stoichiometric, the change of α over the whole 500 K range does not exceed 0.5. Nevertheless, this questions the validity of Eq. (1.1) as a correlation equation for wide temperature ranges. Figure 3.14 suggests that α increases with temperature, meaning that the burning velocity rises faster that the prediction of Eq. (1.1) outside the fitting domain. This can result in a significant offset from the real value of S_L, if it is extrapolated from the experimental data to higher temperatures. Also, due to uncertainty range of the experimentally determined α, the uncertainty in the predicted S_L would increase with temperature.

Finally, available results for stoichiometric H_2 + O_2 + N_2 mixtures with different amount of N_2 can be combined in one plot. The modeling was done in the range of 250-500 K and the comparison with available literature data is shown in Figure 3.15 (taken from Paper II). Apart from the already mentioned sources [18, 21, 143, 144], the results of Kusharin et al. [46], Paidi et al. [145] were used. It can be seen that agreement with the modeling is good, especially for higher dilutions. As was shown before, the rapid rise of α was also observed in the lean H_2 + air flames, and in both cases it was supported by experimental observations. Such behavior occurs when the mixture composition approaches the flammability limits. It can be concluded that if S_L is determined with Eq. (1.1) in these mixtures, the exact value of the power exponent α has to be known, since the use of $\alpha \approx 1.5$ can lead to underprediction of S_L.

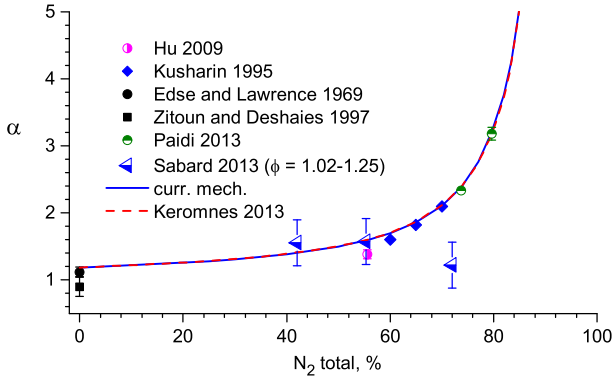

Figure 3.15: *Power exponent α for stoichiometric H_2 + O_2 + N_2 flames at standard conditions and variable N_2 content. Symbols: experiments of Hu et al. [18], Sabard et al. [21], Edse and Lawrence [143], Zitoun and Deshaies [144], Kusharin et al. [46], Paidi et al. [145], lines: modeling.*

3.3 Structure of NH_3 + air flames

This section is based on the contents of Paper IV, which is related to structure of atmospheric-pressure ammonia + air flames. Concentration profiles of major and minor species were for the first time recorded at these conditions using spectroscopic methods. The main objective of the kinetic part of the study was to rank the performance of four contemporary detailed reaction mechanisms, analyze sensitive reactions and point the directions for future development.

Ammonia (NH_3) is an important component in H/N/O chemical systems, and it is a hydrogen carrier. The flame structure of ammonia is relatively simple compared to hydrocarbon flames, therefore all major intermediates, i.e. OH, NH_2, NH, NO, can be measured with spectroscopic methods. In the present work, the structure of premixed ammonia + air flames, burning at atmospheric pressure under strain-stabilized conditions on a porous-plug burner, has been investigated using laser-diagnostic methods. Quantitative profiles of NH, OH and NO were measured employing laser-induced fluorescence (LIF), and temperatures and oxygen concentrations were obtained with Coherent Anti-Stokes Raman Spectroscopy (CARS). Details of the experimental procedure and data quantification can be found in Paper IV, since they are outside the scope of the present work, and in the following, the results of the study will be discussed. The flames of equivalence ratios $\phi = 0.9$, 1.0, 1.2 were stabilized by aerodynamic strain as explained in Section 2.2 and modeled under stagnation flame geometry as described in Section 2.3. The modeling was performed with the energy equation (Eq. (2.62)) to simulate temperature and O_2 concentrations, and experimental temperatures were used to determine the radical concentrations. For the stoichiometric flame, the fuel + air mixture was diluted with a small amount of nitrogen to lift the flame further from the

burner. The stabilizer was put 16.2 mm above the burner surface.

Four detailed reaction mechanisms were selected to model the experimental flame conditions. Two mechanisms are based on the work of Konnov and de Ruyck [146]: the reduced model of Duynslaegher et al. [147] and the mechanism of Shmakov et al. [148]. The third mechanism considered is from Mendiara and Glarborg [149], with the H/N/O subset developed by studying NH_3 oxidation in a flow reactor [150]. Finally, the last model was recently developed by Klippenstein et al. [151], and it is also based on the work of Glarborg and co-workers [149, 152, 153]. In the following, as in Paper IV, the four models considered will be referred to as Model 1, standing for the scheme of Mendiara

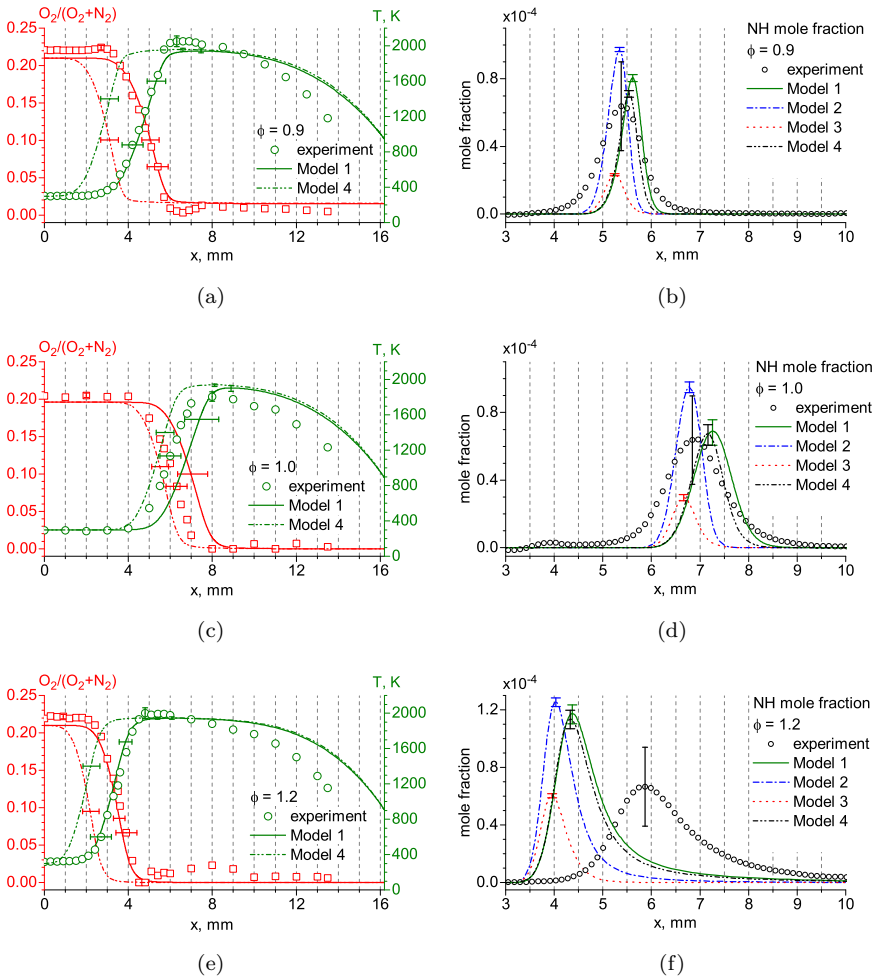

Figure 3.16: *Temperature and O_2 concentration profiles (left) and NH concentrations (right) for the flames with $\phi = 0.9$ (a,b), $\phi = 1.0$ (c,d), $\phi = 1.2$ (e,f). Symbols: experiments, lines: modeling. Colors on the left panels: green – temperatures, red - $O_2/(O_2 + N_2)$.*

and Glarborg [149], Model 2 for Shmakov et al. [148], Model 3 for Duynslaegher et al. [147] and Model 4 for Klippenstein et al. [151].

The left panel of Figure 3.16 (adapted from Paper IV) shows temperature and relative O_2 profiles in the studied flames. The experimental uncertainties are plotted as error bars on symbols (measurement uncertainties) and modeling lines (mixture parameters uncertainties). Only Models 1 and 4 were able to reproduce the flames detached from the burner when the experimental temperature profiles are not used as an input, and these results are shown in Figure 3.16. The two other models instead predicted flames stabilized on the burner, indicating an overestimated S_L, which has to be exceeded by the inlet flow for the flame to detach from the burner. From Figure 3.16 it can be seen that the shapes of the temperature and O_2 profiles are very well reproduced by Models 1 and 4 for all flames. However, in terms of absolute values and flame front positions, agreement is very good in the lean and rich flames for Model 1, whereas Model 4 showed some discrepancy. For the stoichiometric flame, both models are in fair agreement with the measurements. Comparing Models 1 and 4 with each other, Model 4 predicts flames slightly closer to the burner than Model 1 due to higher S_L.

The comparison between the experimental NH, OH and NO profiles and modeling is presented in Figures 3.16, 3.17 (adapted from Paper IV). Models 1, 2 and 4 predict similar maximal NH concentrations (right panel of Figure 3.16) for all three flames, whereas the values obtained with Model 3 are a factor of 2-3 lower. The experimental peak NH concentrations show good agreement with Models 1 and 4 at lean and stoichiometric conditions, but in the rich flame the experimental values become comparable to the predictions of Model 3 (about 60 ppm). Since Model 1 showed good agreement with the rich oxygen-enriched NH_3 flames of Chou et al. [154], it was concluded that the experimental NH concentrations obtained in the rich flame might be underestimated.

For OH concentration profiles, presented in the left panel of Figure 3.17, all models show satisfactory agreement with the experimental data, however, a tendency of under-prediction is observed in the lean flame for all models, as shown in Figure 3.17(a). In the rich flame, Figure 3.17(e), there is agreement between Models 1, 2, 4, while Model 3 predicts higher OH concentrations. Differences in peak values and positions are observed between all models in the stoichiometric flame. Nevertheless, all experiments and model predictions of peak OH concentrations lie within the specified error bars. For the stoichiometric flame in Figure 3.17(c), the influence of the mixture parameters uncertainty on the peak OH position is also shown for Models 1 and 4 by horizontal error bars. For Models 2 and 3, as well as for all other experimental cases, the peak radical positions were found to be insensitive to the variations in the initial mixture parameters within their accuracy range.

All models predict similar NO concentrations in the product zone and show good agreement with experimental data in the lean flame Figure 3.17(b). Lower NO levels are obtained for the stoichiometric case Figure 3.17(d) from the measurements, for which the model predictions also differ. The lowest NO

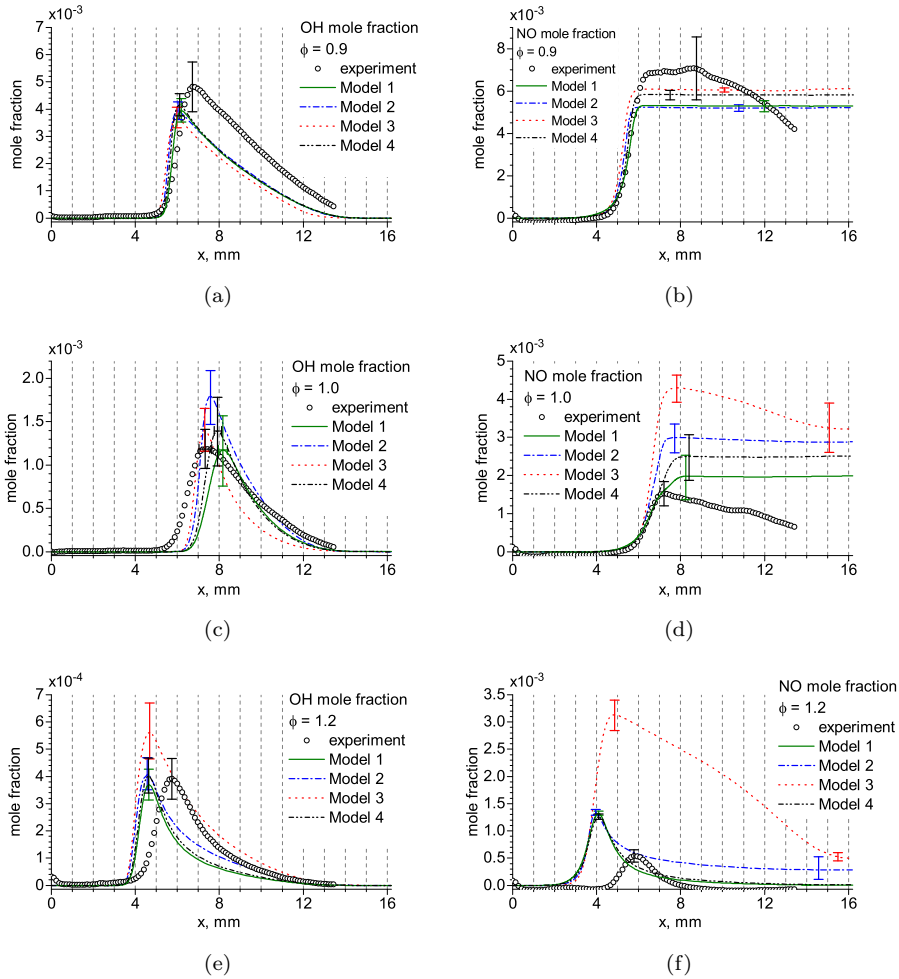

Figure 3.17: *OH (left) and NO (right) concentration profiles for the flames with ϕ = 0.9 (a,b), ϕ = 1.0 (c,d), ϕ = 1.2 (e,f). Symbols: experiments, lines: modeling.*

level, and closest agreement to the measurements, is observed for Model 1. In contrast to the model predictions, experimental NO concentrations in the lean and stoichiometric flames decrease in the post-flame zone, which can be possibly attributed to effects of signal absorption.

For the rich flame Figure 3.17(f), further decrease of the experimental NO concentration can be seen, however, values from all models are higher than the measurement results. NO profiles of Models 1, 2 and 4 are similar in shape to the experimental data and predict peak NO concentrations around a factor of 2.5 higher, Model 3 predicts NO profile very different in shape and magnitude compared to the other models as well as to the experimental data. Here it should be noted that the modification proposed by Shmakov et al. [148] to the original Konnov and De Ruyck mechanism [146], i.e. substitution of the

reaction

$$NH+H_2O=HNO+H_2 \quad \text{(R3.4)}$$

by formation of the NH_2OH radical:

$$NH+H_2O=NH_2OH \quad \text{(R3.5)}$$

has made a major improvement for the simulation of the studied flames with Model 2, since the performance of the mechanism from [146] was found to be very close to Model 3, which does not implement this modification.

The larger error bars on the modeling lines for the stoichiometric flame (middle panels in Figures 3.16, 3.17) indicate that in this case the flame structure is more sensitive to the exact value of the equivalence ratio, compared to the lean and rich flames. For the stoichiometric flame, it is interesting to note that Model 1 predicts the peak of OH to occur further downstream compared to other models, and about 1.3 mm further compared to experiments, which is beyond the experimental uncertainty in the determination of the spatial coordinate (0.3 mm).

Temperature and O_2 profiles measured in the rich flame show good agreement with Model 1 (Figure 3.16(e)), and the experimental NH, OH, and NO profiles are positioned consistently with respect to each other. However, comparing the positions of the radical profiles with the temperature data, an offset in position between experimental temperature and radicals is suggested, since the maximum radical concentrations (bottom panels of Figures 3.16, 3.17) are located in the post-flame zone (cf. Figure 3.16(e)). The consistent downstream location of the radical profiles suggests that an offset exists in the experimental temperature data. This would in turn suggest that Model 1 also overpredicts the flame speed for rich NH_3 flames, though less than the other three. This correlates with freely propagating flame calculations of S_L = 8.9 cm/s for Model 1, compared with S_L = 5-7 cm/s at ϕ = 1.2 [155–157]. An offset in experimental temperature data would also explain the observed difference in position between the experimental and modeled concentration profiles, since the latter were obtained using experimental temperatures as input.

Summarizing the behavior of the four models, Model 1 performs better or similar compared to the other three models for all studied flame conditions. Therefore, it was decided to investigate the radical concentration sensitivity for this model in an attempt to analyze the impact of the uncertainty in the rate constants on its performance. The definition of the A-factor sensitivity coefficients was given in Section 2.3.5. The results for the three flames are presented in Table 3.1. Sensitivity coefficients were analyzed at the peak position of each radical profile and the sensitive reactions (numbered in Table 3.1) were selected by their place in the top-20 sensitivity chart for nine cases (three radicals in three flames, lower number meaning higher sensitivity). The reactions are sorted by their relative importance in all cases, and Table 3.1 also presents signs of the sensitivity coefficients (after the position in the chart) and sources for the individual rate constants. The notation ">20" refers to a reaction outside 20 most sensitive at the corresponding conditions. In addi-

Table 3.1: *Sensitivity analysis for Model 1.*

No.	Reaction	Ref.	Position in the sensitivity chart								
			NH 0.9	NH 1	NH 1.2	OH 0.9	OH 1	OH 1.2	NO 0.9	NO 1	NO 1.2
93	NH_2+NH=N_2H_2+H	[158]	2-	1-	1-	11+	4+	6+	>20	8+	13+
110	NH+NO=N_2O+H_2	[159]	7-	8-	14-	5+	17+	>20	1-	1-	1-
	NH+NO=N_2O+H										
	NH+NO=N_2+OH										
	NNH+O=NH+NO										
84	NH_2+O=HNO+H	[152]	4-	4-	4-	18+	>20	>20	2+	3+	2+
	NH_2+O=NH+OH										
104	NH+OH=HNO+H	[158]	3-	5-	5-	>20	15-	13-	3+	2+	15+
	NH+OH=N+H_2O										
1	H+O_2=O+OH	[160]	6-	16+	9-	1-	2-	1-	>20	>20	8+
83	NH_2+H=NH+H_2	[150]	5+	2+	2+	9+	14+	2-	>20	>20	18-
87	NH_2+OH=NH+H_2O	[158]	1+	3+	6+	15+	>20	8-	7-	>20	>20
14	OH+H+M=H_2O+M	[48]	>20	>20	>20	2-	1-	>20	20-	7-	>20
37	NO+H(+M)= HNO(+M)	[161]	18-	12+	>20	3+	3+	9+	14+	6+	>20
102	NH+H=N+H_2	[150]	14-	6-	3-	>20	>20	5-	>20	>20	>20
98	NH_2+NO=NNH+OH	[153]	20-	18+	>20	>20	5+	>20	4-	19-	3-
	NH_2+NO=N_2+H_2O										
149	N_2H_2+M=NNH+H+M	[150]	>20	17+	10+	>20	11+	3+	>20	15+	>20

tion, the branching channels of the sensitive reactions, if taken from the same sources, are given in Table 3.1 under the main channels, some of them also appeared in the top-20 charts. The reactions are numbered as in Model 1. To modify Model 1, rate constant expressions taken from other sources, or varied within their uncertainty range, were substituted into the model one by one. Selected results of the individual rate constant variation are shown in Figure 3.18 (adapted from Paper IV).

It can be seen that changes in the individual rate constants do not produce a significant impact on the performance of Model 1. For OH and NO concentrations in the stoichiometric flame, the results calculated with updated rate constants never exceeded the accuracy range caused by the experimental uncertainties in flows and temperatures. For NO in the lean and rich flames, where the uncertainties are lower, the impact can be distinguished from the error bars. However, for the conditions where the discrepancy between the modeling and experiments is significant (OH at $\phi = 0.9$, NO at $\phi = 1.2$), the variation of individual rate constants did not reduce it to any considerable extent. NO profiles in the lean and stoichiometric flames were found to be more sensitive to the rate constant variation. The original Model 1 underpredicts NO in the lean flame and overpredicts the experiments in the stoichiometric flame, but, as can be seen from Table 3.1, the most sensitive reactions act similarly on both profiles and therefore no modifications can be proposed. For NH, the model performance could possibly be improved in the rich flame, however, no individual reactions were found to change NH concentration significantly. It was concluded that remaining uncertainties of the rate constants implemented in the recent H/N/O models are difficult to scrutinize unambiguously due to insufficient accuracy of the experimental methods.

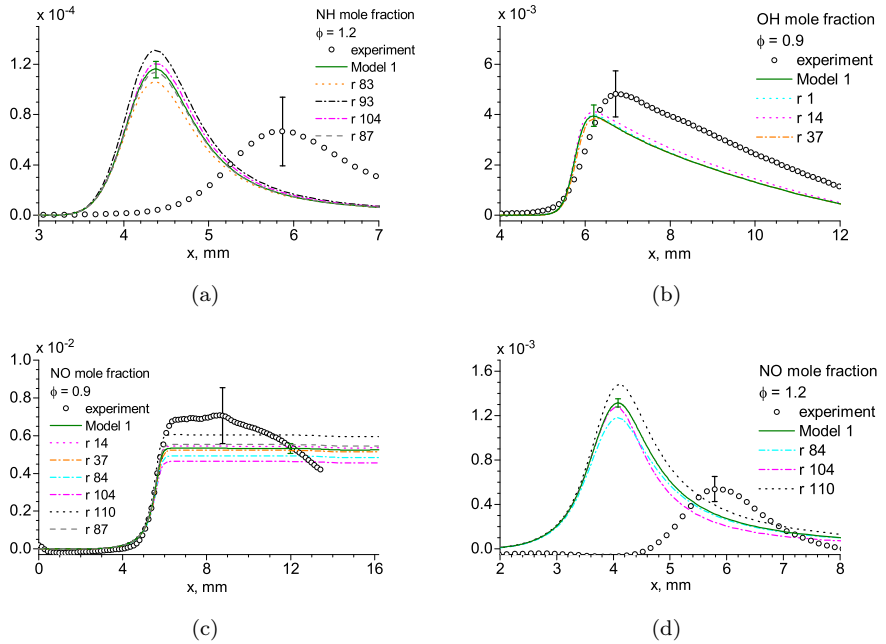

Figure 3.18: *Rate constant variation for Model 1. Symbols: experiments, solid lines: original predictions of Model 1, other: Model 1 with modified rate constants.*

3.4 Studies of flame structure based on HCO and H_2O spectroscopic measurements in CH_4 flames

The contents of this section is based on Papers VI and VII. The goal of the HCO study (Paper VI) was to test the adequacy of the contemporary kinetic mechanisms at ultra-rich conditions, relevant to syngas production. The objective of the H_2O absorption measurements was to test the feasibility of FLICAS for determination of temperature in flames.

3.4.1 ICLAS in rich low-pressure flames

Rich CH_4 mixtures are relevant to hydrogen energy, since partial oxidation of CH_4 can be used for syngas production:

$$CH_4 + \tfrac{1}{2}O_2 \rightarrow CO + 2H_2 \qquad \text{(R3.6)}$$

However, most of the known chemical mechanisms related to methane oxidation are optimized for conditions that differ considerably from those used in the syngas production. To investigate the performance of two commonly used reaction schemes for CH_4 combustion, GRI 3.0 [52] and Aramco mech. 1.3 [162], under very fuel-rich conditions, HCO concentrations were measured with in-

Table 3.2: *Composition of the studied CH_4 flames.*

eq. ratio	CH_4	O_2	N_2
$\phi = 1.0$	0.1119	0.2239	0.6642
$\phi = 1.5$	0.2842	0.3789	0.3368
$\phi = 1.6$	0.3333	0.4167	0.2500
$\phi = 1.7$	0.3616	0.4247	0.2137
$\phi = 1.9$	0.4868	0.5132	0

tracavity laser absorption spectroscopy (ICLAS). The experimental setup and methodology are presented in Section 2.2.2, the method was used previously to demonstrate HCO detection in a stoichiometric CH_4 + air flame [163]. In the present work, rich CH_4 flames were considered, and their composition is listed in Table 3.2. Temperature profiles, necessary for data quantification, were acquired with two-line OH LIF. Different N_2 dilution ratios in the mixtures of Table 3.2 were necessary to stabilize the flame and have an approximately constant stand-off distance from the burner surface.

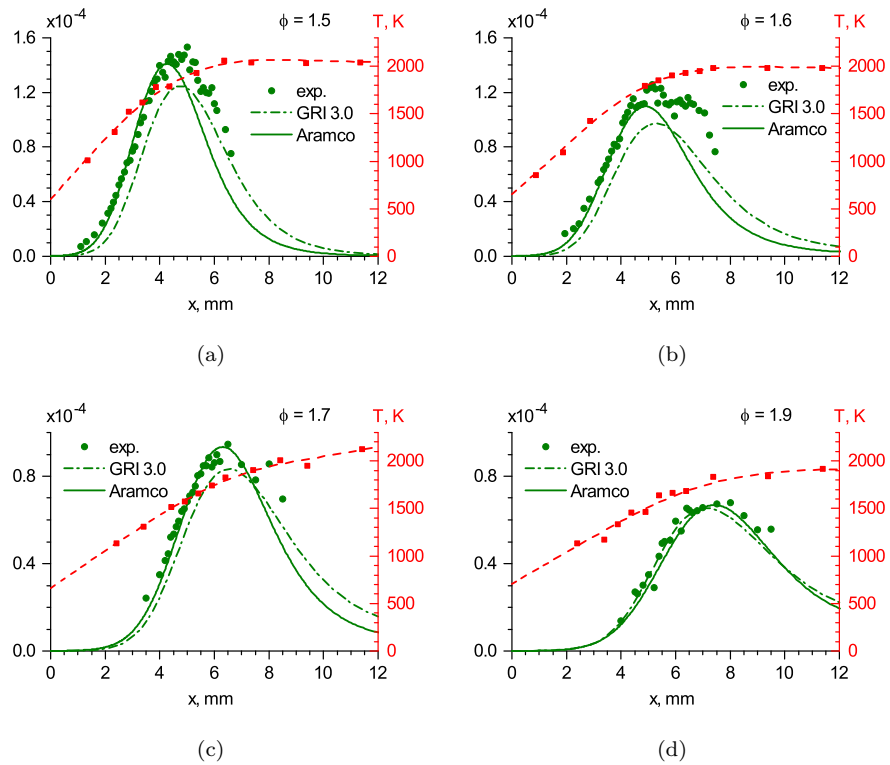

Figure 3.19: *HCO mole fractions (green) and temperatures (red) for the CH_4 flames at $\phi = 1.5$ (a), $\phi = 1.6$ (b), $\phi = 1.7$ (c) and $\phi = 1.9$ (d). Symbols: experiments, lines: temperature spline and modeling.*

Figure 3.19 (adapted from Paper VI) shows the experimental and modeled HCO mole fractions in the rich flames. Overall, very good agreement was observed between ICLAS data and Aramco mech. predictions, while GRI 3.0 showed a very slight difference. However, even though very close results were obtained with the two models, the pathways of HCO formation and consumption differ in GRI 3.0 and Aramco mech. That was concluded from the sensitivity and rate-of-production analysis. As an example, HCO sensitivity in the flame with $\phi = 1.7$ for the two models is shown in Figure 3.20 (from Paper VI). Both mechanisms showed a high importance of HCO decomposition reaction:

$$HCO + M = H + CO + M \tag{R3.7}$$

especially when H_2O acts as a third body. The biggest difference between the two mechanisms was observed for the reaction between methyl radical and oxygen atom:

$$CH_3 + O = CH_2O + H \tag{R3.8}$$

$$CH_3 + O \rightarrow CO + H_2 + H \tag{R3.9}$$

In GRI 3.0, both channels (R3.8) and (R3.9) are present, and HCO concentration is affected by the branching ratio between the channels. Aramco mech. has only the first channel (R3.8), and effect of the second is balanced by modifications in the rate constants of other reactions.

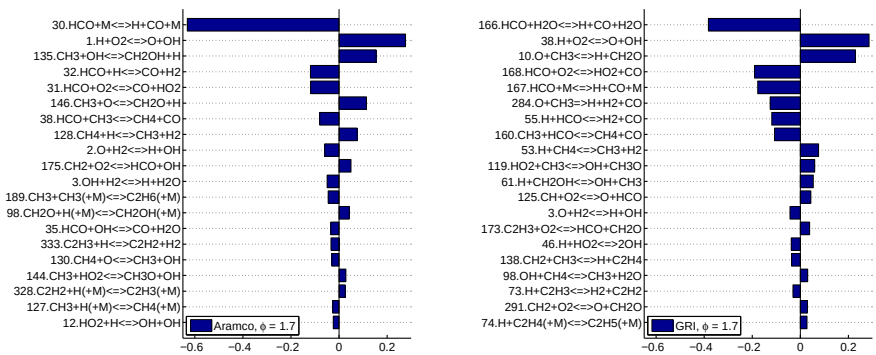

(a) (b)

Figure 3.20: *Normalized sensitivity coefficients of the maximum HCO concentration in the flame at $\phi = 1.7$ obtained for Aramco mech. (a) and GRI 3.0 (b).*

3.4.2 FLICAS in atmospheric-pressure flames

The goal of the FLICAS measurements was to record H_2O absorption in order to test the feasibility of the technique for determination of temperature and concentrations in flames. The experimental methodology was presented in Section 2.2.2, and the measurements were performed in atmospheric-pressure

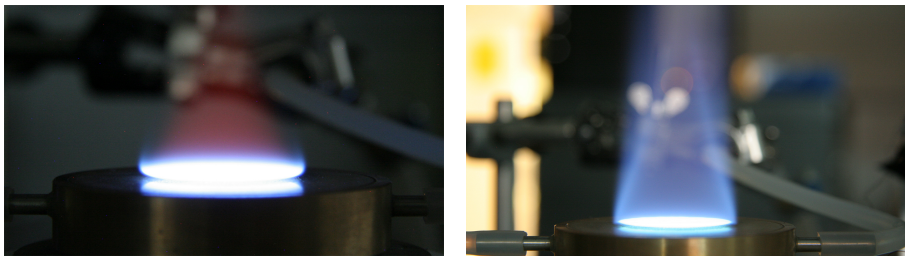

(a) (b)

Figure 3.21: *Photograph of the flame at $\phi = 0.7$ (a) and $\phi = 1.3$ (b) for FLICAS measurements.*

CH_4 + air flames stabilized on the heat flux burner. The generation time t_g was estimated to 5.5 μs. The filling factor of the cavity $\frac{l}{L}$ in Eq. (2.42) was calculated using photographs of the flame to determine l (equal to the primary product zone) and having $L = 100.5$ cm. Figure 3.21 gives an example for the flames with $\phi = 0.7$ and $\phi = 1.3$. FLICAS measurements were done at 7.5 mm above the burner. The spectral range of 6525-6540 cm^{-1} was selected due to the absence of absorption lines from any other molecules in the product zone.

The acquired H_2O absorption spectra were fitted to the simulations made with the HITEMP database. The algorithm is described in Paper VII. Due to strong absorption of H_2O, the baseline in the experiments was unknown, instead, a non-linear least square fit was used to match the experimental data with the theoretical spectra. It was discovered that some of the lines are present in the database, but were not observed during the measurements. These lines were removed from the database. Figure 3.22 from Paper VII presents an example for the flame at $\phi = 1.3$, where the best-fit spectra are

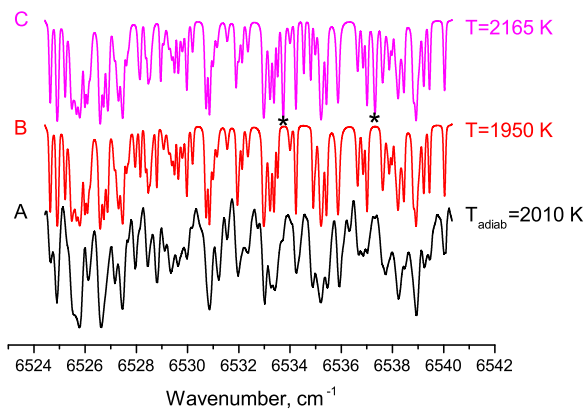

Figure 3.22: *FLICAS spectra of water in CH_4 + air flame at $\phi = 1.3$ (A) along with its simulation using original (C) and modified (B) HITEMP database. Deleted lines are denoted by asterisks.*

shown for the original and modified HITEMP database. Table 3.3 contains temperatures evaluated from the experimental data and obtained by kinetic modeling. The calculations were performed using Aramco mech. 1.3 under equilibrium conditions (T^{ad}) and in a 1D flame with included radiation model (T^{fl}). Radiation losses in CHEMKIN are described assuming the optically thin limit. For the 3-cm heat flux burner this assumption is reasonable, as can be concluded from the results of Lammers and de Goey [164]. More details on the influence of the radiation losses can be found in Paper V. All temperatures obtained using the modified database were found to be lower than adiabatic flame temperatures T^{ad}, opposed to the original HITEMP data. However, they are also systematically lower than T^{fl}. While it is expected that real flame temperatures are affected by heat losses, the detailed modeling shows that at HAB = 7.5 mm their effect is less significant than the experimental values suggest. Therefore, the accuracy of the temperature determination in flames using FLICAS can be estimated to be about ±150 K.

The results of the measurements performed in Tel Aviv in a tubular oven, where temperature can be accurately calibrated, showed that the uncertainty in the obtained values is about ±70 K in the studied temperature range of 1025-1075 K. The accuracy of the flame temperatures was found to be about two times lower than for the oven measurements. The method allows simultaneous determination of concentrations, which differed from the calculated values by about ±20% for the flame experiments. It can be concluded that while FLICAS was shown to be feasible for temperature and concentration measurements using absorption of water vapor, a more thorough spectroscopic assignment procedure is desirable.

Table 3.3: *Temperatures in adiabatic flames.*

ϕ	T^{ad}	T^{fl}	Mod. HITEMP	Orig. HITEMP
0.7	1850	1790	1690	1970
1.1	2200	2160	2010	2245
1.3	2060	2020	1950	2165

Chapter 4

Summary and conclusions

In the present work, fuels relevant to hydrogen combustion were considered in terms of the laminar burning velocity and flame structure. A major part of the thesis is dedicated to the laminar burning velocity of hydrogen flames and its temperature dependence, studied experimentally and using detailed kinetic modeling. The heat flux method for measuring the laminar burning velocity, and specifically, its applicability to hydrogen flames, was also analyzed. Finally, the flame structure of NH_3 and CH_4 flames was considered to determine how well it can be reproduced with contemporary reaction mechanisms and to analyze its use for kinetic model development.

Laminar burning velocity of H_2

Pressure dependence of the burning velocity of very rich hydrogen + air mixtures was studied experimentally, employing spherical flame apparatus, and numerically, using detailed kinetic modeling. It was found that the method for stretch correction does not influence the burning velocity significantly for these conditions. At the same time, for the limiting mixture, $\phi = 7.14$, experimental data disagreed with the simulations. The reasons for the discrepancy were unclear. It is concluded that while further model development can be required, additional measurements with a higher frame rate recording system might be necessary to resolve the flame propagation better, and consequently, the influence of stretch.

Laminar burning velocity of very lean H_2 + air mixtures was measured for the first time in flat stretchless flames at room and elevated temperatures, and the results were compared to the available literature data and detailed kinetic modeling. The present measurements suggest lower values of the burning velocity compared to those obtained in stretched flames, and a different lean flammability limit. Temperature dependence of the laminar burning velocity was presented for the studied conditions in the form of power exponent α. As opposed to a majority of the previous studies, the data from flat flames supports the increasing trend of α with decreasing ϕ, as predicted by kinetic

modeling. It was shown experimentally that α can reach values of about 3-5 at $\phi = 0.4$-0.5. The experimental and numerical results allowed a conclusion that power exponent α cannot be treated as constant for hydrogen flames, even to a first approximation. For a given fuel–oxidizer mixture, it strongly depends on equivalence ratio, diluent content and correlation temperature interval. The results of the present work also validate α as an important independent parameter for analysis of reliability and consistency of burning velocity measurements.

The heat flux method

Heat flux method for measuring burning velocity was analyzed, and a modified procedure of data processing was presented. The method can be applied to unstable flame conditions, in particular to hydrogen flames, improving the accuracy of the measurements. From the analysis of the dependence of the parabolic coefficient on the unburned gas velocity, it has become evident that for a particular burner system the power exponent α is the main flame parameter affecting the accuracy of the measurements. The best accuracy is achieved when α is the lowest.

Different uncertainty factors of a typical heat flux setup were analyzed with the aim to reveal their influence on the accuracy and propose methods for their control. An approach to evaluate asymmetric heat fluxes in the burner plate was proposed. The present study resulted in the necessity to re-evaluate some of the previously published data.

It was concluded that the uncertainty in the unburned gas temperature and combined influence of the edge effects require further investigation. To reduce the uncertainty in the unburned gas temperature, a heating tube should be used at elevated temperatures, and additional thermocouple can also be installed into the plenum chamber, preferably with the possibility to vary its radial position. For the uncertainties related to the flow uniformity at the edges, combined velocity and temperature measurements can be performed in order to quantify the difference between the real and averaged gas velocities.

Combined influence of some uncertainty factors, namely, flow uniformity, edge effects and radiation can be addressed by performing measurements on burners of different diameter, since the burner diameter is a main parameter that allows investigation of their importance.

From the examination of the asymmetric heat fluxes it has become clear that the design with the burner plate integrated with the heating jacket is advantageous over the conventional design, since the temperature scatter can be easily reduced. It has also become evident that burners with scatter of the TC readings higher than about 5 K at adiabatic conditions should not be used, since big temperature scatter is an indication of possible asymmetric heat fluxes.

Structure of NH_3 and CH_4 flames

Structure of NH_3 + air flames was studied. It was found that from the contemporary reaction mechanisms, the model of Mendiara and Glarborg [149] is the best-performing in terms of radical concentration profiles and burning velocities. However, it was concluded that it is difficult to scrutinize unambiguously the remaining uncertainties in the rate constants using the flame structure due to insufficient accuracy of the contemporary experimental methods.

Intracavity absorption methods were implemented to study the flame structure of CH_4 flames. The concentrations of HCO were obtained in a low-pressure flame with ICLAS setup based on an external cavity dye laser, and the experimental results were found to be in good agreement with the modeling. Aramco mech. 1.3 [162] was found to be an appropriate choice for the studied conditions. However, for more detailed analysis of the model, further work is needed. Under the present conditions, a high importance of HCO decomposition channel via collisions with H_2O was identified. Thus, mixtures with a higher amount of H_2O should be studied in the future, e.g., steam-diluted CH_4 + O_2 mixtures. Additional experiments could be aimed at investigating formation of HCO in flames over a wider temperature range.

FLICAS was applied to record H_2O absorption in atmospheric-pressure CH_4 + air flames. It was attempted to use the H_2O absorption spectra for determination of temperature. However, it was concluded that for accurate temperature measurements, the spectroscopic information in the HITEMP database should be modified and a more thorough spectroscopic assignment procedure should be applied.

References

[1] E. Ranzi, A. Frassoldati, R. Grana, A. Cuoci, T. Faravelli, A.P. Kelley, C.K. Law, Hierarchical and comparative kinetic modeling of laminar flame speeds of hydrocarbon and oxygenated fuels, Prog. Energy Combust. Sci. 38 (2012) 468-501.

[2] F.N. Egolfopoulos, N. Hansen, Y. Ju, K. Kohse-Höinghaus, C.K. Law, F. Qi, Advances and challenges in laminar flame experiments and implications for combustion chemistry, Prog. Energy Combust. Sci. 43 (2014) 36-67.

[3] G. Rozenchan, D.L. Zhu, C.K. Law, S.D. Tse, Outward propagation, burning velocities, and chemical effects of methane flames up to 60 ATM, Proc. Combust. Inst. 29 (2002) 1461-1470.

[4] F.N. Egolfopoulos, C.K. Law, Chain Mechanisms in the Overall Reaction Orders in Laminar Flame Propagation, Combust. Flame 80 (1990) 7-16.

[5] L. Figura, A. Gomez, Laminar counterflow steady diffusion flames under high pressure ($P \leq 3$ MPa) conditions, Combust. Flame 159 (2012) 142-150.

[6] M. Goswami, J.G.H. van Griensven, R.J.M. Bastiaans, A.A. Konnov, L.P.H. de Goey, Experimental and modeling study of the effect of elevated pressure on lean high-hydrogen syngas flames, Proc. Combust. Inst. 35 (2015) 655-662.

[7] M. Goswami, R.J.M. Bastiaans, A.A. Konnov, L.P.H. de Goey, Laminar burning velocity of lean H_2-CO mixtures at elevated pressure using the heat flux method, Int. J. Hydrogen Energy 39 (2014) 1485-1498.

[8] M. Goswami, S.C.R. Derks, K. Coumans, W.J. Slikker, M.H. de Andrade Oliveira, R.J.M. Bastiaans, C.C.M. Luijten, L.P.H. de Goey, A.A. Konnov, The effect of elevated pressures on the laminar burning velocity of methane + air mixtures, Combust. Flame 160 (2013) 1627-1635.

[9] A. Keromnes, W.K. Metcalfe, K.A. Heufer, N. Donohoe, A.K. Das, C.J. Sung, J. Herzler, C. Naumann, P. Griebel, O. Mathieu, M.C. Krejci, E.L. Petersen, W.J. Pitz, H.J. Curran, An experimental and detailed chemical

kinetic modeling study of hydrogen and syngas mixture oxidation at elevated pressures, Combust. Flame 160 (2013) 995-1011.

[10] S.C. Taylor, Burning Velocity and the Influence of Flame Stretch, PhD thesis, The University of Leeds, 1991.

[11] V.P. Karpov, A.N. Lipatnikov, P. Wolanski, Finding the Markstein Number Using the Measurements of Expanding Spherical Laminar Flames, Combust. Flame 109 (1997) 436-448.

[12] K.T. Aung, M.I. Hassan, G.M. Faeth, Flame Stretch Interactions of Laminar Premixed Hydrogen/Air Flames at Normal Temperature and Pressure, Combust. Flame 109 (1997) 1-24.

[13] O.C. Kwon, G.M. Faeth, Flame/Stretch Interactions of Premixed Hydrogen-Fueled Flames: Measurements and Predictions, Combust. Flame 124 (2001) 590-610.

[14] N. Lamoureux, N. Djebaili-Chaumeix, C.-E. Paillard, Laminar flame velocity determination for H_2–air–He–CO_2 mixtures using the spherical bomb method, Exp. Therm. Fluid Sci. 27 (2003) 385-393.

[15] S. Verhelst, R. Woolley, M. Lawes, R. Sierens, Laminar and unstable burning velocities and Markstein lengths of hydrogen–air mixtures at engine-like conditions, Proc. Combust. Inst. 30 (2005) 209-216.

[16] D. Bradley, M. Lawes, K. Liu, S. Verhelst, R. Woolley, Laminar burning velocities of lean hydrogen–air mixtures at pressures up to 1.0 MPa, Combust. Flame 149 (2007) 162-172.

[17] M.P. Burke, Z. Chen, Y. Ju, F.L. Dryer, Effect of cylindrical confinement on the determination of laminar flame speeds using outwardly propagating flames, Combust. Flame 156 (2009) 771-779.

[18] E. Hu, Z. Huang, J. He, H. Miao, Experimental and numerical study on laminar burning velocities and flame instabilities of hydrogen–air mixtures at elevated pressures and temperatures, Int. J. Hydrogen Energy 34 (2009) 8741-8755.

[19] M. Kuznetsov, S. Kobelt, J. Grune, T. Jordan, Flammability limits and laminar flame speed of hydrogene-air mixtures at sub-atmospheric pressures, Int. J. Hydrogen Energy 37 (2012) 17580-17588.

[20] M.C. Krejci, O. Mathieu, A.J. Vissotski, S. Ravi, T.G. Sikes, E.L. Petersen, A. Keromnes, W. Metcalfe, H.J. Curran, Laminar Flame Speed and Ignition Delay Time Data for the Kinetic Modeling of Hydrogen and Syngas Fuel Blends, J. Eng. Gas Turbines Power 135 (2013), Paper 021503.

[21] J. Sabard, N. Chaumeix, A. Bentaib, Hydrogen explosion in ITER: Effect of oxygen content on flame propagation of $H_2/O_2/N_2$ mixtures, Fusion Eng. Des. 88 (2013) 2669-2673.

[22] G. Dayma, F. Halter, P. Dagaut, New insights into the peculiar behavior of laminar burning velocities of hydrogen–air flames according to pressure and equivalence ratio, Combust. Flame 161 (2014) 2235-2241.

[23] E. Varea, J. Beeckmann, H. Pitsch, Z. Chen, B. Renou, Determination of burning velocities from spherically expanding H_2/air flames, Proc. Combust. Inst. 35 (2015) 711-719.

[24] F.N. Egolfopoulos, C.K. Law, An experimental and computational study of the burning rates of ultra-lean to moderately-rich $H_2/O_2/N_2$ laminar flames with pressure variations, Proc. Combust. Inst. 23 (1990) 333-340.

[25] C.M. Vagelopoulos, F.N. Egolfopoulos, C.K. Law, Further considerations on the determination of laminar flame speeds with the counterflow twin-flame technique, Proc. Combust. Inst. 25 (1994) 1341-1347.

[26] A.K. Das, K. Kumar, C.J. Sung, Laminar flame speeds of moist syngas mixtures, Combust. Flame 158 (2011) 345-353.

[27] A.K. Das, C.J. Sung, private communication.

[28] O. Park, P.S. Veloo, H. Burbano, F.N. Egolfopoulos, Studies of premixed and non-premixed hydrogen flames, Combust. Flame 162 (2015) 1078-1094.

[29] P. Clavin, Dynamic behavior of premixed flame fronts in laminar and turbulent flows, Prog. Energy Combust. Sci. 11 (1985) 1-59.

[30] A.P. Kelley, C.K. Law, Nonlinear effects in the extraction of laminar flame speeds from expanding spherical flames, Combust. Flame 156 (2009) 1844-1851.

[31] C.K. Wu, C.K. Law, On the determination of laminar flame speeds from stretched flames, Proc. Combust. Inst. 20 (1984) 1941-1949.

[32] J.H. Tien, M. Matalon, On the Burning Velocity of Stretched Flames, Combust. Flame 84 (1991) 238–248.

[33] Y.L. Wang, A.T. Holley, C. Ji, F.N. Egolfopoulos, T.T. Tsotsis, H.J. Curran, Propagation and extinction of premixed dimethyl-ether/air flames, Proc. Combust. Inst. 32 (2009) 1035-1042.

[34] F. Wu, W. Liang, Z. Chen, Y. Ju, C.K. Law, Uncertainty in stretch extrapolation of laminar flame speed from expanding spherical flames, Proc. Combust. Inst. 35 (2015) 663-670.

[35] M. Zhou, C.P. Garner, Direct measurements of burning velocity of propane-air using particle image velocimetry, Combust. Flame, 106 (1996) 363-367.

[36] S. Balusamy, A. Cessou, B. Lecordier, Direct measurement of local instantaneous laminar burning velocity by a new PIV algorithm, Exp. Fluids 50 (2011) 1109-1121.

[37] S. Heimel, Effect of initial mixture-temperature on burning velocity of hydrogen-air mixtures with preheating and simulated preburning, NACA Technical Note 4156, Lewis Flight Propulsion Laboratory, 1957.

[38] T. Iijima, T. Takeno, Effects of Temperature and Pressure on Burning Velocity, Combust. Flame 65 (1986) 35-43.

[39] D.D.S. Liu, R. MacFarlane, Laminar Burning Velocities of Hydrogen-Air and Hydrogen-Air-Steam Flames, Combust. Flame 49 (1983) 59-71.

[40] B.E. Milton, J.C. Keck, Laminar Burning Velocities in Stoichiometric Hydrogen and Hydrogen-Hydrocarbon Gas Mixtures, Combust. Flame 58 (1984) 13-22.

[41] S. Verhelst, R. Sierens, A Laminar Burning Velocity Correlation for Hydrogen/Air Mixtures Valid at Spark-Ignition Engine Conditions, in: Proceedings of ICES03 2003 Spring Technical Conference of the ASME Internal Combustion Engine Division, Salzburg, 2003, Paper ICES2003-555.

[42] G. D'Errico, A. Onorati, S. Ellgas, 1D thermo-fluid dynamic modelling of an S.I. single-cylinder H_2 engine with cryogenic port injection, Int. J. Hydrogen Energy 33 (2008) 5829-5841.

[43] U. Gerke, K. Steurs, P. Rebecchi, K. Boulouchos, Derivation of burning velocities of premixed hydrogen/air flames at engine-relevant conditions using a single-cylinder compression machine with optical access, Int. J. Hydrogen Energy 35 (2010) 2566-2577.

[44] S. Ravi, E.L. Petersen, Laminar flame speed correlations for pure-hydrogen and high-hydrogen content syngas blends with various diluents, Int. J. Hydrogen Energy 37 (2012) 19177-19189.

[45] A.A. Konnov, The effect of temperature on the adiabatic laminar burning velocities of CH_4-air and H_2-air flames, Fuel 89 (2010) 2211-2216.

[46] A.Yu. Kusharin, O.E. Popov, G.L. Agafonov, Нормальные скорости пламени в смесях гремучего газа с водяным паром, Khimicheskaya Fizika 14 (1995) 179-189 (in Russian).

[47] S. Bougrine, S. Richard, A. Nicolle, D. Veynante, Numerical study of laminar flame properties of diluted methane-hydrogen-air flames at high pressure and temperature using detailed chemistry, Int. J. Hydrogen Energy 36 (2011) 12035-12047.

[48] M. Ó Conaire, H.J. Curran, J.M. Simmie, W.J. Pitz, C.K. Westbrook, A Comprehensive Modeling Study of Hydrogen Oxidation, Int. J. Chem. Kinet. 36 (2004) 603-622.

[49] J. Warnatz, Rate Coefficients in the C/H/O System, in: W.C. Gardiner Jr. (Ed.), Combustion Chemistry, Springer-Verlag, New York, 1984, p. 197.

[50] R.A. Yetter, F.L. Dryer, H. Rabitz, A Comprehensive Reaction Mechanism For Carbon Monoxide/Hydrogen/Oxygen Kinetics, Combust. Sci. Technol. 79 (1991) 97-128.

[51] A. Frassoldati, T. Faravelli, E. Ranzi, A wide range modeling study of NO_x formation and nitrogen chemistry in hydrogen combustion, Int. J. Hydrogen Energy 31 (2006) 2310-2328.

[52] G.P. Smith, D.M. Golden, M. Frenklach, N.W. Moriarty, B. Eiteneer, M. Goldenberg, C.T. Bowman, R.K. Hanson, S. Song, W.C. Gardiner Jr., V.V. Lissianski, Z. Qin, GRI-Mech 3.0, 1999; http://www.me.berkeley.edu/gri_mech/.

[53] A.A. Konnov, Remaining uncertainties in the kinetic mechanism of hydrogen combustion, Combust. Flame 152 (2008) 507-528.

[54] C.K. Law, Dynamics of stretched flames, Proc. Combust. Inst. 22 (1988) 1381-1402.

[55] G.H. Markstein, Experimental and Theoretical Studies of Flame-Front Stability, J. Aeronaut. Sci. 18 (1951) 199-209.

[56] A.P. Kelley, J.K. Bechtold, C.K. Law, Premixed flame propagation in a confining vessel with weak pressure rise, J. Fluid Mech. 691 (2012) 26-51.

[57] D.R. Dowdy, D.B. Smith, S.C. Taylor, A. Williams, The use of expanding spherical flames to determine burning velocities and stretch effects in hydrogen/air mixtures, Proc. Combust. Inst. 23 (1990) 325-332.

[58] K.J. Bosschaart, L.P.H. de Goey, Detailed analysis of the heat flux method for measuring burning velocities, Combust. Flame 132 (2003) 170–180.

[59] I.V. Dyakov, A.A. Konnov, J. de Ruyck, K.J. Bosschaart, E.C.M. Brock, L.P.H. de Goey, Measurement of Adiabatic Burning Velocity in Methane-Oxygen-Nitrogen Mixtures, Combust. Sci. Technol. 172 (2001) 81-96.

[60] A.A. Konnov, I.V. Dyakov, J. De Ruyck, Probe Sampling Measurements and Modeling of Nitric Oxide Formation in Methane-Air Flames, Combust. Sci. Technol. 169 (2001) 127-153.

[61] Mass Flow / Pressure meters and controllers for gases and liquids, Instruction manual 9.17.001M, Bronkhorst High-Tech B.V., 2010.

[62] A. van Maaren, D.S. Tsung, L.P.H. de Goey, Measurement of Flame Temperature and Adiabatic Burning Velocity of Methane/Air Mixtures, Combust. Sci. Technol. 96 (1994) 327-344.

[63] B. Lewis, G. von Elbe, Combustion, flames and explosions of gases, third ed., Academic Press, Orlando, 1987.

[64] A.A. Konnov, R.J. Meuwissen, L.P.H. de Goey, The temperature dependence of the laminar burning velocity of ethanol flames, Proc. Combust. Inst. 33 (2011) 1011-1019.

[65] K.J. Bosschaart, Analysis of the Heat Flux Method for Measuring Burning Velocities, PhD thesis, Technische Universiteit Eindhoven, Eindhoven, 2002.

[66] R.T.E. Hermanns, Laminar Burning Velocities of Methane-Hydrogen-Air Mixtures, PhD thesis, Eindhoven University of Technology, Eindhoven, 2007.

[67] R.T.E. Hermanns, A.A. Konnov, R.J.M. Bastiaans, L.P.H. de Goey, Laminar Burning Velocities of Diluted Hydrogen-Oxygen-Nitrogen Mixtures, Energy Fuels 21 (2007) 1977-1981.

[68] A. Van Maaren, L.P.H. de Goey, Laser Doppler Thermometry in Flat Flames, Combust. Sci. Technol. 99 (1994) 105-118.

[69] A.A. Konnov, R. Riemeijer, V.N. Kornilov, L.P.H. de Goey, 2D effects in laminar premixed flames stabilized on a flat flame burner, Exp. Therm. Fluid Sci. 47 (2013) 213-223.

[70] L.P.H. de Goey, L.M.T. Somers, W.M.M.L. Bosch, R.M.M. Mallens, Modeling of the Small Scale Structure of Flat Burner-Stabilized Flames, Combust. Sci. Technol. 104 (1995) 387-400.

[71] J.D. Naucler, L. Sileghem, E.J.K. Nilsson, S. Verhelst, A.A. Konnov, Performance of methanol kinetic mechanisms at oxy-fuel conditions, Combust. Flame 162 (2015) 1719-1728.

[72] S.M. Burke, U. Burke, R. Mc Donagh, O. Mathieu, I. Osorio, C. Keesee, A. Morones, E.L. Petersen, W. Wang, T.A. DeVerter, M.A. Oehlschlaeger, B. Rhodes, R.K. Hanson, D.F. Davidson, B.W. Weber, C.-J. Sung, J. Santner, Y. Ju, F.M. Haas, F.L. Dryer, E.N. Volkov, E.J.K. Nilsson, A.A. Konnov, M. Alrefae, F. Khaled, A. Farooq, P. Dirrenberger, P.-A. Glaude, F. Battin-Leclerc, H.J. Curran, An experimental and modeling study of propene oxidation. Part 2: Ignition delay time and flame speed measurements, Combust. Flame 162 (2015) 296-314.

[73] P. Dirrenberger, P.A. Glaude, H. Le Gall, R. Bounaceur, O. Herbinet, F. Battin-Leclerc, A. A. Konnov, Laminar flame velocity of components of natural gas, in: Proceedings of ASME Turbo Expo 2011, Vancouver, 2011, Paper No. GT2011-46312, pp. 1079-1085.

[74] J.L. Devore, Probability and Statistics for Engineering and the Sciences, eighth ed., Brooks/Cole, Cengage Learning, Boston, 2012.

[75] L. Sileghem, V.A. Alekseev, J. Vancoillie, E.J.K. Nilsson, S. Verhelst, A.A. Konnov, Laminar burning velocities of primary reference fuels and simple alcohols. Fuel 115 (2014) 32-40.

[76] F. Gillespie, W.K. Metcalfe, P. Dirrenberger, O. Herbinet, P.-A. Glaude, F. Battin-Leclerc, H.J. Curran, Measurements of flat-flame velocities of diethyl ether in air, Energy 43 (2012) 140-145.

[77] P.F. Henshaw, T. D'Andrea, K.R.C. Mann, D.S.-K. Ting, Premixed Ammonia-Methane-Air Combustion, Combust. Sci. Technol. 177 (2005) 2151-2170.

[78] S. Goswami, Laminar Burning Velocities at Elevated Pressures using the Heat Flux Method, PhD thesis, Eindhoven University of Technology, 2005.

[79] http://www.omega.com/techref/colorcodes.html, accessed 04.08.2015.

[80] L. Sileghem, V.A. Alekseev, J. Vancoillie, K.M. Van Geem, E.J.K. Nilsson, S. Verhelst, A.A. Konnov, Laminar burning velocity of gasoline and the gasoline surrogate components iso-octane, n-heptane and toluene, Fuel 112 (2013) 355-365.

[81] K.J. Bosschaart, L.P.H. de Goey, The laminar burning velocity of flames propagating in mixtures of hydrocarbons and air measured with the heat flux method, Combust. Flame 136 (2004) 261–269.

[82] T. Knorsch, A. Zackel, D. Mamaikin, L. Zigan, M. Wensing, Comparison of Different Gasoline Alternative Fuels in Terms of Laminar Burning Velocity at Increased Gas Temperatures and Exhaust Gas Recirculation Rates, Energy Fuels 28 (2014) 1446-1452.

[83] K.J. Bosschaart, L.P.H. de Goey, Extension of the Heat Flux Method to Subatmospheric Pressures, Combust. Sci. Technol. 176 (2004) 1537-1564.

[84] Ya.B. Zeldovich, D.A. Frank-Kamenetsky, К теории равномерного распространения пламени, Compt. Rend. Acad. Sci. USSR 19 (1938) 693 (in Russian).

[85] J.P. Botha, D.B. Spalding, The laminar flame speed of propane/air mixtures with heat extraction from the flame, Proc. R. Soc. Lond. Ser. A. Math. Phys. Sci. 225 (1954) 71-96.

[86] Z.H. Wang, W.B. Weng, Y. He, Z.S. Li, K.F. Cen, Effect of H_2/CO ratio and N_2/CO_2 dilution rate on laminar burning velocity of syngas investigated by direct measurement and simulation, Fuel 141 (2015) 285-292.

[87] A.A. Konnov, I.V. Dyakov, Measurement of propagation speeds in adiabatic cellular premixed flames of $CH_4 + O_2 + CO_2$, Exp. Therm. Fluid Sci. 29 (2005) 901-907.

[88] A.A. Konnov, I.V. Dyakov, Measurement of propagation speeds in adiabatic flat and cellular premixed flames of $C_2H_6 + O_2 + CO_2$, Combust. Flame 136 (2004) 371-376.

[89] A.A. Konnov, I.V. Dyakov, Experimental Study of Adiabatic Cellular Premixed Flames of Methane (Ethane, Propane) + Oxygen + Carbon Dioxide Mixtures, Combust. Sci. Technol. 179 (2007) 747-765.

[90] J.F. Yu, R. Yu, X.Q. Fan, M. Christensen, A.A. Konnov, X.S. Bai, Onset of cellular flame instability in adiabatic $CH_4/O_2/CO_2$ and CH_4/air laminar premixed flames stabilized on a flat-flame burner, Combust. Flame 160 (2013) 1276-1286.

[91] F.H.V. Coppens, A.A. Konnov, The effects of enrichment by H2 on propagation speeds in adiabatic flat and cellular premixed flames of CH4 + O2 + CO2, Fuel 87 (2008) 2866-2870.

[92] V. Ratna Kishore, M.R. Ravi, A. Ray, Adiabatic burning velocity and cellular flame characteristics of H2–CO–CO2–air mixtures, Combust. Flame 158 (2011) 2149-2164.

[93] W.B. Weng, Z.H. Wang, Y. He, R. Whiddon, Y.J. Zhou, Z.S. Li, K.F. Cen, Effect of N2/CO2 dilution on laminar burning velocity of H2–CO–O2 oxy-fuel premixed flame, Int. J. Hydrogen Energy 40 (2015) 1203-1211.

[94] V. Ratna Kishore, R. Muchahary, A. Ray, M.R. Ravi, Adiabatic burning velocity of H2–O2 mixtures diluted with CO2/N2/Ar, Int. J. Hydrogen Energy 34 (2009) 8378-8388.

[95] M. Goswami, M. Wustmans, N.J. Dam, R.J.M. Bastiaans, L.P.H de Goey, A.A. Konnov, Temperature Measurement for the Heat Flux Method using ZnO:Zn Thermophosphor, in: Proceedings of the European Combustion Meeting – 2013, Lund, 2013, Paper P3-22, 6 pp; ISBN 978-91-637-2151-9.

[96] J.P.J. van Lipzig, E.J.K. Nilsson, L.P.H. de Goey, A.A. Konnov, Laminar burning velocities of n-heptane, iso-octane, ethanol and their binary and tertiary mixtures, Fuel 90 (2011) 2773-2781.

[97] J. Vancoillie, M. Christensen, E.J.K. Nilsson, S. Verhelst, A.A. Konnov, Temperature Dependence of the Laminar Burning Velocity of Methanol Flames, Energy Fuels 26 (2012) 1557-1564.

[98] E.J.K. Nilsson, L.P.H. de Goey, A.A. Konnov, Laminar burning velocities of acetone in air at room and elevated temperatures, Fuel 105 (2013) 496-502.

[99] M. Christensen, E.J.K. Nilsson, A.A. Konnov, Laminar Burning Velocities of Formaldehyde + Methanol Flames, in: Proceedings of the European Combustion Meeting – 2011, CD Paper, 4 pp, June 28-July 1, 2011, Cardiff, Wales.

[100] J. Vancoillie, M. Christensen, E.J.K. Nilsson, S. Verhelst, A.A. Konnov, The effects of dilution with nitrogen and steam on the laminar burning

velocity of methanol at room and elevated temperatures, Fuel 105 (2013) 732-738.

[101] M.E. Bardin, E.V. Ivanov, E.J.K. Nilsson, V.A. Vinokurov, A.A. Konnov, Laminar Burning Velocities of Dimethyl Carbonate with Air, Energy Fuels 27 (2013) 5513-5517.

[102] N.-E. Olofsson, H. Bladh, A. Bohlin, J. Johnsson, P.-E. Bengtsson, Are Sooting Premixed Porous-Plug Burner Flames One-Dimensional? A Laser-Based Experimental Investigation, Combust. Sci. Technol. 185 (2013) 293-309.

[103] F. Migliorini, S. De Iuliis, F. Cignoli, G. Zizak, How "flat" is the rich premixed flame produced by your McKenna burner?, Combust. Flame 153 (2008) 384–393.

[104] M. Bachmann, W. Wiese, K.-H. Homann, Fullerenes Versus Soot in Benzene Flames, Combust. Flame 101 (1995) 548-550.

[105] G. Berden, R. Peeters, G. Mejner, Cavity ring-down spectroscopy: Experimental schemes and applications, Int. Rev. Phys. Chem. 19 (2000) 565-607.

[106] V.M. Baev, T. Latz, P.E. Toschek, Laser Intracavity Absorption Spectroscopy, Appl. Phys. B 69 (1999) 171-202.

[107] L. Pakhomycheva, E. Sviridenkov, A. Suchkov, L. Titova, S. Churilov, Line structure of generation spectra of lasers with inhomogeneous broadening of the amplification line, JETP Lett. 12 (1970) 43-45.

[108] J. Sierks, T. Latz, V.M. Baev, P.E. Toschek, Spectral Dynamics of Multi-Mode Dye Lasers and Single-Atom Absorption, in: Proceedings of the 1996 European Quantum Electronics Conference (EQEC'96), 8–13 September 1996, Hamburg, Paper QWB6, p. 100.

[109] I. Rahinov, N. Ditzian, A. Goldman, S. Cheskis, Intracavity laser absorption spectroscopy of NH_2 in methane/air flames doped with N_2O, NO, and NH_3, Proc. Combust. Inst. 30 (2005) 1575–1582.

[110] B. Löhden, S. Kuznetsova, K. Sengstock, V.M. Baev, A. Goldman, S. Cheskis, B. Pálsdóttir, Fiber laser intracavity absorption spectroscopy for in situ multicomponent gas analysis in the atmosphere and combustion environments, Appl. Phys. B 102 (2011) 331–344.

[111] J. Hunkemeier, R. Bohm, V. Baev, P. Toschek, Spectral dynamics of multimode Nd^{3+}- and Yb^{3+}-doped fibre lasers with intracavity absorption, Opt. Commun. 176 (2000) 417-428.

[112] CHEMKIN 10112, Reaction Design, San Diego, 2011.

[113] F.A. Lindemann, The Radiation Theory of Chemical Action, Trans. Faraday Soc. 17 (1922) 598-606.

[114] M. Pilling, P. Seakins, Reaction Kinetics, Oxford University Press, New York, 1996.

[115] R.G. Gilbert, K. Luther, J. Troe. Theory of Thermal Unimolecular Reactions in the Fall-off Range. II. Weak Collision Rate Constants, Ber. Bunsenges. Phys. Chem. 87 (1983) 169-177.

[116] R.J. Kee, M.E. Coltrin, P. Glarborg, Chemically reacting flow: theory and practice, John Wiley & Sons, Inc., Hoboken, New Jersey, 2003.

[117] CHEMKIN Theory Manual, CK-THE-10112-1112-UG-1, Reaction Design: San Diego, 2011.

[118] R. J. Kee, J. A. Miller, G. H. Evans, A computational model of the structure and extinction of strained, opposed flow, premixed methane-air flames, Proc. Combust. Inst. 22 (1988) 1479-1494.

[119] Th. V. Karman, Über laminare und turbulente Reibung, Z. Angew. Math. Mech. 1 (1921) 233–252.

[120] M.A. Mueller, T.J. Kim, R.A. Yetter, F.L. Dryer, Flow Reactor Studies and Kinetic Modeling of the H_2/O_2 Reaction, Int. J. Chem. Kinet. 31 (1999) 113-125.

[121] Z. Hong, R.D. Cook, D.F. Davidson, R.K. Hanson, A Shock Tube Study of $OH + H_2O_2 \rightarrow H_2O + HO_2$ and $H_2O_2 + M \rightarrow 2OH + M$ using Laser Absorption of H_2O and OH, J. Phys. Chem. A 114 (2010) 5718-5727.

[122] Z. Hong, D.F. Davidson, E.A. Barbour, R.K. Hanson, A new shock tube study of the $H_2 + O \rightarrow OH + O$ reaction rate using tunable diode laser absorption of H_2O near 2.5 μm, Proc. Combust. Inst. 33 (2011) 309-316.

[123] Z. Hong, S.S. Vasu, D.F. Davidson, R.K. Hanson, Experimental Study of the Rate of $OH + HO_2 \rightarrow H_2O + O_2$ at High Temperatures Using the Reverse Reaction, J. Phys. Chem. A 114 (2010) 5520-5525.

[124] D.A. Masten, R.K. Hanson, C.T. Bowman, Shock Tube Study of the Reaction $H + O_2 \rightarrow OH + O$ Using OH Laser Absorption, J. Phys. Chem. 94 (1990) 7119-7128.

[125] Z. Hong, K.Y. Lam, R. Sur, S. Wang, D.F. Davidson, R.K. Hanson, On the rate constants of $OH + HO_2$ and $HO_2 + HO_2$: A comprehensive study of H_2O_2 thermal decomposition using multi-species laser absorption, Proc. Combust. Inst. 34 (2013) 565-571.

[126] J. Troe, The thermal dissociation/recombination reaction of hydrogen peroxide $H_2O_2(+M) \Longleftrightarrow 2OH(+M)$ III.: Analysis and representation of the temperature and pressure dependence over wide ranges, Combust. Flame 158 (2011) 594-601.

[127] Z. Hong, D.F. Davidson, R.K. Hanson, An improved H_2/O_2 mechanism based on recent shock tube/laser absorption measurements, Combust. Flame 158 (2011) 633-644.

[128] G.A. Pang, D.F. Davidson, R.K. Hanson, Experimental study and modeling of shock tube ignition delay times for hydrogen–oxygen–argon mixtures at low temperatures, Proc. Combust. Inst. 32 (2009) 181-188.

[129] G.W. Koroll, R.K. Kumar, E.M. Bowles, Burning Velocities of Hydrogen-Air Mixtures, Combust. Flame 94 (1993) 330-340.

[130] A.E. Dahoe, Laminar burning velocities of hydrogen–air mixtures from closed vessel gas explosions, J. Loss Prev. Process Ind. 18 (2005) 152-166.

[131] J. Pareja, H.J. Burbano, Y. Ogami, Measurements of the laminar burning velocity of hydrogen–air premixed flames, Int. J. Hydrogen Energy 35 (2010) 1812-1818.

[132] Z. Hong, A. Farooq, E.A. Barbour, D.F. Davidson, R.K. Hanson, Hydrogen Peroxide Decomposition Rate: A Shock Tube Study Using Tunable Laser Absorption of H_2O near 2.5 μm, J. Phys. Chem. A 113 (2009) 12919-12925.

[133] C. Olm, I.Gy. Zsely, R. Pavlolgyi, T. Varga, T. Nagy, H.J. Curran, T. Turanyi, Comparison of the performance of several recent hydrogen combustion mechanisms, Combust. Flame 161 (2014) 2219-2234.

[134] A.P. Kelley, G. Jomaas, C.K. Law, Critical radius for sustained propagation of spark-ignited spherical flames, Combust. Flame 156 (2009) 1006-1013.

[135] Z. Chen, M.P. Burke, Y. Ju, Effects of Lewis number and ignition energy on the determination of laminar flame speed using propagating spherical flames, Proc. Combust. Inst. 32 (2009) 1253-1260.

[136] C.J. Sun, C.J. Sung, L. He, C.K. Law, Dynamics of weakly stretched flames: quantitative description and extraction of global flame parameters, Combust Flame 118 (1999) 108-128.

[137] A.N. Lipatnikov, S.S. Shy, W. Li, Experimental assessment of various methods of determination of laminar flame speed in experiments with expanding spherical flames with positive Markstein lengths, Combust. Flame 162 (2015) 2840-2854.

[138] G. Dixon-Lewis, Structure of laminar flames, Proc. Combust. Inst. 23 (1990) 305-324.

[139] E. Varea, V. Modica, A. Vandel, B. Renou, Measurement of laminar burning velocity and Markstein length relative to fresh gases using a new postprocessing procedure: Application to laminar spherical flames for methane, ethanol and isooctane/air mixtures, Combust. Flame 159 (2012) 577-590.

[140] J.F. Yu, R. Yu, X.S. Bai, Onset of cellular instability in adiabatic $H_2/O_2/N_2$ premixed flames anchored to a flat-flame heat-flux burner, Int. J. Hydrogen Energy 38 (2013) 14866-14878.

[141] A.A. Desoky, Y.A. Abdel-Ghafar, R.M. El-Badrawy, Hydrogen, propane and gasoline laminar flame development in a spherical vessel, Int. J. Hydrogen Energy 15 (1990) 895-905.

[142] S. Verhelst, A Study of the Combustion in Hydrogen-Fuelled Internal Combustion Engines, PhD thesis, Ghent University, 2005.

[143] R. Edse, L.R. Lawrence Jr., Detonation induction phenomena and flame propagation rates in low temperature hydrogen-oxygen mixtures, Combust. Flame 13 (1969) 479-486.

[144] R. Zitoun, B. Deshaies, Burning Velocities of Rich H_2-O_2 Flames under Cryogenic Conditions, Combust. Flame 109 (1997) 427-435.

[145] S.K. Paidi, A. Bhavaraju, M. Akram, S. Kumar, Effect of N_2/CO_2 dilution on laminar burning velocity of H_2-air mixtures at high temperatures, Int. J. Hydrogen Energy 38 (2013) 13812-13821.

[146] A.A. Konnov, J. De Ruyck, A Possible New Route for NO Formation via N_2H_3, Combust. Sci. Technol. 168 (2001) 1-46.

[147] C. Duynslaegher, F. Contino, J. Vandooren, H. Jeanmart, Modeling of ammonia combustion at low pressure, Combust. Flame 159 (2012) 2799-2805.

[148] A.G. Shmakov, O.P. Korobeinichev, I.V. Rybitskaya, A.A. Chernov, D.A. Knyazkov, T.A. Bolshova, A.A. Konnov, Formation and consumption of NO in H_2 + O_2 + N_2 flames doped with NO or NH_3 at atmospheric pressure, Combust. Flame 157 (2010) 556-565.

[149] T. Mendiara, P. Glarborg, Ammonia chemistry in oxy-fuel combustion of methane, Combust. Flame 156 (2009) 1937-1949.

[150] Ø. Skreiberg, P. Kilpinen, P. Glarborg, Ammonia chemistry below 1400 K under fuel-rich conditions in a flow reactor, Combust. Flame 136 (2004) 501-518.

[151] S.J. Klippenstein, L.B. Harding, P. Glarborg, J.A. Miller, The role of NNH in NO formation and control, Combust. Flame 158 (2011) 774-789.

[152] Z. Tian, Y. Li, L. Zhang, P. Glarborg, F. Qi, An experimental and kinetic modeling study of premixed $NH_3/CH_4/O_2$/Ar flames at low pressure, Combust. Flame 156 (2009) 1413-1426.

[153] J.A. Miller, P. Glarborg, Modeling the Thermal De-NOx Process: Closing in on a Final Solution, Int. J. Chem. Kinet. 31 (1999) 757-765.

[154] M.S. Chou, A.M. Dean, D. Stern, Laser absorption measurements of OH, NH, and NH_2 in NH_3/O_2 flames: Determination of an oscillator strength for NH_2, J. Chem. Phys. 76 (1982) 5334-5340.

[155] V.F. Zakaznov, L.A. Kursheva, Z.I. Fedina, Determination of normal flame velocity and critical diameter of flame extinction in ammonia-air mixture, Combust. Explos. Shock Waves 14 (1978) 710-713.

[156] A. Hayakawa, T. Goto, R. Mimoto, Y. Arakawa, T. Kudo, H. Kobayashi, Laminar burning velocity and Markstein length of ammonia/air premixed flames at various pressures, Fuel 159 (2015) 98-106.

[157] K. Takizawa, A. Takahashi, K. Tokuhashi, S. Kondo, A. Sekiya, Burning velocity measurements of nitrogen-containing compounds, J. Hazard. Mater. 155 (2008) 144-152.

[158] J.A. Miller, C.T. Bowman, Mechanism and modeling of nitrogen chemistry in combustion, Prog. Energy Combust. Sci. 15 (1989) 287-338.

[159] J.A. Miller, C.F. Melius, The reactions of imidogen with nitric oxide and molecular oxygen, Proc. Combust. Inst. 24 (1992) 719-726.

[160] J.P. Hessler, Calculation of Reactive Cross Sections and Microcanonical Rates from Kinetic and Thermochemical Data, J. Phys. Chem. A 102 (1998) 4517-4526.

[161] C.L. Rasmussen, J. Hansen, P. Marshall, P. Glarborg, Experimental Measurements and Kinetic Modeling of $CO/H_2/O_2/NO_x$ Conversion at High Pressure, Int. J. Chem. Kinet. 40 (2008) 454-480.

[162] W.K. Metcalfe, S.M. Burke, S.S. Ahmed, H.J. Curran, A Hierarchical and Comparative Kinetic Modeling Study of C-1 - C-2 Hydrocarbon and Oxygenated Fuels, Int. J. Chem. Kinet. 45 (2013) 638-675.

[163] V.A. Lozovsky, S. Cheskis, A. Kachanov, F. Stoeckel, Absolute HCO concentration measurements in methane/air flame using intracavity laser spectroscopy, J. Chem. Phys. 106 (1997) 8384-8391.

[164] F.A. Lammers, L.P.H. de Goey, The influence of gas radiation on the temperature decrease above a burner with a flat porous inert surface, Combust. Flame 136 (2004) 533-547.

Acknowledgments

Finally, I've reached the truly important (and certainly most-read) part of the thesis. Over these five years in Sweden, the best experience I had by far were the people around me: those who I worked with, talked to during the long coffee breaks (which didn't feel that long), or who helped me to understand how the life here works (maybe, I do, finally). I would've never made it without all of you (or it would have never been that fun), and below I'll try to explain why.

First of all, I would like to express my gratitude and deepest respect to my supervisors, *Professor Alexander Konnov* and *Dr. Elna Heimdal Nilsson*. Thank you for all the efforts you put into me, and for patience all those times when I argued with you (and later felt that it was too much). *Alexander*, I really appreciate that your door was always open for discussion, well, even when it wasn't, it usually didn't stop me anyways. You always knew exactly what had to be done and why (and how soon). *Elna*, your favorite advice to us (your students) was "You're a smart person, I'm sure you'll figure it out". Well, most of the times I think we did, so this concept has been proven to be working as well (ok, but not when it comes to editing the papers, where your thoroughness is truly remarkable). But seriously, I was so happy to have you and I learned so much from you, starting from combustion chemistry, mechanisms and reaction rates, to writing, presenting and defending my work against the reviewers who weren't always nice.

I would like to thank *Professor Marcus Aldén* for letting *Alexander* and *Elna* hire me and for giving me a chance to join the Division. I'm still not sure whether it was good for the Division, but it was certainly a life-turning moment for me, so I can't be more grateful to all three of you.

I appeared here almost at the same time with my fellow colleagues, *Jenny Naucler* and *Moah Christensen*, so everything was new for all of us. Thank you for sharing the never-ending struggle with the setups, burners, MFCs, risk analyses and everything else. I think we've been a good team, maybe except for that wine in your office that we are planning to drink together since 2011. *Jenny*, *Moah*, I was always impressed how passionately you considered every problem that appeared over these years, hope it pays off when your turn comes.

The survival strategy of a first-year PhD student is to find some senior

students who look suitable for bombardment with various practical questions and who don't seem to be annoyed by them (or at least don't show it). Thank you, *Ronald Whiddon* and *Andreas Lantz* for being always willing to help, I really appreciate it.

I would like to acknowledge *Dr. Christian Brackmann* and *Dr. Bo Zhou* for our collaboration in the ammonia project. So, we began it at the end of 2012, and now the paper is finally accepted. So maybe it's time to start something new.

I would like to thank the Centre for Combustion Science and Technology (CECOST) for funding my contract, and personally, *Dr. Sven-Inge Möller* for all your work handling our projects, organizing the annual meetings and the Graduate School. No doubt, the CECOST courses were the best part of my coursework, and it's not only because of the outdoor pool/beer sessions. Also, many thanks to *Dr. Zhongshan Li* and *Dr. Mattias Richter* for hosting the two courses which happened to be the best way to learn what all other people in the Division were doing.

I would also like to thank *Minna Ramkull*, *Cecilia Bille* and *Eva Persson* for being always kind and patient explaining how and why I should fill these forms I had no idea about (and probably, needing to do the same for all other people). *Minna*, *Cecilia*, I always had a feeling that your optimism and joy is what really holds this place (and all of us) together.

I shouldn't forget to acknowledge *Susanne Dunér*, *Åke Johansson* and *Igor Buzuk*, who successively took care of our diodes, power boxes, computers, license server and many other things. Equally important, *Igor*, your interest in movies saved so many awkwardly extinguished coffee break conversations, this stuff we could discuss for ages.

I'm also really grateful to *Rutger Lorensson* for providing the best engineering solutions to any nonsense ideas we had. It was almost magical how the parts I needed always appeared in your drawer.

I would like to thank the Tel Aviv group, *Professor Sergey Cheskis*, *Alexey Fomin* and *Dr. Igor Rahinov*, and also *Dr. Valery Baev* from the University of Hamburg for the collaboration and continuous help with ICLAS. This work was only possible thanks to the support from Lund Laser Centre (LLC) and European Cooperation in Science and Technology (COST). Also, I wish to express my deepest gratitude to *Professor Cheskis* for hosting me in Tel Aviv, I really enjoyed the time there, and also for taking me to a road trip and showing places which I would've never visited otherwise.

I would like to mention the collaboration with *Dr. Valerii Zamashchikov* from the Institute of Chemical Kinetics and Combustion in Novosibirsk in the first hydrogen project. My participation in the project was not planned initially, and then suddenly I have the word "hydrogen" in the title of the thesis and in three journal papers.

I am also grateful to the interns: *Joris*, *Luc*, *Astrid* and *Iuliia*. It was a pleasure (and fun) to work with you, well, of course, since I had the authority

to delegate the boring stuff. Hope you enjoyed the time in Sweden despite this.

The Friday group: *Arman*, *Giota*, *Alex*, *Dina*, *Per*, *Ali*, *Jim*, *Igor* and *Fahed* who never joined, and *Sandra* who probably will. Thank you for all the fun and nice discussions (which I always enjoyed, I'm not sure if you did, too...). *Ali* and *Jim*, I'm still not convinced, but maybe some day... Keep trying! My late-afternoon friends, *Bo* (again), *Jiajian* and *Zhenkan*, thank you for filling these long dark evenings with a good laugh and entertaining conversations.

Erdzan, I don't know how you could stand me this last year, desperately trying to prove that the glass is half-full, when it wasn't even a glass. Thank you also for reminding me (almost every day) how important and relevant my work was and how good my chess skills were. But seriously, I learned a lot from you about all that CFD, the importance of turbulence and the history of Balkans (well, mostly the last one).

Steffi, the time you were here was a great fun, I think the amount of social/tourist stuff I participated in thanks to you was larger than during all other years combined. Thank you for being a great friend, always supportive, and I'm really looking forward to see you again!

Alina, thank you for introducing me to the concept of going out for lunch. In fact, it's almost impossible now to find me at the lunch table at the Division (if it's not a coffee break), even after you graduated.

Sasha, your remote cooking classes were of great help. I have a feeling that sometimes you were excited about my life more than I was (and certainly more than I deserved), thank you for your support, I needed it.

Thank you, *Anna* and *Nikolay*, for incepting the idea of going abroad (and practically packing and sending me here). Who would guess, right? And still...

Lena and *Douglas*, there are simply no words I can express my gratitude to you. Whenever I needed help with anything (with everything, basically), you were always there to offer it, and every time I felt welcome. Whenever I needed to switch my mind from the work problems, I could just come to you and there was always something to do, somewhere to go and so many things to laugh about (ok, my Nobel prize was postponed again). I really enjoyed these times.

Finally, I would like to thank my family. Back in days, I never valued the importance of education as much as you wanted me to, but your persistence and your expectations made it possible for me to appear at this stage. Thank you!

Summary of papers

Paper I: V.V. Zamashchikov, V.A. Alekseev, A.A. Konnov, Laminar burning velocities of rich near-limiting flames of hydrogen, Int. J. Hydrogen Energy 39 (2014) 1874–1881; http://dx.doi.org/10.1016/j.ijhydene.2013.11.054.

Laminar burning velocity of rich near-limiting hydrogen flames (70% H_2 + air and 75% H_2 + air) and its pressure dependence was investigated experimentally and numerically. Experiments were conducted in a constant volume bomb equipped with a pressure sensor and a Schlieren system for optical registration of the flame front propagation. Markstein lengths were extracted and compared with the literature by using different extrapolation models. An important role of the critical radius for extraction of the burning velocity and Markstein length was demonstrated. New experimental data were compared with three models for hydrogen combustion to elucidate the need for their further development.

The experiments and image processing were carried out by Dr. V.V. Zamashchikov. I determined S_L from the flame propagation data and performed the modeling. I was responsible for preparing the manuscript, which all co-authors contributed to.

Paper II: V.A. Alekseev, M. Christensen, A.A. Konnov, The effect of temperature on the adiabatic burning velocities of diluted hydrogen flames: A kinetic study using an updated mechanism, Combust. Flame 162 (2015) 1884-1898; http://dx.doi.org/10.1016/j.combustflame.2014.12.009.

The effect of temperature on the adiabatic burning velocities of diluted hydrogen flames was analyzed using an updated version of the Konnov detailed reaction mechanism for hydrogen. The choice of the rate constants was substantiated, and the mechanism was validated against a wide range of cases: jet stirred and flow reactors; oxidation, decomposition and ignition in shock waves; ignition in rapid compression machines; laminar burning velocity and flame structure. An overall improvement of the mechanism performance was observed, particularly for the shock tube and flow reactor data. The updated mechanism was applied to study the temperature dependence of the burning velocity in $H_2 + O_2 + N_2$ flames in a wide range of stoichiometry and dilution

ratios. The simulations were compared to the available experimental results, either taken from the literature or evaluated in the present study from the existing burning velocity data. The temperature dependence was found to be significantly influenced by the equivalence ratio and N_2 content in the mixture. Dependence of the temperature exponent on the fitting temperature range was observed and discussed.

The kinetic mechanism was developed by Prof. A.A. Konnov. I did the validation of the mechanism together with Moah Christensen. I have applied the mechanism for the analysis of the temperature dependence of the burning velocity. I wrote the corresponding sections of the manuscript, and Prof. A.A. Konnov wrote the first part related to the development of the mechanism.

Paper III: V.A. Alekseev, M. Christensen, E. Berrocal, E.J.K. Nilsson, A.A. Konnov, Laminar premixed flat non-stretched lean flames of hydrogen in air, Combust. Flame 162 (2015) 4063-4074;
http://dx.doi.org/10.1016/j.combustflame.2015.07.045.

Laminar burning velocity of lean hydrogen + air flames and its temperature dependence were studied for the first time in stretch-free flat flames on a heat flux burner. The equivalence ratio was varied from 0.375 to 0.5 and the range of the unburned gas temperatures was 278-358 K. The flat flames tended to form cells at adiabatic conditions, therefore special attention was paid to the issue of their appearance. The shape of the flames was monitored by taking OH* images with an EM-CCD camera. In most cases, the burning velocity had to be extrapolated from flat sub-adiabatic conditions, and the accuracy of such procedure was estimated. The measured burning velocities at 298 K showed an important difference to the previously obtained literature values. The temperature dependence of the burning velocity was found to be in agreement with the trends predicted by the detailed kinetic modeling, and contradicted to the majority of the available literature data.

I was responsible for planning the experiments, and performed them together with Moah Christensen, Dr. Edouard Berrocal and Prof. A.A. Konnov. I made data processing and wrote the manuscript, which other co-authors contributed to.

Paper IV: C. Brackmann, V.A. Alekseev, B. Zhou, E. Nordström, P.-E. Bengtsson, Z. Li, M. Aldén, A.A. Konnov, Structure of premixed ammonia + air flames at atmospheric pressure: laser diagnostics and kinetic modeling, Combust. Flame (2015);
http://dx.doi.org/10.1016/j.combustflame.2015.10.012.

Structure of premixed ammonia + air flames, burning at atmospheric pressure under strain-stabilized conditions on a porous-plug burner, has been investigated using laser-diagnostic methods and kinetic modeling. Profiles of OH, NH, and NO were acquired by laser-induced fluorescence (LIF) and quantitative concentrations of OH and NO were retrieved using a concept for calibration versus absorption utilizing the LIF signal itself whereas NH concentrations were evaluated employing a saturated fluorescence signal. In addition, temperatures and relative oxygen concentrations were measured by rotational Coherent Anti-stokes Raman Spectroscopy (CARS). The new experimental data for flames with equivalence ratios of 0.9, 1.0, and 1.2 allowed evaluation of the performance of four contemporary detailed kinetic models. A sensitivity analysis for the best performing mechanism indicated that it is difficult to scrutinize unambiguously the remaining uncertainties of the rate constants implemented in the recent H/N/O models due to insufficient accuracy of the experimental methods.

I participated in the planning of the experiments, which were conducted by Dr. Christian Brackmann and Dr. Bo Zhou. I was responsible for the modeling and the kinetic analysis in the study. Dr. Christian Brackmann and I wrote the manuscript, which other co-authors contributed to.

Paper V: V.A. Alekseev, M. Christensen, J.D. Naucler, E.J.K. Nilsson, E.N. Volkov, L.P.H. de Goey, A.A. Konnov, Experimental uncertainties of the heat flux method for measuring burning velocities, *submitted to Combustion Science and Technology.*

The heat flux method for measuring laminar burning velocity was discussed. An attempt was made to summarize and extend the available information on different factors contributing to the experimental uncertainty of the heat flux method. A typical experimental setup and procedures of the burning velocity determination, used by the Lund University group, were described and the influence of different uncertainty factors, originating from each part of the setup, was analyzed. As a result of this, some of the previously published data had to be re-evaluated. Finally, recommendations were presented in order to control or reduce the uncertainties, and possible directions for future research, aimed at improving the accuracy and understanding of the method, were outlined.

I was the main responsible for the study and wrote the manuscript, which other co-authors contributed to. The information presented in the paper was collected and discussed by all co-authors over several years of work with the heat flux method.

Paper VI: A. Fomin, T. Zavlev, I. Rahinov, V.A. Alekseev, A.A. Konnov, S. Cheskis, Intracavity laser absorption spectroscopy study of HCO radicals during methane to hydrogen conversion in very rich flames, Energy Fuels 29 (2015) 6146-6154; http://dx.doi.org/10.1021/acs.energyfuels.5b01497.

Stoichiometric and very rich low-pressure flames of methane have been investigated using Intracavity Laser Absorption Spectroscopy in terms of absolute HCO concentrations. Temperature profiles were obtained with laser induced fluorescence of OH. The new experimental data were compared with the predictions of two models: GRI-mech 3.0 and Aramco-mech 1.3. GRI-mech was found to perform better in the stoichiometric flame, while Aramco-mech showed better agreement with experiments in the rich flames. Detailed analysis of the behavior of these two models revealed that their similar performance was essentially fortuitous and explained by balancing of different reactions involved in HCO formation and consumption.

I participated in the preliminary ICLAS measurements and construction of the experimenal setup in Tel Aviv. I conducted the modeling of the flame conditions and prepared some of the figures and tables for the manuscript.

Paper VII: A. Fomin, T. Zavlev, I. Rahinov, V.A. Alekseev, A.A. Konnov, V.M. Baev, S. Cheskis, Fiber Laser Intracavity Spectroscopy of hot water for temperature and concentration measurements, Appl. Phys. B: Lasers Opt. (2015); http://dx.doi.org/10.1007/s00340-015-6236-4.

The feasibility of the temperature and concentration measurements using near-IR (≈ 1.5 μm) H_2O spectra obtained by Fiber Laser Intracavity Absorption Spectroscopy (FLICAS) was evaluated. The measurements were performed in Tel Aviv with water vapor heated in a tubular oven at temperatures between 1000 and 1300 K and in Lund having adiabatic flames where temperatures were above 1800 K. The adiabatic flames of methane were stabilized on the heat flux burner. For the temperature and concentration evaluation, the observed spectra were fitted to the simulations using the HITEMP spectroscopic database. Several discrepancies between the HITEMP data and the experiments were found, which lead to significant errors in evaluation. After small corrections in the database, better accuracy was achieved. A more thorough spectroscopic assignment is needed to further improve the results.

I participated in the construction of the FLICAS setup in Lund. I performed FLICAS measurements in flames and contributed to the manuscript, specifically, to the parts describing flame conditions and experiments in Lund.